

American University in Cairo

## AUC Knowledge Fountain

---

Theses and Dissertations

---

6-1-2012

### Determination of shakedown boundary and fitness-assessment-diagrams of cracked pipe bends

Mostafa ElSaadany

Follow this and additional works at: <https://fount.aucegypt.edu/etds>

---

#### Recommended Citation

##### APA Citation

ElSaadany, M. (2012). *Determination of shakedown boundary and fitness-assessment-diagrams of cracked pipe bends* [Master's thesis, the American University in Cairo]. AUC Knowledge Fountain.

<https://fount.aucegypt.edu/etds/1268>

##### MLA Citation

ElSaadany, Mostafa. *Determination of shakedown boundary and fitness-assessment-diagrams of cracked pipe bends*. 2012. American University in Cairo, Master's thesis. *AUC Knowledge Fountain*.

<https://fount.aucegypt.edu/etds/1268>

This Thesis is brought to you for free and open access by AUC Knowledge Fountain. It has been accepted for inclusion in Theses and Dissertations by an authorized administrator of AUC Knowledge Fountain. For more information, please contact [mark.muehlhaeusler@aucegypt.edu](mailto:mark.muehlhaeusler@aucegypt.edu).



**The American University in Cairo**  
**School of Sciences and Engineering**

***Determination of Shakedown Boundary and Fitness-  
Assessment-Diagrams of Cracked Pipe Bends***

By

**Mostafa Siam Elsaadany**

A thesis submitted in partial fulfillment of the requirements for the degree

Of

**Master of Science in Mechanical Engineering**

Under the supervision of:

**Dr. Maher Younan**

Professor of Mechanics and Design  
Associate Dean for Undergraduate Studies  
School of Sciences and Engineering  
The American University in Cairo

**Dr. Hany Fayek**

Assistant Professor of Mechanical Design and Solid Mechanics  
Department of Mechanical Engineering  
The American University in Cairo

**Spring 2012**

The American University in Cairo

**Determination of Shakedown Boundary and Fitness-Assessment-Diagrams of  
Cracked Pipe Bends**

A Thesis Submitted by Mostafa Siam Elsaadany

To Department of Mechanical Engineering

May/2012

In partial fulfillment of the requirements for the degree of Masters of Science in  
Engineering

Has been approved by

Dr. Maher Y. A. Younan

Thesis Committee Chair / Adviser \_\_\_\_\_

Affiliation \_\_\_\_\_

Dr. Hany Fayek Abdalla

Thesis Committee Chair / Adviser \_\_\_\_\_

Affiliation \_\_\_\_\_

Dr. Mohammad Megahed

Thesis Committee Reader / examiner \_\_\_\_\_

Affiliation \_\_\_\_\_

Dr. Abdalla S. Wifi

Thesis Committee Reader / examiner \_\_\_\_\_

Affiliation \_\_\_\_\_

Dr. Mohamed Abdel Moaty

Thesis Committee Reader / examiner \_\_\_\_\_

Affiliation \_\_\_\_\_

\_\_\_\_\_  
Department Chair/  
Program Director

\_\_\_\_\_  
Date

\_\_\_\_\_  
Dean

\_\_\_\_\_  
Date

## ACKNOWLEDGMENT

I know as a matter of fact that I would never be able to give the full due to everybody who helped me during the process of conducting this research. I have to thank the great generous merciful Allah for being always with me during the success times by good fortune and during stumbling times by conferring me patience and perseverance. I cannot find any manner of expression that gives the full due to my supervisor Dr. Maher Younan who was the father that direct, inspire, and encourage. My grand brother before being my supervisor Dr. Hany Fayek was the person who provides smart solutions and moral support when the road was full of obstacles. The American University in Cairo is highly acknowledged for the financial support of this research and also for giving me the chance to utilize the state of the art computational facilities. Special thanks to Eng. Mohammed Abdelaal for his generous help and support. Special thanks to my colleagues Youssef Fouad and Ahmed Gaber. Last and foremost, my adored family: to my mother, words fail to express my gratitude to you. To my father, your words that you told me when I was just crawling in my road towards this day were always echoing in my ears; you have been always my inspiration. My brother Eng. Mahmoud and my little sister Magi, thanks for bearing me ever and always. To my beloved wife Dr. Alshaimaa, my dream has come to reality only when you were beside me and recently you gave me the best gift in this world, ABDELRAHAMAN who I wholeheartedly dedicate this thesis.

## ABSTRACT

Determination of shakedown boundaries of 90-degree defect-free smooth pipe bends has received substantial attention by several researchers within the recent decades. However, scarce information is found within the literature regarding the determination of the shakedown boundary of cracked pipe bends. The current research outcomes include the determination of shakedown boundary for a circumferentially cracked 90-degree pipe bend via a simplified technique utilizing the finite element method, and introduction of Failure-Assessment-Diagrams (FAD) in compliance with the API 579 Failure-for-Service assessment of pressure vessel and piping components. The analyzed cracked pipe bend is subjected to the combined effect of steady internal pressure spectrum and cyclic In-Plane Closing (IPC) or opening (IPO) bending moments. Line Spring Elements (LSE) are embedded in quadratic shell elements to model part through cracks. Failure assessment diagrams (FAD) are developed through linking the J-integral fracture mechanics parameter with the shakedown limit moments of the analyzed cracked 90-degree pipe bend. The LSE outcomes illustrated satisfactory results in comparison to the results of verification studies: stress intensity factor, Shakedown (SD) limit, and limit load. Additionally, full elastic-plastic cyclic loading finite element analyses are conducted and the outcomes revealed good correlation with the results obtained via the simplified technique. The maximum load carrying capacity (limit moment) and the elastic domain are also computed thereby generating a Bree diagram for the cracked pipe bend.

## TABLE OF CONTENTS

INTRODUCTION .....	1
1.1 Introduction .....	1
1.2 Literature review .....	3
1.2.1 Limit load.....	3
1.2.2 Shakedown load.....	5
1.2.2.1 The Simplified Technique .....	9
1.2.3 Load carrying capacity of cracked structures .....	10
1.2.3.1 Fitness-for-Service procedure adopted in API 579 .....	10
1.2.3.2 Shakedown analysis of cracked structures .....	11
1.2.3.3 Limit load analysis of cracked pipe bends.....	12
1.2.4 Line spring model .....	16
1.3 Objectives.....	18
1.4 Thesis outlines.....	18
MODELING AND ANALYSIS.....	20
2.1 Models description .....	21
2.2 Stress intensity factor verification study .....	28
2.3 Shakedown limit verification study.....	33
2.4 Limit load verification study .....	36
2.5 Application of the simplified technique .....	43

2.6	Proposed procedure for FAD generation .....	45
2.6.1	Failure Assessment Diagram generation .....	45
2.6.2	Assessment procedure.....	49
RESULTS and DISCUSSION .....		55
3.1	Bree diagrams.....	55
3.1.1	Pipe bends under IPO bending moment and internal pressure .....	55
3.1.1.1	Defect-Free model .....	55
3.1.1.2	Pipe bend with 45° circumferential crack.....	56
3.1.1.3	Pipe bend with 120° circumferential crack.....	57
3.1.1.4	Effect of crack size on SD boundary .....	59
3.1.1.5	Effect of crack depth on SD boundary .....	60
3.1.2	Pipe bends under IPC bending moment and internal pressure .....	60
3.1.2.1	Defect-Free model .....	60
3.1.2.2	Pipe bend with 120° circumferential crack.....	61
3.1.2.3	Effect of crack size on SD boundary .....	63
3.1.3	Comparison between IPO and IPC bending moments.....	64
3.2	Validation of the simplified technique using full cyclic loading .....	66
3.3	Failure Assessment Diagrams .....	69
3.3.1	Elastic and total J-integrals .....	69
3.3.2	The effect of crack size and loading condition on J-integrals .....	69
3.3.3	The proposed FAD.....	75

3.3.4	Application of The proposed procedure .....	79
3.3.5	Crack growth analysis.....	82
CONCLUSIONS and RECOMMENDATIONS .....		85
4.1	Conclusions .....	85
4.2	Recommendations and future work.....	86
REFERENCES .....		87
Appendix (A).....		95
Appendix (B).....		97
Appendix (C).....		98

## LIST OF TABLES

Table 1 Pipe bend (90-degree Sch. 40) geometry .....	22
Table 2 Pipe bend material properties .....	25
Table 3 Stress Intensity Factors verification study summary .....	31
Table 4 Shakedown limit verification study .....	36
Table 5 Defect-Free models assuming large deformation limit load verification study summary.....	40
Table 6 Limit load verification study summary.....	41
Table 7 Summary of the models investigated.....	54

## LIST OF FIGURES

Fig. 1 Twice-Elastic-Slope Method adopted in ASME Sec. VIII Div. II to determine the plastic collapse load [4].....	4
Fig. 2 Tangent-Intersection Method used to obtain the plastic collapse load [4] .....	4
Fig. 3 Bree diagram of defect free components illustrating the safe and the unsafe operating domains .....	6
Fig. 4 Failure regions on the Failure Assessment Diagram [18] .....	11
Fig. 5 Schematic illustration of LSE (LS6 and LS3S) connected to eight node shell elements (S8R) [53] .....	17
Fig. 6 Schematic drawing showing a typical 90-degree pipe bend and major line sectioning the pipe bend meridional direction [4] .....	22
Fig. 7 Experimental setup [17].....	23
Fig. 8 Notation for circumferentially cracked pipe bends .....	23
Fig. 9 Notation for meridionally cracked pipe bends [17].....	24
Fig. 10 True Stress-Strain curve of the material tested by Yahiaoui et. al. [17].....	25
Fig. 11 Pipe bend quarter model geometry .....	26
Fig. 12 Quarter model of the pipe bend that is used to introduce external circumferential crack on the intrados.....	27

Fig. 13 Quarter model of the pipe bend that is used to introduce external circumferential crack on the extrados .....	27
Fig. 14 Quarter model of the plate with central surface crack .....	29
Fig. 15 Full model of the plate with central surface crack.....	30
Fig. 16 Deformed shape and stress contours of the full model utilizing the element LS6 at SP1 (crack ligament) .....	32
Fig. 17 Deformed shape and stress contours of the quarter model utilizing the element LS3S at SP5 (crack tip) .....	32
Fig. 18 Geometry and Boundary conditions annotations of the thick cylinder with longitudinal part through crack under internal pressure .....	34
Fig. 19 Deformed shape of the thick cylinder with longitudinal part through crack under internal pressure .....	35
Fig. 20 Quarter model of pipe bend that is used to introduce internal circumferential crack on the intrados. ....	38
Fig. 21 Full model of the pipe bend that is used to introduce internal meridional crack on the crown.....	38
Fig. 22 Moment-Displacement curve of the defect-free model assuming large deformation used to determine the limit load using TES method. ....	39
Fig. 23 Moment-Displacement curve of QM120C model assuming small deformation used to determine the limit load.....	40

Fig. 24 Deformed shape of the quarter model with internal circumferential crack .....	42
Fig. 25 Deformed shape of the full model with internal meridional crack on the crown.....	42
Fig. 26 Schematic representation of the simplified technique analyses [4].....	43
Fig. 27 Failure Assessment Diagram generation procedure .....	48
Fig. 28 Assessment procedure .....	51
Fig. 29 Elastic J-integral Vs. Applied Moment for the case of QM120C-IPO at 15% $P_y$ .....	51
Fig. 30 Total J-integral Vs. Applied Moment for the case of QM120C-IPO at 15% $P_y$ .....	52
Fig. 31 Assessment criteria .....	53
Fig. 32 Integrity assessment procedure of cracked pipe bends.....	54
Fig. 33 Representative sample Moment End-Rotation curve for the Defect-Free model at 30% $P_y$ used for limit load Determination using TES method. ....	55
Fig. 34 Normalized limit, shakedown and elastic moments of the defect-free pipe bend subjected to IPO bending moment and internal pressure .....	56
Fig. 35 Normalized limit, shakedown and elastic moments of the pipe bend with 45° circumferential crack ( $b/t=0.5$ ) subjected to IPO bending moment and internal pressure .....	57

Fig. 36 Normalized limit, shakedown and elastic moments of pipe bend with $120^\circ$ circumferential crack ( $b/t=0.5$ ) subjected to IPO bending moment and internal pressure .....	58
Fig. 37 Normalized limit, shakedown and elastic moments of pipe bend with $120^\circ$ circumferential crack ( $b/t=0.75$ ) subjected to IPO bending moment and internal pressure .....	58
Fig. 38 Comparison between SD limits of Defect-Free-IPO, QM45C-IPO, and QM120C-IPO Models ( $b/t=0.5$ ) .....	59
Fig. 39 Comparison between SD limits of Defect-Free-IPO, QM120C-IPO ( $b/t=0.5$ ), and QM120C-IPO ( $b/t=0.75$ ) Models.....	60
Fig. 40 Normalized limit, shakedown and elastic moments of the defect-free pipe bend subjected to IPC bending moment and internal pressure .....	61
Fig. 41 Normalized limit, SD, and elastic moments of QM120C ( $b/t =0.5$ ) subjected to IPC bending moment and internal Pressure.....	62
Fig. 42 Normalized limit, SD, and elastic moments of QM120C ( $b/t =0.75$ ) subjected to IPC bending moment and internal pressure .....	63
Fig. 43 Comparison between Elastic and SD limits of Defect-Free and QM120C ( $b/t =0.75$ ) models subjected to IPC bending moment and internal pressure.....	64
Fig. 44 Comparison between Elastic and SD limits of Defect-Free models under IPO and IPC bending moments ( $b/t=0.75$ ).....	65

Fig. 45 Comparison between Elastic and SD limits of QM120C-IPO, and QM120C-IPC (b/t=0.5) .....	65
Fig. 46 Comparison between Elastic and SD limits of QM120C-IPO, and QM120C-IPC (b/t=0.75) .....	66
Fig. 47 Elastic shakedown behavior of the model QM120C-IPO exhibited for the case of 15% $P_y$ using the shake down limit obtained by the simplified technique. ....	67
Fig. 48 Reversed plasticity behavior exhibited for the case of 0% $P_y$ (QM120C-IPO) upon slightly exceeding the shakedown limit obtained using the simplified technique. ....	68
Fig. 49 Ratchetting behavior exhibited for the case of 40% $P_y$ Defect-free model upon slightly exceeding the shakedown limit obtained using the simplified technique. ....	68
Fig. 50 The effect of increasing the internal pressure on the elastic J-integral for the model QM120C-IPO (b/t =0.75) .....	70
Fig. 51 The effect of increasing the internal pressure on the total J-integral for the model QM120C-IPO (b/t=0.75) .....	70
Fig. 52 Comparison between the elastic J-integral obtained under IPO bending only of the models QM120C and QM45C (b/t=0.5).....	71
Fig. 53 Comparison between the total J-integral obtained under IPO bending only of the models QM120C and QM45C (b/t=0.5).....	72

Fig. 54 Comparison between the elastic J-integral obtained under IPO bending and 10% $P_y$ of the models QM120C and QM45C ( $b/t=0.5$ ).....	72
Fig. 55 Comparison between the total J-integral obtained under IPO bending and 10% $P_y$ of the models QM120C and QM45C ( $b/t=0.5$ ).....	73
Fig. 56 Comparison between the elastic J-integral obtained under IPO and IPC bending of the model QM120C ( $b/t=0.75$ ) .....	74
Fig. 57 Comparison between the total J-integral obtained under IPO and IPC bending of the model QM120C ( $b/t=0.75$ ).....	74
Fig. 58 Failure Assessment Diagram of QM120C model ( $P=0\%P_y$ ) and ( $b/t = 0.75$ )	75
Fig. 59 Failure Assessment Diagram of QM120C-IPO model ( $P=15\%P_y$ ) and ( $b/t = 0.75$ ) .....	76
Fig. 60 The effect of increasing the internal pressure on the FAD of the model QM120C-IPO ( $b/t=0.75$ ) .....	77
Fig. 61 Failure Assessment Diagram of QM45C-IPO model ( $P=20\%P_y$ ) and ( $b/t = 0.5$ ) .....	77
Fig. 62 The effect of increasing the internal pressure on the FAD of the model QM145C-IPO ( $b/t=0.5$ ) .....	78
Fig. 63 Failure Assessment Diagram of QM120C-IPC model ( $P=40\%P_y$ ) and ( $b/t = 0.75$ ) .....	78

Fig. 64 Elastic J-integral Vs. Applied Moment for the case of QM120C-IPO at 0% $P_y$	80
Fig. 65 Total J-integral Vs. Applied Moment for the case of QM120C-IPO at 0% $P_y$	81
Fig. 66 Assessment points Vs. FAL for the model QM120C-IPO ( $b/t=0.75$ ) at 0% $P_y$	81
Fig. 67 Assessment points Vs. FAL for the model QM120C-IPO ( $b/t=0.75$ ) at 15% $P_y$	82
Fig. 68 Crack growth analysis for the pipe bend models with circumferential crack at the intrados under the combined effect of IPO bending moment and internal pressure	84

## ACRONYMS

ASME	American Society of Mechanical Engineers
API	American Petroleum Institute
DBA	Design by Analysis
ECM	Elastic Compensation Method
EPP	Elastic-Perfectly-Plastic
FAD	Failure Assessment Diagram
IPC	In-Plane Closing
IPO	In-Plane Opening
KH	Kinematic Hardening
Large Disp.	Large Displacement
NPS	Nominal Pipe Size
OP	Out-of-Plane
PEEQ	Equivalent Plastic Strain
Sch.	Schedule
SD	Shakedown
Simp. Tech.	Simplified Technique
Small Disp.	Small Displacement
SP	Section Point

## NOMENCLATURE

$C$	Paris law constant
$E$	Modulus of elasticity
$J$	J-integral
$J-ELA$	Elastic J-integral
$L$	Length of straight pipe
$P$	Internal pressure
$PEEQ$	Equivalent plastic strain
$Q$	Complete elliptic integral
$R$	Pipe bend radius
$D_m$	Pipe mean diameter
$G_j$	Influence coefficients
$J_{Ic}$	Material fracture toughness
$K_{Ic}$	Material fracture toughness
$K_r$	Toughness ratio
$L_r$	Load ratio
$M_{ref}$	Reference moment
$M_i$	Applied moment increment
$P_Y$	Internal pressure that causes yielding
$R_i$	Thick cylinder inner radius

$b$	Crack depth
$i$	Elastic-plastic solution increment
$n$	Paris law constant
$t$	Pipe wall thickness
$\theta$	Crack angle
$\sigma_E$	Elastic stress components
$\sigma_{ELPL}$	Elastic-plastic stress components
$\sigma_y$	Material yield strength
$\sigma_r$	Residual stress
$\sigma_u$	Material ultimate strength
$\nu$	Poisson's ratio

# CHAPTER 1

## INTRODUCTION

### 1.1 Introduction

The problem of shakedown (SD) limit load determination for various structures particularly pressure vessels and piping components subjected to the simultaneous effect of steady and cyclic loads has become of major importance. Limit loads and SD limits are determined to define the safe loading domain for defect-free structures. It is very important also for fitness for service requirements to assess the capability of the structure to perform its function under certain loads and to answer the question of whether the structure is still capable of performing its functional requirements when some defects are existent. Defects like local wall thinning due to erosion, corrosion, and crack initiation and propagation might occur during service. These defects alter, significantly, the load carrying capacity of the components that is why it is essential to investigate their influence on the behaviour of piping components.

Pipe bends are commonly utilized in various industrial fields such as the petrochemicals, pharmaceuticals, and conventional and nuclear power plants. Pipeline networks are often exposed to elevated temperatures or hazardous environments that dictate the application of strict safety assessment procedures requiring deep understanding of the detailed stress fields involved in the structure. Pipe bends are used to change the direction of fluid flow, but this is not always the case. Mourad and Younan [1] showed that pipe bends are used to introduce flexibility to the piping

system as they were found to possess (5-20) times the flexibility of a straight pipe having the same size and material properties. Hence, pipe bends should be capable of sustaining thermal, seismic, and pressure effects and at the same time minimizing the induced loading on the whole system and the piping component itself. On the other hand, the stress fields induced on the pipe bend are (3-12) times that of a straight pipe having the same size and material properties.

Bantlin [2] proved through experimental analysis that pipe bends respond differently than straight pipes which tend to behave like beams. Karaman [3] proved the claim of Bantlin [2] by performing analytical investigations. Karaman [3] concluded that pipe bends possess high bending flexibility than straight pipes because of the virtue of its curved shape that renders it behave like a shell more than a beam; however, it was shown that pipe bends have more stress and strain magnitudes than straight pipes. Previous work in the literature [1, 19, 27-33] has proved that pipe bends possess low limit load and SD limit load compared to straight pipes having the same size and material properties. For that reason, pipe bends are considered critical components that should be investigated to develop the safe domain with respect to plastic collapse and SD limits.

## 1.2 Literature review

### 1.2.1 Limit load

There are many definitions for limit load. The theoretical definition of limit load is based upon the assumption of Elastic-Perfectly-Plastic (EPP) material model and ignoring the geometric nonlinearity. However, in practice the term limit load is usually used under the assumption of large deformation and strain hardening (Robertson et. al. [16]). The plastic instability load is defined as the load at which the load-deflection curve has a zero slope. Robertson et. al. [16] stated that the plastic instability load is based on large deformation analyses and that it is dependent on the load path leading to collapse. The plastic instability moment is an important parameter because it might be smaller than the limit moment depending upon the loading case that might cause geometrical weakening rather than stiffening effect.

The plastic collapse load is the load at which significant plastic deformation occurs in the system under consideration. The limit load determined in this study is obtained using the ASME Sec. VIII Div. II Twice-Elastic-Slope (TES) method as shown in Fig. 1. The TES method is based on doubling the slope of the linear part of load-deflection curve and defines the load at the intercept with the nonlinear part as the plastic collapse load. On the other hand, there are several definitions used to obtain the limit load. The Tangent-Intersection Method is shown in Fig. 2. It depends on drawing two tangents for the linear (elastic) and nonlinear parts of the load-deflection curve and the intersection of the two tangents corresponds to limit load. One of the drawbacks of the Tangent-Intersection Method is the difficulty to decide upon a certain point on the nonlinear part of the load deflection curve to draw a tangent.

Yahiaoui et. al. [17] used the plateau of the moment-displacement curve to define the limit load; this definition is used in the limit load verification study in Sec. 2.4. There are other methods to obtain the limit load like the Twice-elastic Deformation method, the 1% Plastic Strain Method, and Proportional-Limit Method, but they are not as commonly used as the TES method adopted in ASME Boiler and Pressure Vessel Code [11].

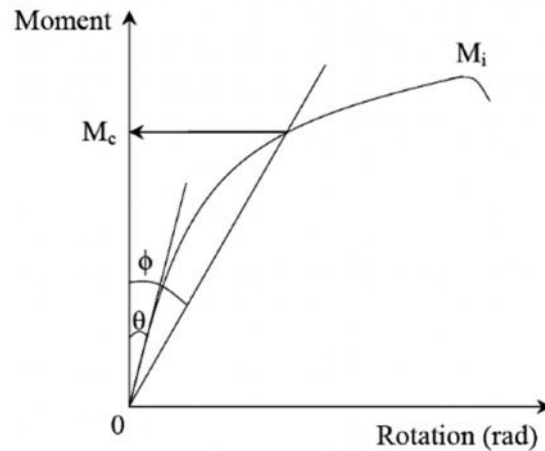


**Fig. 1 Twice-Elastic-Slope Method adopted in ASME Sec. VIII Div. II to determine the plastic collapse load [4]**

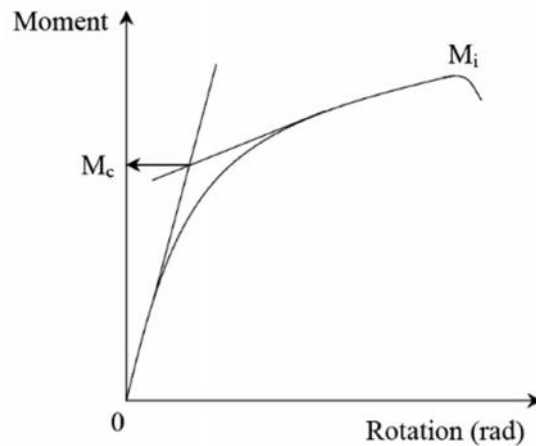


**Fig. 2 Tangent-Intersection Method used to obtain the plastic collapse load [4]**

### 1.2.2 Shakedown load

Some measures of controlled plastic deformation are sometimes allowed in most well-designed systems without affecting the safety of the component. Being within the plastic domain, it is essential to determine the limit load for structures subjected to monotonic loading, on the other hand, it is essential to determine the shakedown limit load (SD) for structures subjected to cyclic loading. Exceeding the limit load would result in failure due to gross plastic deformation or plastic instability while exceeding the elastic SD limit might result in two ductile failure mechanisms which are reversed plasticity or ratcheting. Elastic SD means that the material will behave fully elastically after a limited amount of plasticity in the first loading cycles.

Reversed plasticity (plastic SD) means that the structure will have plastic strain by the end of loading which is completely reversed by the end of unloading; however, the structure will fail after a certain number of cycles because of low cycle fatigue. The other failure mode is called ratcheting, and it means that the structure will accumulate plastic strain during each loading-unloading cycle until ductility is exhausted and collapse occurs. The generalized interaction diagram which is commonly termed Bree diagram is shown in Fig. 3. It should be noted that the SD interaction diagram was first proposed by Bree in 1967. The safe region that corresponds to Elastic limit, Elastic SD limit, and limit loads are defined within the diagram as well as the different failure mechanisms encountered upon exceeding the aforementioned limits.

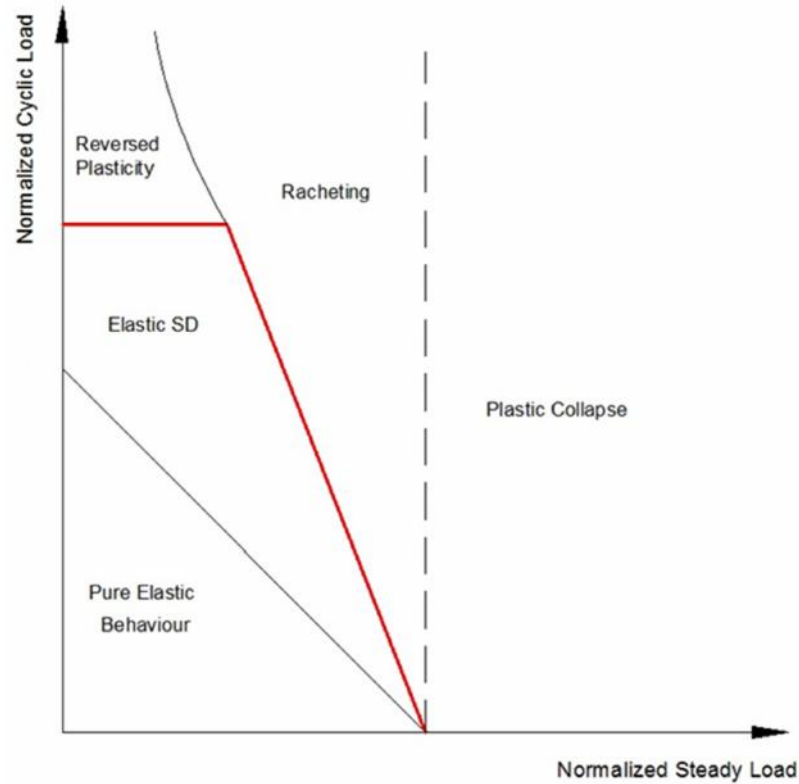


**Fig. 3 Bree diagram of defect free components illustrating the safe and the unsafe operating domains**

Determination of the SD limit load is not an easy task due to emerging structural complexities specifically geometrical and loading effects, closed form solutions become more and more difficult. Accordingly, numerical analyses render solutions of complex problems both adequate and computationally economic. Obtaining a closed form solution for the SD limit load is only amenable for mathematically manageable benchmark problems like the two bar structure and the Bree cylinder. The elastic SD lower bound theorem was initially introduced by Gruning [5] in 1929, extended by Bleich [6] and then developed and formulated by Melan [7-9] where he stated that: “For a given load set  $P$ , if any distribution of self-equilibrating residual stresses can be found (assuming perfect plasticity) which when taken together with elastically calculated stresses, constitute a system of stresses

*within the yield limit, then  $P$  is a lower bound shakedown load set and the structure will shakedown”.*

In 1960, Koiter [10] introduced the upper bound SD theorem which is based on an energy approach by comparing the rate at which the applied loads perform work by the rate of internal energy dissipation. The lower bound SD theorem is widely adopted by several design codes such as ASME Boiler and Pressure Vessel Code [11], UK Pressure Vessel Design code [12], the German Pressure Vessel Design Code [13], and the European Pressure Vessel Standard [14]. Lower bound shakedown theorem is employed throughout the present thesis. After the introduction of Melan’s theorem, research efforts has witnessed attention to determine the shakedown limit loads with major focus on pressure vessels and piping components.

Research has been conducted after introducing Melan's theorem to develop different techniques to obtain a SD limit load without the need to perform challenging mathematical derivations to get a closed form solution. Iterative elastic techniques were developed and used extensively by the aid of Finite FE method to find a quick and approximate SD limit load. One of the most commonly used techniques to obtain SD limit load is the Elastic Compensation Method (ECM) which was first introduced by Marriot [20], Developed by Dhalla [21], Seshadri [22], Ponter [23] and then extensively utilized by Mackenzie and Boyle [24]. Elastic Compensation Method (ECM) was widely used because of its simplicity in obtaining the elastic and residual stress fields that are required to be substituted in Melan’s lower bound theorem to get a lower bound SD limit load. In this method, the elastic moduli of the elements are modified based on the previous iterations’ calculated stress fields. Accuracy of ECM technique depends on the FE mesh and is strongly influenced by the positions of

singularities like sharp edges. ECM can be automated by using the FE software capabilities of parametric design [24-25]

ASME Section VIII Div. II Design by Analysis (DBA) [11] introduced the stress categorization in the 1960s; the code defined different stress limits which change with service conditions. Stress limits include primary, secondary, and peak stresses; these stress limits are used to define the service limits. The ASME code defined the stress limits as follows:

- Primary stress is a load controlled stress that might be normal or shear stress developed by the applied load. The main characteristic of primary stress is that it is not self-limiting and, if primary stress exceeds the yield stress, failure or distortion is going to occur. The primary stresses might include general membrane stress in a circular cylindrical or a spherical shell due to internal pressure or the bending stress in the central portion of a flat head due to pressure.
- Secondary stress is self-limiting developed by the self-constraints of the structure or constraints of neighbourhood different material. This stress may be due to local yielding or minor distortions, but cannot cause failure if it is only applied. Secondary stresses might include general thermal stress or the bending stress at a gross structural discontinuity.
- Peak stress is the portion added to the primary and secondary stresses because of the presence of stress concentrations that exist as a result of local discontinuities. This kind of stress does not cause remarkable distortion, but is considered as the reason for fatigue cracks and brittle fracture.

According to the ASME DBA [11] and Muscat et al. [26], primary stresses only and secondary stresses added to primary stresses would cause plastic deformation; however, peak stress is highly localized and can only be considered for high cycle fatigue. Primary plus secondary stresses had to be considered to investigate the SD limit; the DBA design limit for this problem is  $3S_m$ . Where  $S_m$  is the allowable material stress intensity and is evaluated according to the following rule for ferritic steels:

$$S_m = \min \left( \frac{1}{3} \sigma_u, \frac{2}{3} \sigma_y \right) \quad (1)$$

The code specified  $1.5S_m$  as the design limit;  $2.25S_m$  for emergency (Level C); and  $3S_m$  for faulted conditions (Level D), that is why  $3S_m$  is used as the limiting design load for the problem of SD. The stress fields of spherical vessels with axisymmetric nozzles under internal pressure obtained by the code are compared to these obtained by Muscat et al. [26] who were conservative in their analysis by adding peak stress to the primary and secondary stress. Muscat et al. [26] showed that the DBA  $3S_m$  did not guarantee that plastic SD will not occur in all cases. Hence, a review of the DBA code has to be conducted to assure elastic SD under developed stresses less than  $3S_m$ . It is worth mentioning that Muscat et al. [26] used a superposition method that is similar to the approach proposed by Abdalla et al. [19].

#### 1.2.2.1 The Simplified Technique

Abdalla et al. [19] introduced a very useful technique to determine a lower bound SD limit load without conducting the conventional iterative elastic solutions or the long time consuming full elastic-plastic cyclic loading; the simplified technique was verified by applying it to benchmark SD problems like the two bar model and

Bree cylinder. The simplified technique consists mainly of two consecutive analyses: the first is elastic analysis (simulating unloading) and this analysis is conducted by applying the cyclic load only without exceeding the yield stress while the second analysis is Elastic-Plastic that comprises of two steps: the first is applying the static load monotonically without exceeding the yield and the second sub analysis is applying the cyclic load monotonically by exceeding the yield stress and maintaining the static load applied. The superposition rule (Eq. 2) is then applied to calculate the residual stress components:

$$\sigma_{r_i} = \sigma_{ELPL_i} - \sigma_E \frac{M_i}{M_{ref}} \quad (2)$$

Where:

$\sigma_{r_i}$  : Von-Mises Equivalent residual stress

i: Load increment

$\sigma_{ELPL}$  : Elastic-plastic stress components

$\sigma_E$  : Elastic stress components

$M_i$ : Applied moment increment

$M_{ref}$ : Reference moment

### 1.2.3 Load carrying capacity of cracked structures

#### 1.2.3.1 Fitness-for-Service procedure adopted in API 579

Part-9 of the API 579-1/ ASME FFS-1 [18] procedure for the assessment of structures with crack-like flaw is summerized herein. The procedure is based on the generation of a Failure Assessment Diagram (FAD) and then assessment point is

plotted on the diagram using two parameters namely: Load Ratio ( $L_r$ ) plotted on the abscissa and Toughness Ratio ( $K_r$ ) plotted on the ordinate. Load ratio represents the tendency of the structure to fail by plastic collapse while toughness ratio represents the tendency of the structure to fail by unstable crack growth. The details about the procedure of FAD generation and the methodology of assessment can be referred to the API 579-1/ ASME FFS-1 [18]. However, a brief description about the assesment procedure is presented in Chapter 2. A sample FAD adopted in the Fitness-for-Service assessment of crack like flaws in the API 579-1/ ASME FFS-1 is shown in Fig. 4

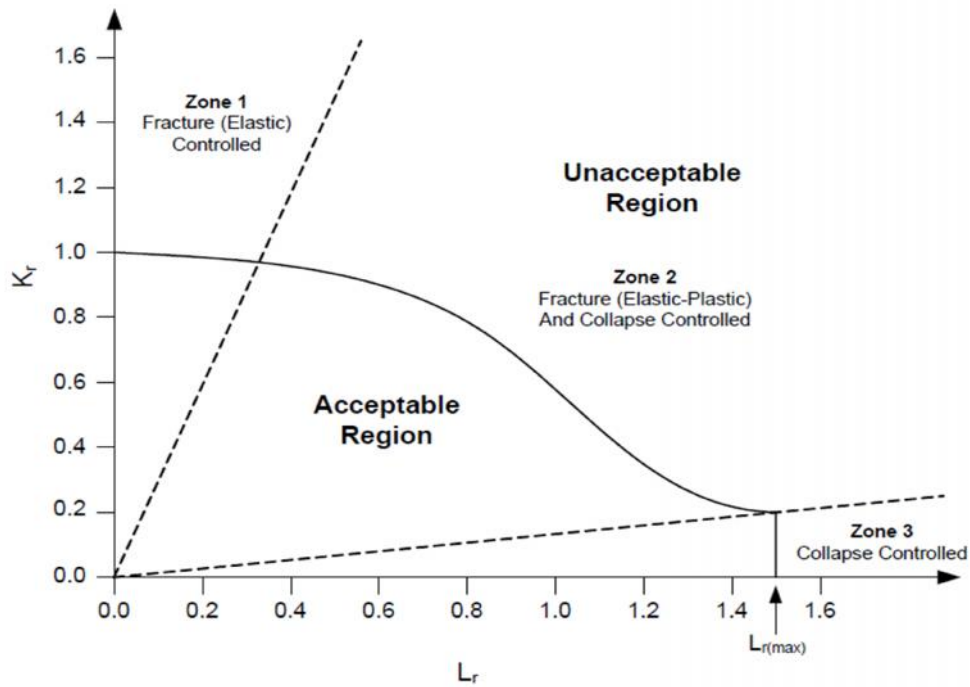


**Fig. 4 Failure regions on the Failure Assessment Diagram [18]**

### 1.2.3.2 Shakedown analysis of cracked structures

Feng and Gross [34] developed a simple approach to address the problem of SD analysis of defected components. They introduced a two-step analytical solution: the first step is based on a global analysis by adopting the classical SD theorem

without introducing the crack, while the second step involves a local analysis by adopting the stress intensity factor. Feng and Gross [34] showed that microscopic defects like micro voids and micro cracks can be considered by introducing internal damage variables into SD theory. On the other hand, macro flaws have to be accounted for using the concepts of fracture mechanics because of the complexity of the damage and deformation around the crack tip.

Lower bound SD analysis of spherical shells containing defects was introduced by Mingde et al. [36]; they used the temperature parameter method with a linear programming model of the yield function in order to investigate the effect of part through slots and gas holes on both the limit and SD limit load of spherical shells. On the other hand Yinghua [35] investigated the influence of different configurations of part-through slots on the SD limit load by developing an analytical simplified technique that was validated afterwards by numerical analyses and he concluded that the use of the developed technique yielded good results as compared with numerical analyses.

### **1.2.3.3 Limit load analysis of cracked pipe bends**

Limit load determination of cracked pipe bends have drawn a lot of concern in the recent years. Yahiaoui et. al [37] performed FE analyses to assess the limit load of cracked short radius pipe bends. Internal pressure and in-plane bending were applied to pipe bends with circumferential cracks at the intrados or meridional cracks at the crown. Crack position was decided following a previous study of the same authors [38] which found that under dynamic bending and steady pressure cracks usually initiate meridionally at the crown and circumferentially at the intrados. Two techniques were used to model the crack into 3D continuum elements: the node

release method and collapsed elements method. The limit load was taken as the plateau of the moment-displacement curve. Moment was taken as the product of the reaction force at the neutral axis end node and the lever arm which is the distance between the load application point and the pipe bend centre line. Yahiaoui et. al [37] concluded that pipe bends can tolerate the presence of cracks without dramatic reductions in limit load leaving aside the possibility of fast fracture. Only deep cracks or through wall cracks have a substantial influence on the limit load of cracked pipe bends.

In the work of Yahiaoui et. al [17], FE plastic loads were compared with experimental test outcomes of pipe bends with different crack configurations and positions. Cracks were introduced using electric discharge machining for experimental tests and using node release method for FE models. Plastic loads were obtained using TES method from moment-displacement curves using elastic-strain hardening material model and large deformation (non Linear) assumption. The elbow was attached to tangent straight pipes with length equal to four times the outer diameter of the pipe bend; this was to ensure elimination of the induced shear due to the load application method. Yahiaoui et. al [17] FE results were in good agreement with experimental outcomes as FE analyses were based on the nominal pipe bend dimensions while experimental models were usually a little thicker. It was concluded that dramatic reduction in limit load of cracked pipe bends under in-plane bending can only exist if the cracks were circumferential, through wall, and with large subtended angle.

Yahiaoui et. al. [39] summarized the experimental results obtained by the same authors [17, 37] for cracked pipe bends under opening bending. Comparison

with the existing results by others was also introduced. Yahiaoui et. al. [39] presented the experimental limit loads of 13 models with through wall or part penetrating cracks at the intrados, extrados (circumferential) or crown (meridional) subjected to in-plane opening bending moment. They quoted the results of Miller [40] and Zahoor [41] and came with a conclusion that the existing results were conservative after comparison with the experimental outcomes. Yahiaoui et. al. [39] concluded that both meridional and circumferential part-through cracks and through-wall meridional cracks has little effect on the limit load of pipe bends whereas through-wall circumferential cracks have significant effect on limit load of pipe bends.

On the other hand, Kim et. al. [42] studied the effect of circumferential through wall cracks on pipe bends under in-plane bending. They assumed elastic-perfectly plastic material model. Both small deformation and large deformation assumptions were investigated. Based on FE results, they came up with closed form approximations of the plastic loads and compared them with existing solutions of Miller [40]. They found that Miller solutions were unduly over conservative and also neglected the effect of some bend parameters on the plastic loads.

Chattopadhaya et. al. [43] performed experimental tests of cracked ferritic and austenitic pipes and elbows. Various sets of geometries and crack configurations were considered under the combined effect of internal pressure and bending moments. Experimental outcomes were compared with existing analytical solutions of Miller [40], Zahor [41], and Chattopadhaya et. al. [44] and also with R6 approach [45]. Chattopadhaya et. al. [30] came to the conclusions that the equations of Zahoor and Miller neglected the difference between the opening and closing bending moments that is why they recommended the use of Chattopadhaya et. al.[43] equation that

distinguished between the types of loadings. They also found that the R6 method accurately predicted the crack initiation load as evidenced by experimental findings.

Simha [46] used the existing solutions of limit loads for elbows with through wall or part through meridional or circumferential cracks subjected to internal pressure only, In-Plane moment only, or the combined effect of both loads in conjunction with a load interaction formula developed by Goodall [47] for flawed elbows. Simha [46] introduced load interaction curves for flawed elbows and compared the results with the available experimental limit loads in the literature after accounting for the uncertainties in experimental limit loads. Simha [46] estimated the uncertainty in experimental limit loads to be about 25%. The load interaction curves obtained agreed well with the experimental results in most of the cases considered in his work. Simha [46] observed that the presence of through wall meridional cracks does not affect the limit load of elbows subjected to In-plane bending meanwhile through wall and part through circumferential cracks affect the limit load of elbows subjected to both internal pressure and or in-plane bending.

All the previous studies investigated the global response of the structure containing defects; However, Yahiaoui et. al [48] determined the local limit load of thirteen test models (together with FE simulation) of pipe bends that contain cracks with different configurations ranging from shallow to through-wall cracks. The term Local limit load is defined as the load causing failure of the crack ligament. Yahiaoui et. al [48] reported that some model data had initial normal behavior followed by "double back" response which can be attributed to the debonding of strain gauges as the load is increased. Local plastic loads were obtained using TES method from strain data and compared to the global response from load-displacement curves. Local limit loads were always lower than those obtained from global analysis. They came up to

the general conclusion that the determination of the local plastic loads of cracked components is not considered to be feasible because of the difficulties encountered in experimental testing and that only detailed FE analyses can account for local Limit load determination.

#### **1.2.4 Line spring model**

Line Spring Elements (LSE) allow the determination of J-integral with a dramatic reduction in the computational cost "one order of magnitude" as compared to 3D FE analyses. LSE were introduced by Rice and Levy [49-50] and improved by Parks [51-52]; the element formulation is based on the idea of simulating the stiffness reduction because of surface cracks by spring stiffness applied at the position of discontinuity. Both membrane forces and bending moments are transduced using the spring stiffness as a function of crack depth at the nodes per unit crack length. This simulation resembles the single edge notched plate under tensile and bending loads with plain strain assumption. More details about the LSE formulations is presented in Appendix (C).

Goncalves et. al. [53] provided a summary of the theory behind the Line Spring Model and utilized the model to obtain the stress intensity factors for plates with semi elliptical cracks and also for plates with corner cracks at central hole. They used the elements LS3S and LS6 found in the element library of ABAQUS commercial finite element package [54] and can be used to model part through cracks in conjugate with quadratic shell elements as shown in Fig. 5. The prevailing conclusion of the data presented by Goncalves et. al. [53] is that the line spring model does not take into account the curvature of the crack front and gives inaccurate results when the crack intersects with the free surface, but for the other points away from the

free surface the line spring model gave very accurate stress intensity factors as compared to 3D FE analyses.

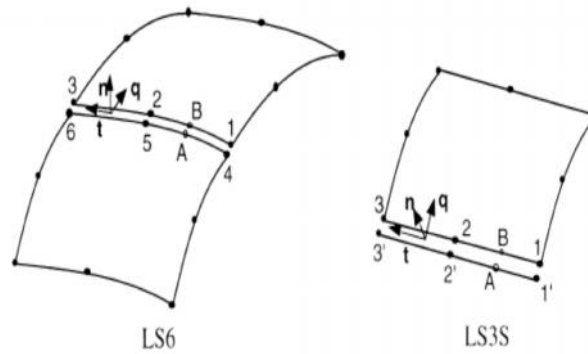


**Fig. 5 Schematic illustration of LSE (LS6 and LS3S) connected to eight node shell elements (S8R) [53]**

Sauter et. al. [55] investigated the fracture mechanics parameters of cracked pipe bends using two methods: 2D line spring model and 3D collapsed continuum elements. J-integrals calculated using LSE were compared to those obtained from 3D FE analyses that were based on the concept of virtual crack extension and contour integrals by calculating the change in total potential energy stored in the structure due to virtual crack propagation. Singularity in the crack tip was simulated by quarter point elements surrounding the crack tip [60]. Sauter et. al.[55] concluded that LSE results agreed very well with those obtained using 3D FE analyses and that a great deal of computational cost can be saved by using LSE to simulate cracks in different structures. LSE models have the advantage of the ability to change the crack depth at each node with a single input data being changed without the need to re-mesh the model every time it is required to alter the crack depth which is inevitable in 3D FE analyses.

### 1.3 Objectives

The current work has two main objectives: To obtain the shakedown limit loads of cracked pipe bends through the simplified technique [19] and to propose a procedure for generating the Failure Assessment Diagrams (FAD) of cracked pipe bends for the use in accordance with the ASME FFS-1 API 579 Fitness for Service code. The proposed FAD is based on the J-integral output from FE analyses and the SD limit load obtained by the simplified technique.

The effect of crack size and position on the SD limit and FAD of cracked pipe bends is investigated. Both short ( $\Theta = 45^\circ$ ) and long ( $\Theta = 120^\circ$ ) circumferential cracks on the pipe bend intrados are introduced for IPO bending moments, while short and long circumferential cracks on the pipe bend extrados are introduced for IPC bending moments.

Two crack depth to thickness ratios ( $b/t = 0.5$  or  $0.75$ ) are investigated and their effect on the SD limit load is discussed, and compared with the defect free pipe bend. The proposed FAD is generated for all the points included in the Bree diagram obtained utilizing the simplified technique.

### 1.4 Thesis outlines

After clearly presenting the technical background and the objectives of the current work, the modelling and analysis chapter includes the FE models descriptions and also the material models utilized. In order to gain confidence on the developed models, various verifications studies are conducted. Fracture mechanics verification studies are conducted in order to compare the Stress Intensity Factor (SIF) provided

by the LSE by the analytical and numerical results provided by the stress intensity factors handbook [57].

Two models having different crack configurations are studied: plate with central surface crack under uniaxial tensile load and thick cylinder with longitudinal part-through crack under internal pressure. The SD limit load obtained by Feng and Gross [34] by introducing the SIF into the classical SD theorem is compared versus the SD limit obtained in the current work using the LSE and the simplified Technique. Limit load verification study is conducted and the FE outcomes of the current work are compared to the limit load experimental test outcomes of Yahiaoui et. al. [17]. The FE outcomes showed confidence in the developed FE models utilized within the current research compared to the experimental test outcomes of limit load and the analytical and numerical results of SIF.

The results and discussion chapter includes all the interaction diagrams (Bree) for all the models with different crack configurations. Comparisons between the different crack configurations and their effect on the SD boundary are discussed. The different behaviour of the cracked pipe bends under the combined effect of steady internal pressure and IPO or IPC bending moment is also discussed. The Failure Assessment Diagram (FAD) is also obtained for the cracked pipe bend models as well as the crack growth analysis based on the FAD and Paris law. The general conclusion drawn from the results of the current work and also recommendation for future work is given in chapter 4.

## CHAPTER 2

### MODELING AND ANALYSIS

In this chapter, the detailed methodology of the current research is presented. The FE models adopted in this study that resembled the experimental models of Yahiaoui et. al. [17] are described. The critical positions selected to introduce postulated cracks have been decided based upon the literature review. It was shown that IPO bending moments would open circumferential cracks at the intrados or meridional cracks at the crown; however, IPC bending moments would open circumferential cracks at the extrados. The boundary and loading conditions are discussed in detail and mesh convergence checks are presented.

The procedure for obtaining the Bree diagrams utilizing the simplified technique [19] and the FAD using the J-integral output from FE analyses is introduced. Both short circumferential cracks that have  $45^\circ$  subtended angle ( $\Theta$ ) and long circumferential cracks that have  $120^\circ$  subtended angle are considered under either IPO or IPC bending moments together with internal pressure. The effect of crack size and position is investigated under two different loading conditions and the corresponding Bree and FAD of each case are developed.

In order to validate the modelling techniques adopted in the current work that utilized the LSE, verification studies have been conducted, namely, SIF verification study that is based on comparing the SIF output of the LSE by the analytical and numerical results found in the stress intensity factors handbook [57]. The second verification study is based on comparing the SIF and SD limit load obtained by Feng

and Gross [54] for a thick cylinder with part-through longitudinal crack with the results obtained for the same model adopting the LSE and the simplified technique. The third verification study was comparing the FE limit load analyses adopted in in the present work against the experimental and numerical limit loads obtained by Yahiaoui et. al. [17] for meridionally and circumferentially cracked pipe bends.

## 2.1 Models description

Pipe bends are classified by the bend angle and the bend radius. Pipe bends that have a bend radius ( $R$ ) that is 1.5 times or more the pipe mean diameter ( $d_m$ ) is termed long-radius pipe bend on contrast to the pipe bend geometrical configuration that is investigated in this thesis which is short radius pipe bend. Bend angles available in the market are 30, 60, and 90-degree; however, the most common pipe bend angle is the 90-degree. A typical 90-degree pipe bend with major sectioning lines on the meridional direction that is used later to define the critical positions to introduce postulated cracks is shown in Fig. 6. Postulated cracks positions is decided based on the loading type that initiates crack opening. The geometry and crack configurations of the pipe bends FE models are the same as the experimental models tested by Yahiaoui et. al. [17]. The pipe bend investigated was a 3 in. NPS, schedule 40, 90-degree short-radius welding elbow with nominal dimensions summarized in Table 1.

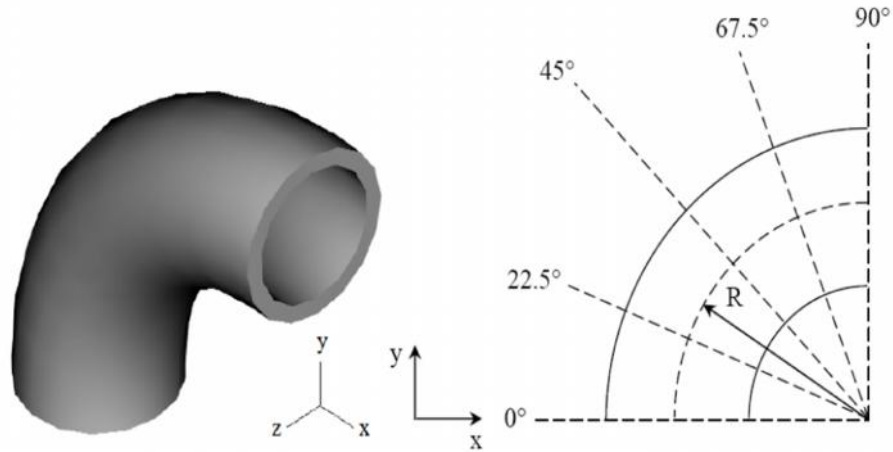


**Fig. 6 Schematic drawing showing a typical 90-degree pipe bend and major line sectioning the pipe bend meridional direction [4]**

**Table 1 Pipe bend (90-degree Sch. 40) geometry**

$D_m$ (mm)	83.41
$t$ (mm)	5.49
$R$ (mm)	76.2
$L$ (mm)	355.6

Two FE models were used to resemble the experimental setup of Yahiaoui et. al. [17]. A schematic drawing of the experimental models is shown in Fig. 7 and the notation for cracked pipe bends is shown in Fig. 8 and Fig. 9. The first model utilized in this study is a quarter model incorporating symmetry boundary conditions on two planes of symmetry; this model is used for pipe bends with external circumferential crack at the intrados subjected to IPO bending or external circumferential cracks at the extrados subjected to IPC bending. The second model is full model of the pipe bend having external meridional crack at the crown.

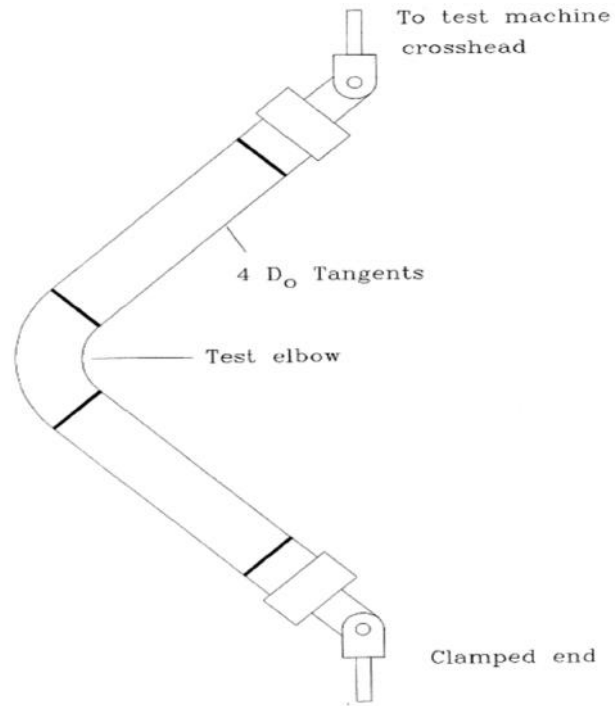


Fig. 7 Experimental setup [17]

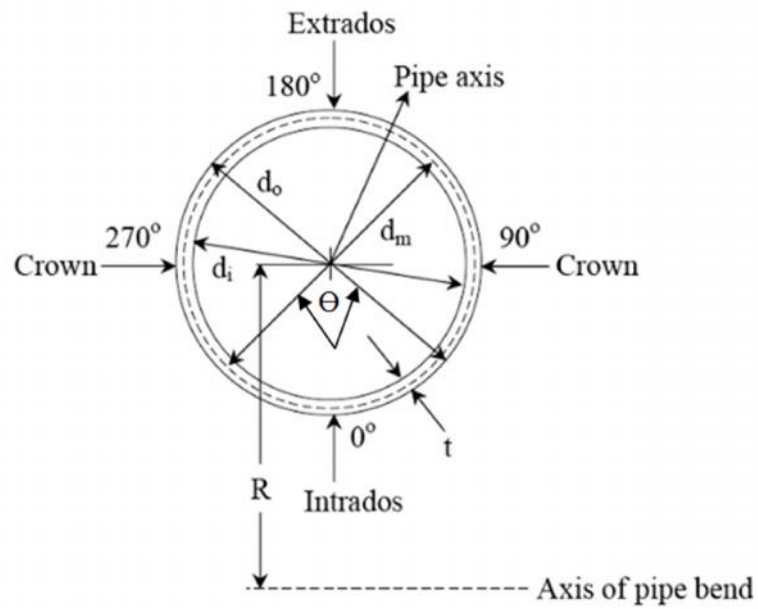
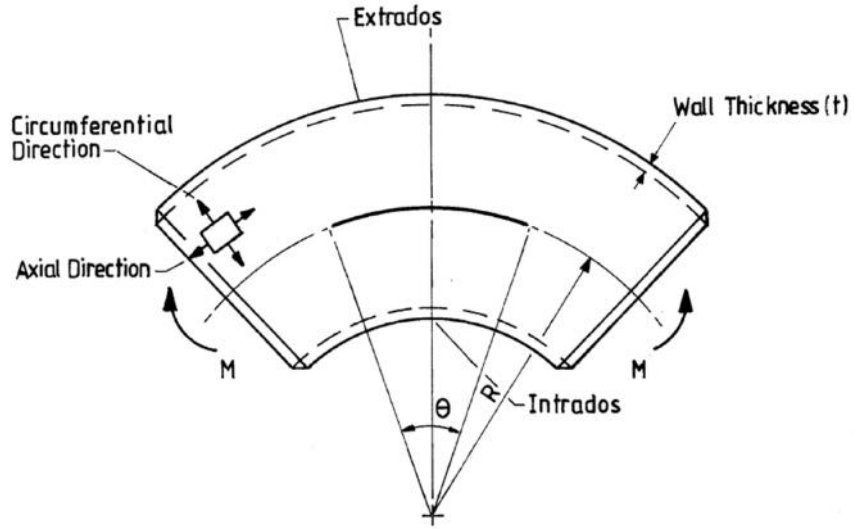
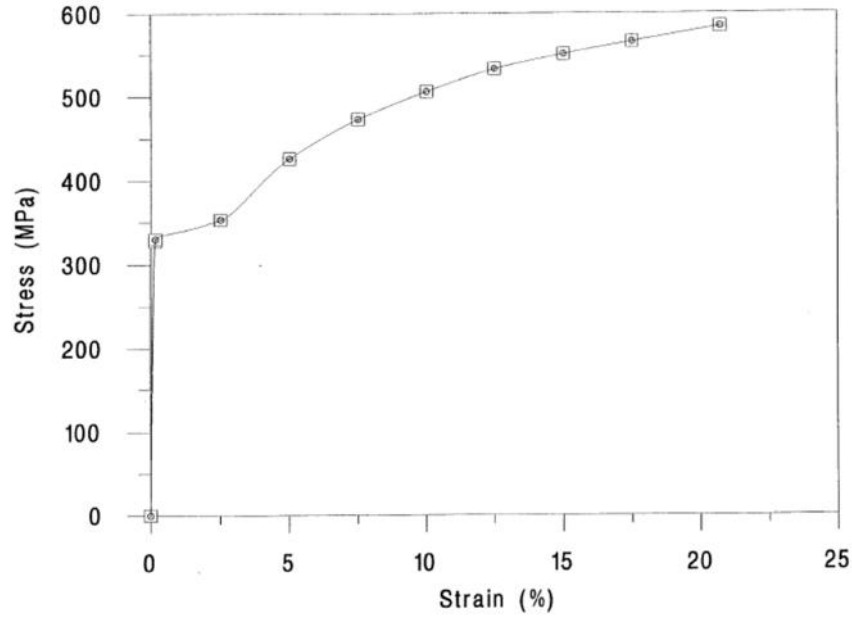


Fig. 8 Notation for circumferentially cracked pipe bends



**Fig. 9 Notation for meridionally cracked pipe bends [17]**

The pipe bend material is a typical piping carbon steel to the specification ASTM 234 WP. The material properties were obtained from tensile tests of specimens taken from the flanks of the pipe bend. The true stress-strain curve of the material is shown in Fig. 10 and a summary of the properties is given in Table 2. The elastic-perfectly plastic (EPP) material model was adopted in the limit load determination, but the real material properties were used in part of the verification study as given in Sec. 2.3.



**Fig. 10 True Stress-Strain curve of the material tested by Yahiaoui et. al. [17]**

**Table 2 Pipe bend material properties**

$E$ (GPa)	210.0
$\gamma_0$ (MPa)	328.0
$\nu$	0.3

The pipe bend geometry is meshed with 8-noded reduced integration shell elements (S8R). The S8R element has four integration points and five section points (integration points) through thickness. Section point 1 (SP1) lies on the outer surface of the element, SP3 lies on the middle of the element, and SP5 lies on the inner surface of the element. Part through cracks are modeled by LSE. The elements LS3S and LS6 are found in the element library of ABAQUS [54] and can be used to model part through cracks in conjugate with quadratic shell elements (S8R). The element

type LS6 is used to simulate part-through cracks that lie outside a plane of symmetry while the LS3S element is used to model cracks on the planes of symmetry.

The geometry of the quarter models is shown in f . The quarter model (Fig. 12) has symmetry boundary conditions on the edges denoted by B (Z-Symmetry) and C (Y-Symmetry) while the edge D that has the LSE was free to allow crack opening under loading. The point of load application A was kinematically coupled with all the nodes on the edge E. The point of load application in the quarter model (A) as shown in Fig. 13 was assigned a Z-rotation boundary condition while restrained to move in X-displacement only to prevent rigid body motion.

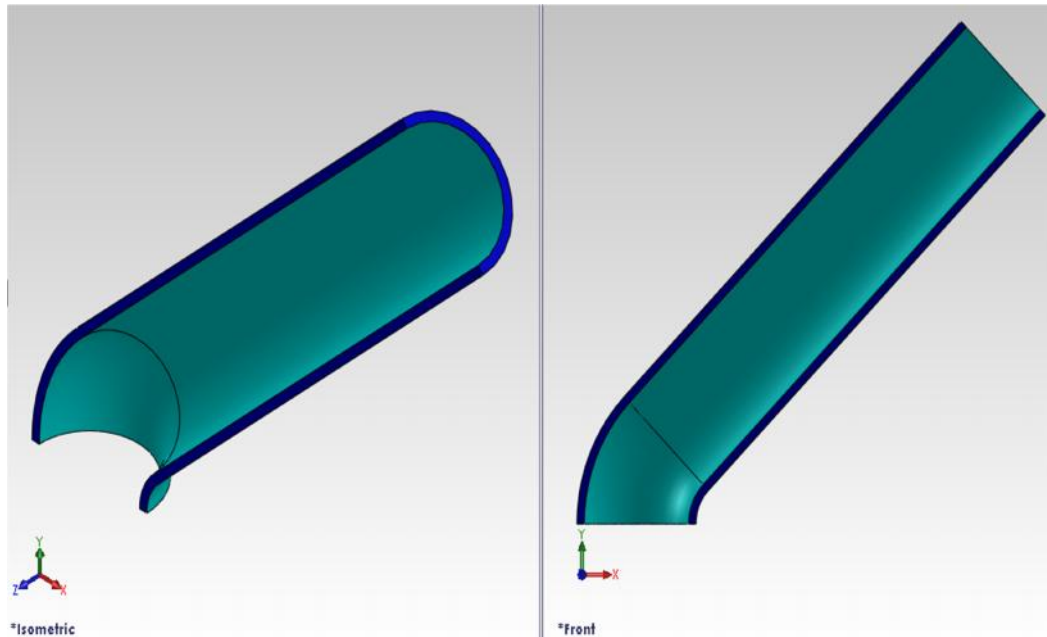


**Fig. 11 Pipe bend quarter model geometry**

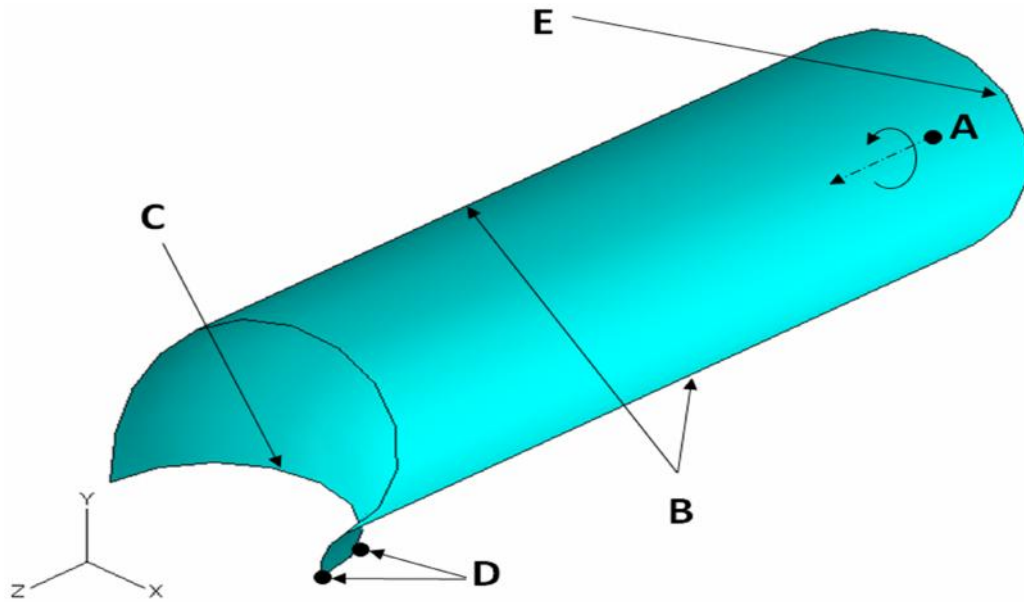


**Fig. 12 Quarter model of the pipe bend that is used to introduce external circumferential crack on the intrados**

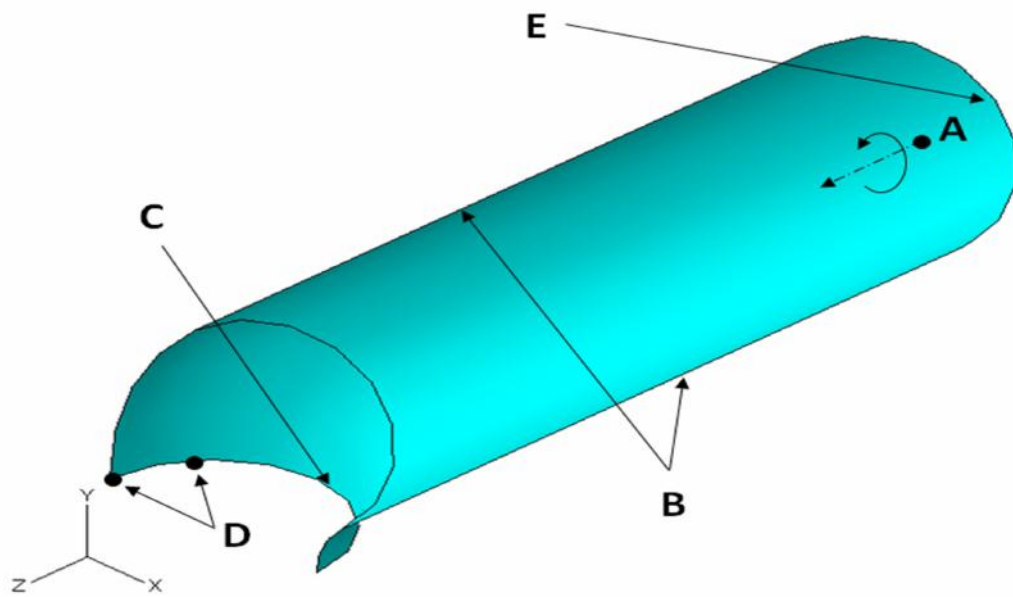


**Fig. 13 Quarter model of the pipe bend that is used to introduce external circumferential crack on the extrados**

## 2.2 Stress intensity factor verification study

In order to gain confidence on the fracture mechanics parameters obtained by LSE, a SIF verification study was performed. A square plate of 100 mm side (L) and thickness (t) of 10 mm with central semielliptical crack of 0.4t depth is uniaxially loaded in a way that incorporate Mode I crack opening. The geometry is meshed with 8-noded reduced integration shell elements (S8R).

Two models are considered: the first is a full model in order to use LS6 element to simulate part-through crack and the second is a quarter model that has two planes of symmetry in order to use the element LS3S. Linear Elastic Fracture Mechanics (LEFM) was only considered and the Stress Intensity Factors (SIF) were obtained utilizing the LSE for all the nodes that lie on the crack front. Several models of the same geometry, but of different meshes have been developed and simple optimization process is conducted to minimize the number of degrees of freedom without affecting the accuracy of the solution. Upon conducting several mesh convergence checks, it was found that modeling the plate full model with 5500 shell elements and 28 LSE (16789 Node) and the quarter model with 1375 shell elements and 14 LSE (4256 Nodes) provided adequate results..

Displacement boundary conditions of the quarter model include constraining the nodes lying on edge (EC) shown in Fig. 14 in Y Direction and the same edge is restrained against rotation about the X and Z-direction. The nodes lying on edge AD are restrained against translation in the X-direction and rotation about both the Y- and Z- axes and the node at corner (B) is constrained in z-direction thereby imposing geometric symmetry about the XZ-plane and YZ plane and also preventing the rigid body motion. The Edge DE that has the LSE is free to move in the Y-Direction to

allow crack opening under loading. The uniaxial tensile stress that will cause crack opening is applied on edge AB by Shell Edge Load (SEL)

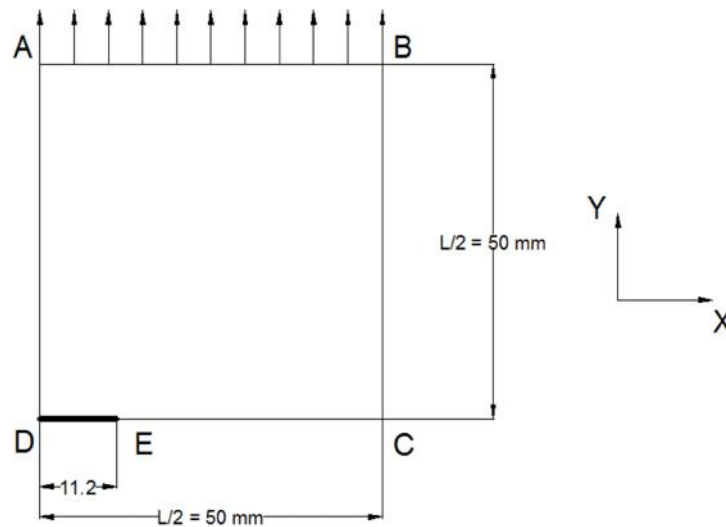


**Fig. 14 Quarter model of the plate with central surface crack**

Displacement boundary conditions of the full model include constraining the nodes lying on edge (DC) shown in Fig. 15 in the Y-Direction. The node lying at the midpoint of edge DC is restrained against translation in the X-direction Z-direction and rotation about the X, Y, and Z- axes thereby preventing the rigid body motion and allowing the plate to stretch in Y-direction and contract in Z and X direction. The uniaxial tensile stress that will cause crack opening is applied on Edge AB by Shell Edge Load (SEL).

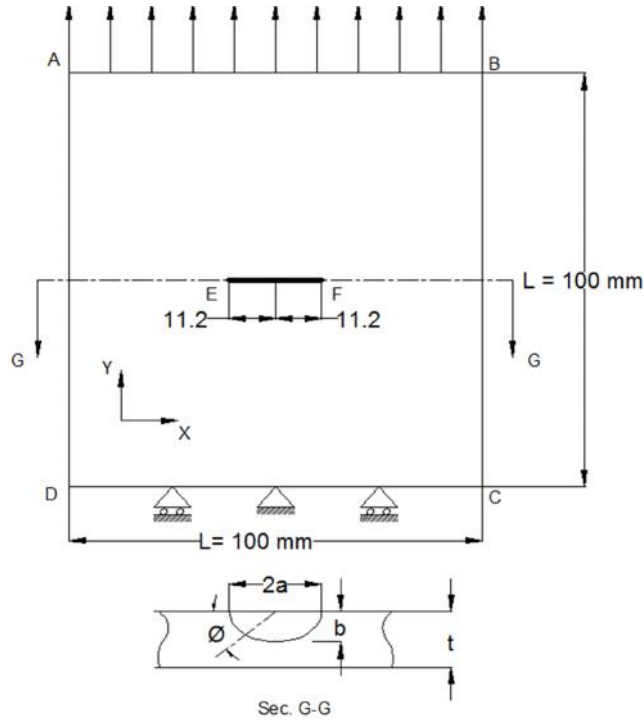


**Fig. 15 Full model of the plate with central surface crack**

The stress intensity factors obtained from the two aforementioned models were compared to those obtained by Raju and Newman [56] found in the Stress Intensity Factors Handbook [57]. The equation used by Raju and Newman [56] to calculate the stress intensity factors is given as follows:

$$K_I = F \sigma \sqrt{\pi b} \quad (3)$$

Where  $K_I$  is the mode I stress intensity factor,  $F$  is boundary correction factors for semi-elliptical surface cracks subjected to tension,  $\sigma$  is the applied stress,  $b$  is the crack depth. The obtained SIF were agreeing with the results presented by Raju and Newman [43] as can be seen in Table 3.

**Table 3 Stress Intensity Factors verification study summary**

Raju and Newman [56]				Current work			% deviation (I) (2-1/1)%	% deviation (II) (3-1/1)%
$2\phi/\pi$	b/a	b/t	F	1	2	3		
				K	K (MPa. $\sqrt{\text{mm}}$ ) Full Model (I)	K (MPa. $\sqrt{\text{mm}}$ ) Quarter Model (II)		
0.25	0.36	0.4	0.83	58.6	68.7	68.1	17.3%	16.3%
0.5			0.96	68.3	76.2	76.3	11.6%	11.2%
0.75			1.07	76.1	79.4	79.5	4.3%	4.5%
1			1.11	79	80.5	80.8	1.9%	2.2%

The deformed shape of the plate with central crack full model at SP1 (the lower surface that has the crack ligament) is shown in Fig. 16 while the quarter model at SP5 (the upper surface that has the crack tip-free surface intersection) is shown in Fig. 17. It is worth mentioning that the critical points lie on the midpoint of the crack ligament in the lower surface and also in the crack tip for the upper surface.

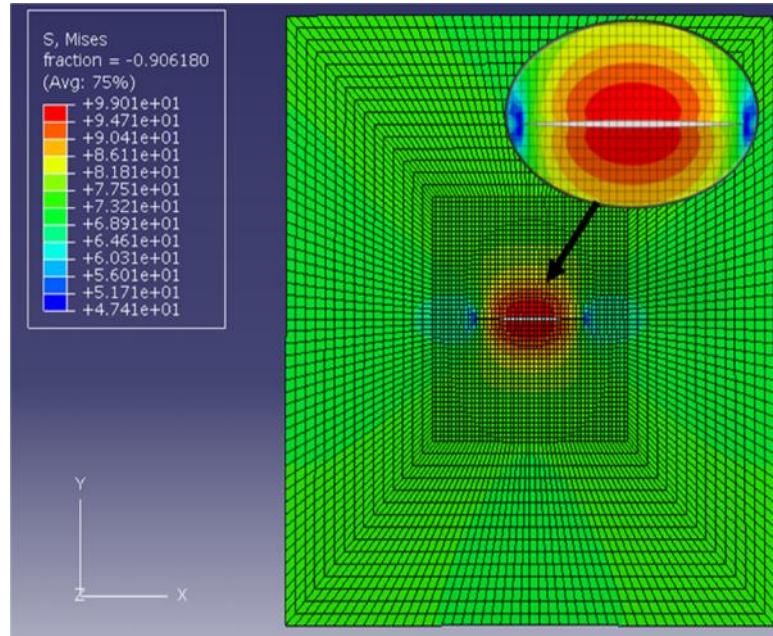


**Fig. 16 Deformed shape and stress contours of the full model utilizing the element LS6 at SP1 (crack ligament)**

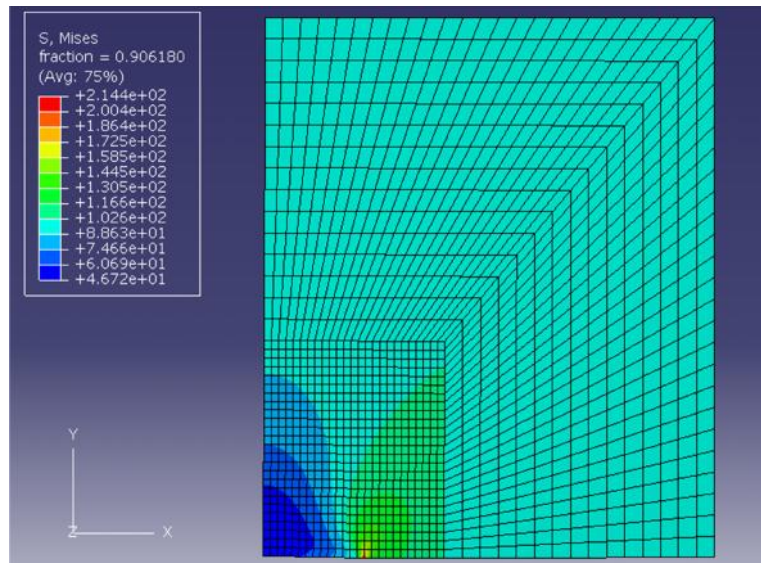


**Fig. 17 Deformed shape and stress contours of the quarter model utilizing the element LS3S at SP5 (crack tip)**

### 2.3 Shakedown limit verification study

Feng and Gross [34] utilized the SIF obtained by Raju and Newman [58] and presented a technique to determine the SD limit load. They applied the technique on two problems: plate with central crack subjected to biaxial tensile load and thick cylinders with longitudinal part-through internal cracks subjected to internal pressure. They obtained the global response SD limit pressure of the thick cylinder by utilizing the static SD theorem and then presented the SIF to obtain a local SD limit load around the crack front. The SD limit load obtained by the simplified technique which is elaborated in detail in Sec. 2.5 and using the LSE is compared with the outcomes of Feng and Gross [34] for the following case:

- Thick cylinder with longitudinal semi elliptic crack
  - $t$  (thickness) = 100 mm
  - $R_i$  (inner radius) = 350 mm
  - $L$  (length) = 2000 mm
  - $b$  (crack depth) = 60 mm
  - $a$  (crack length) = 150 mm
- Material (EPP)
  - $\sigma_y = 262$  MPa
  - $E = 200$  GPa
  - $\nu = 0.3$

The Finite Element (FE) model of the thick cylinder with longitudinal internal crack is shown in Fig. 18. Only one quarter of the cylinder is modeled because of the virtue of having two planes of symmetry (XZ-plane and XY plane). Symmetry boundary condition about X-axis is applied on the edge denoted by A while the edge denoted by B is subjected to symmetry boundary condition about Z-axis. The point C

is constrained to move in Y-direction in order to prevent the rigid body motion. The edge denoted by D will be subjected to SEL in order to simulate the capping. The edge denoted by (E) that will have the LSE is free in order to allow crack opening under loading. The length of the thick cylinder is chosen to be long enough ( $l/a \geq 10$ ) in order to have a negligible effect on the SIF. The deformed shape of the thick cylinder with longitudinal crack under internal pressure is shown in Fig. 19. It can be seen that the presence of crack has caused a stress concentration region around the crack front. It is worth mentioning that the use of shell elements (S8R) to model thick shells involves approximation. However, the ABAQUS elements library manual stated that the element S8R is mainly used to model thick shells in contrast to the element S4R that is a general purpose element used to model both thin and thick shells. In order to overcome this approximation, a large number of through-thickness integration points (section points) is used.

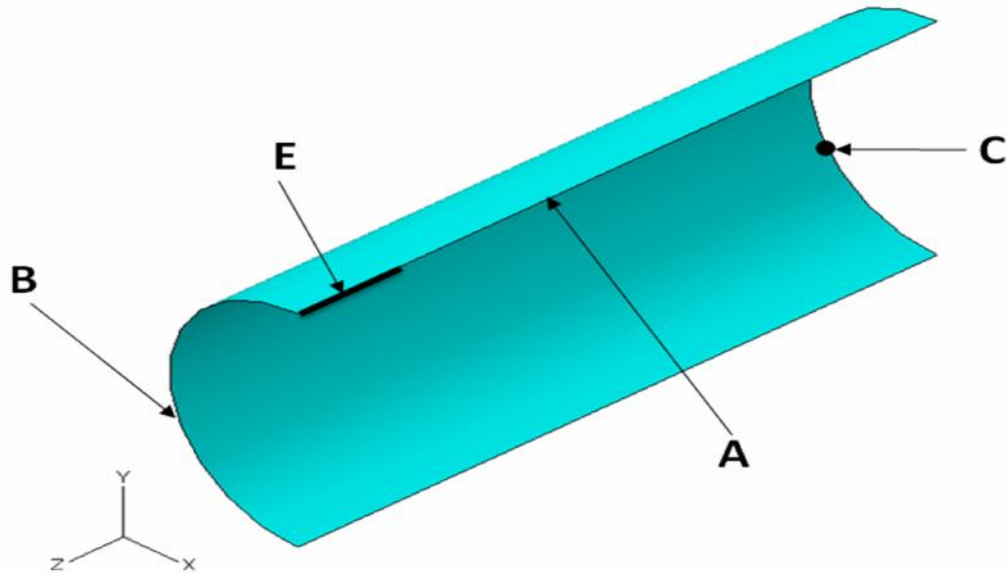


**Fig. 18 Geometry and Boundary conditions annotations of the thick cylinder with longitudinal part through crack under internal pressure**

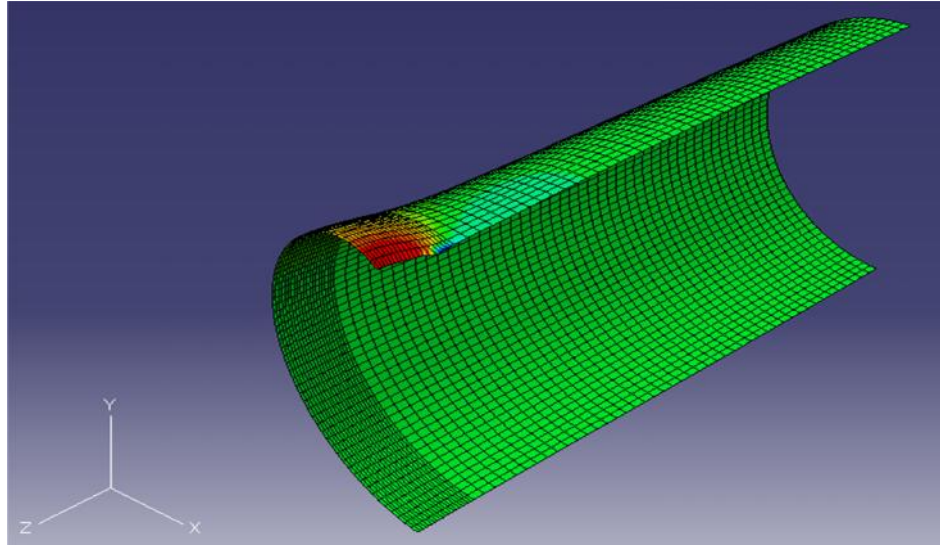


**Fig. 19 Deformed shape of the thick cylinder with longitudinal part through crack under internal pressure**

The Stress Intensity Factor (SIF) of the thick cylinder with internal crack subjected to internal pressure obtained by Raju and Newman [58] is given by Eq. 4.

$$K_I = \frac{PR_i}{t} \sqrt{\pi \frac{b}{Q}} F_i \left( \frac{b}{a}, \frac{b}{t}, \frac{t}{R}, \phi \right) \quad (4)$$

The complete elliptic integral (Q) is given by Eq. 5 and the shape modification factor ( $F_i$ ) is given by Eq. 6. The influence coefficients ( $G_j$ ) that are used to obtain the shape factor are obtained from the tables provided by Raju and Newman [58].

$$Q = 1 + 1.464 \left( \frac{b}{l} \right)^{1.65} \quad (5)$$

$$F_i = \frac{t}{R_i} \left( \frac{R_0^2}{R_0^2 - R_i^2} \right) \left[ 2G_0 - 2 \left( \frac{b}{R_i} \right) G_1 + 3 \left( \frac{b}{R_i} \right)^2 G_2 - 3 \left( \frac{b}{R_i} \right)^3 G_3 \right] \quad (6)$$

The SIF obtained using the LSE is compared to the SIF obtained from 3D FE analyses as given by Raju and Newman [57] and the SD limit pressure obtained using the simplified technique is compared to the outcome of Feng and Gross [34]. A

summary of the SD limit verification study is given in table 4. It can be observed that the outcomes of the current work agree with the SD limit pressure obtained by Feng and Gross [34] and also with the SIF obtained by Raju and Newman [58] as can be seen in table 4.

**Table 4 Shakedown limit verification study**

	1	2	Deviation (2-1)/2 %
	Current work	Feng and Gross [34]	
Stress Intensity Factor (MPa. $\frac{\sqrt{mm}}$ )	3834	4087.5	6.2%
Shakedown limit pressure (MPa)	42.18	48	12.13%

#### 2.4 Limit load verification study

Limit Load verification study was performed in order to gain confidence on the FE pipe bend model incorporating the LSE and to validate the limit load results with experimental outcomes obtained by Yahiaoui et. al. [17]. The pipe bend FE models that were discussed previously in Sec. 2.1 are used in the following section with some modifications in the boundary conditions in order to simulate the actual conditions of the experimental models.

The defect-free model is validated against the FE models that had the assumption of large deformation and also the experimental models tested by Yahiaoui et. al. [17]. Finite Element models of cracked pipe bends utilizing the line spring model and assuming EPP material model and small deformation are compared with experimental outcomes and also with the FE results having the same assumptions tested by Yahiaoui et. al. [17]. The following models were analyzed:

- Defect-Free Full Model (FMDF),

- Defect-Free Quarter Model (QMDF),
- Quarter Model with 45° Circumferential Crack on the intrados (QM45C),
- Quarter Model with 120° Circumferential Crack on the intrados (QM120C), and
- Full Model with 75° Meridional Crack on the crown (FM75A)

The boundary conditions and loading configuration of all the models were designed to simulate the actual conditions of the experimental testing. The quarter model (Fig. 20) has symmetry boundary conditions on the edges denoted by B (Z-Symmetry) and C (Y-Symmetry) while the edge D that has the LSE was free to allow crack opening under loading. The point of load application A was kinematically coupled with all the nodes on the edge E while constrained to displacement on X-direction to prevent the rigid body motion. A displacement boundary condition (Y-Direction) was applied at point A in order to calculate the bending moment by multiplying the resulted reaction force on Y-direction by the moment arm from point A to the center line of the pipe bend.

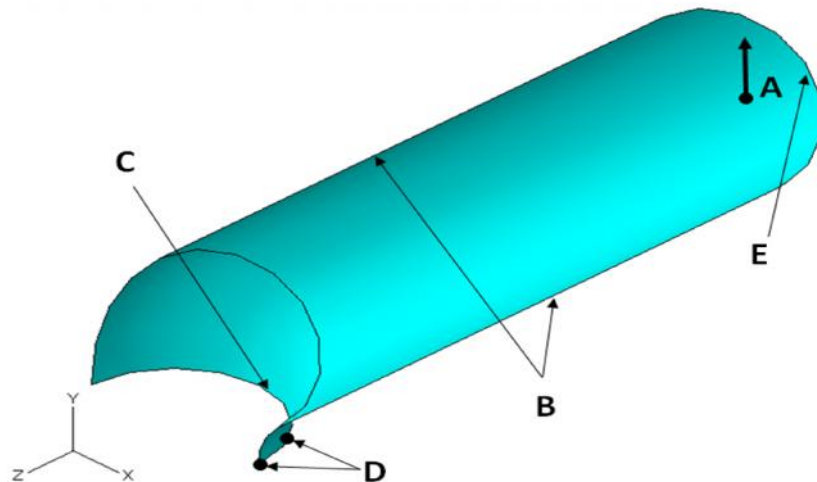


**Fig. 20 Quarter model of pipe bend that is used to introduce internal circumferential crack on the intrados.**

The full model (Fig. 21) boundary conditions were fixing the point of load application (C) in all the degrees of freedom except the translation in Y and rotation about Z while the point (B) was constrained in all the degrees of freedom except the rotation about Z. Both points B and C were kinematically coupled to the nodes at the end edges of the connecting straight pipes (A). The load is applied by the same way as previously shown for the quarter model.

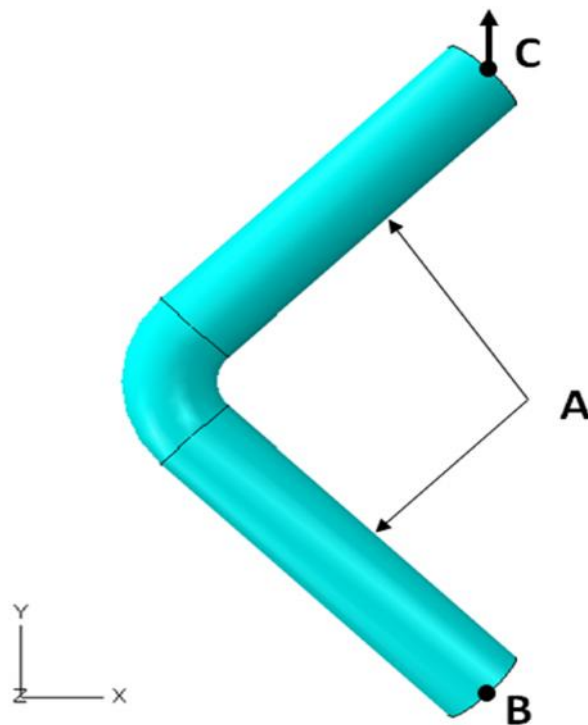


**Fig. 21 Full model of the pipe bend that is used to introduce internal meridional crack on the crown.**

The moment-displacement curve of the defect-free model adopting large deformation assumption is shown in Fig. 21. A sample representative moment-

displacement curve for the different models of the cracked pipe bends is shown in Fig. 23. The limit load of cracked pipe bends was defined as the plateau of the moment displacement curve which is the same definition adopted by Yahiaoui et. al. [17]. The outcome of the limit load verification study of the defect free model incorporating the material true properties and large deformation assumption is summarized in Table 5 while a summary of the results obtained for cracked pipe bends is given in Table 6.

The FE models investigated in the limit load verification study yielded satisfactory results that were agreeing with the experimental testing outcomes of Yahiaoui et. al. [17]. It should be noted that Yahiaoui et. al. [17] reported some experimental scatter and also the fact that the nominal pipe dimensions used in FE models were always lower than the actual dimensions of the experimental models as reported by Yahiaoui et. al. [17].

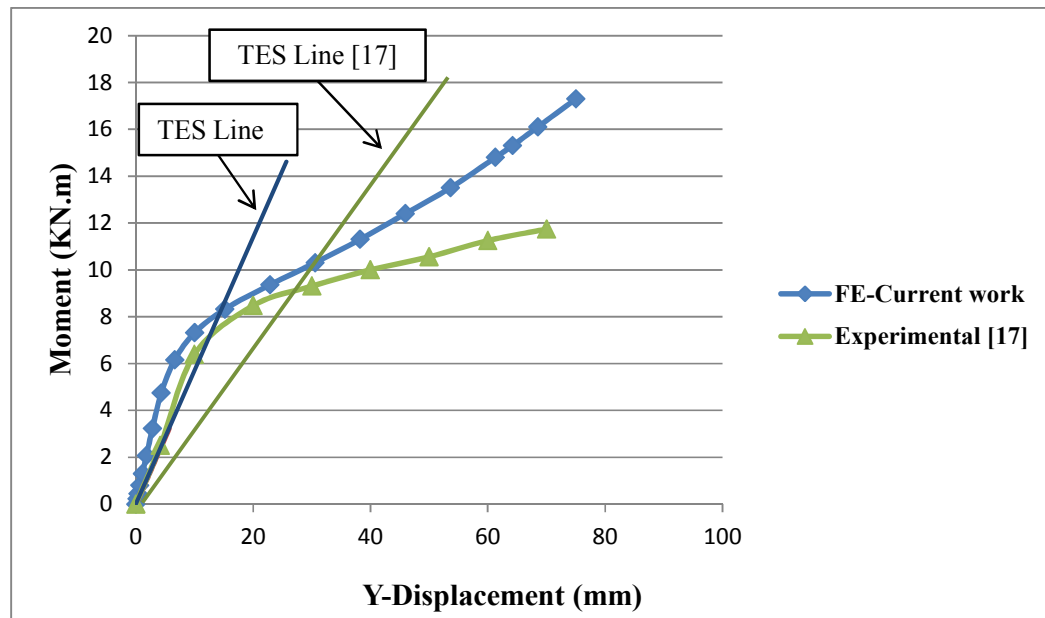


**Fig. 22 Moment-Displacement curve of the defect-free model assuming large deformation used to determine the limit load using TES method.**

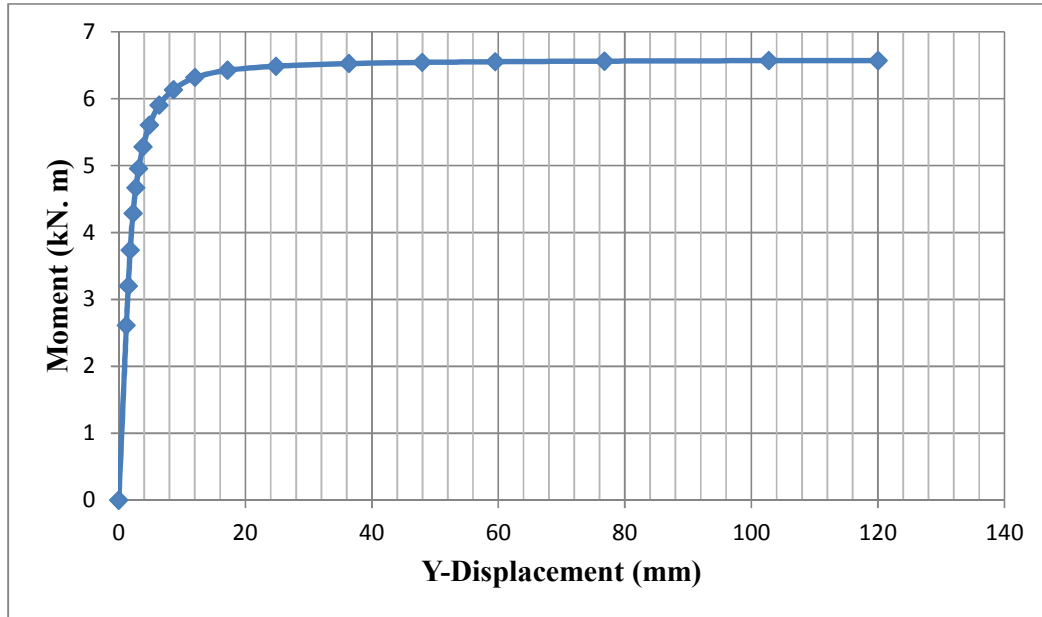


**Fig. 23 Moment-Displacement curve of QM120C model assuming small deformation used to determine the limit load.**

**Table 5 Defect-Free models assuming large deformation limit load verification study summary**

	1	2	3	4	5
	Experimental (Yahiaoui et.al.)	FE Large Deformation Strain Hardening (Yahiaoui et.al.)	FE Large Deformation Strain Hardening	(1-3)/1 %	(1-2)/1 % (Yahiaoui et.al.)
F MDF	9.01	8.27	8.2	8.99%	8.21%
Q MDF	XX	XX	8.2	8.99%	8.21%

**Table 6 Limit load verification study summary**

	1	2	3	4	5	6
	Experimental (Yahiaoui et.al.) (kN.m)	FE Small Deformation EPP Material (Yahiaoui et.al.) (kN.m)	FE Small Deformation EPP Material (Plateau) (kN.m)	(1-3)/1 %	(1-2)/1 % (Yahiaoui et.al.)	(3-2)/2 %
FMDF	9.01	7.72	7.65	15.09%	14.31%	0.91%
QMDF	XX	XX	7.66	14.98%	XX	0.78%
QM45C	7.84	7.71	7.62	2.81%	1.65%	1.17%
QM120C	7.75	6.84	6.56	15.35%	11.74%	4.09%
FM75C	8.09	7.38	7.15	11.62%	8.77%	3.12%

The deformed shape of the quarter model of the pipe bend with internal circumferential crack used to validate the results with the experimental models tested by Yahiaoui et. al. [17] is shown in Fig. 23. The critical point (A) is the crack tip at SP5 (inner Surface). The deformed shape of the full model of the pipe bend with internal meridional crack of  $\theta = 75^\circ$  is shown in Fig. 25. The critical point is at the crack tip at SP5. The LSE are denoted by B.

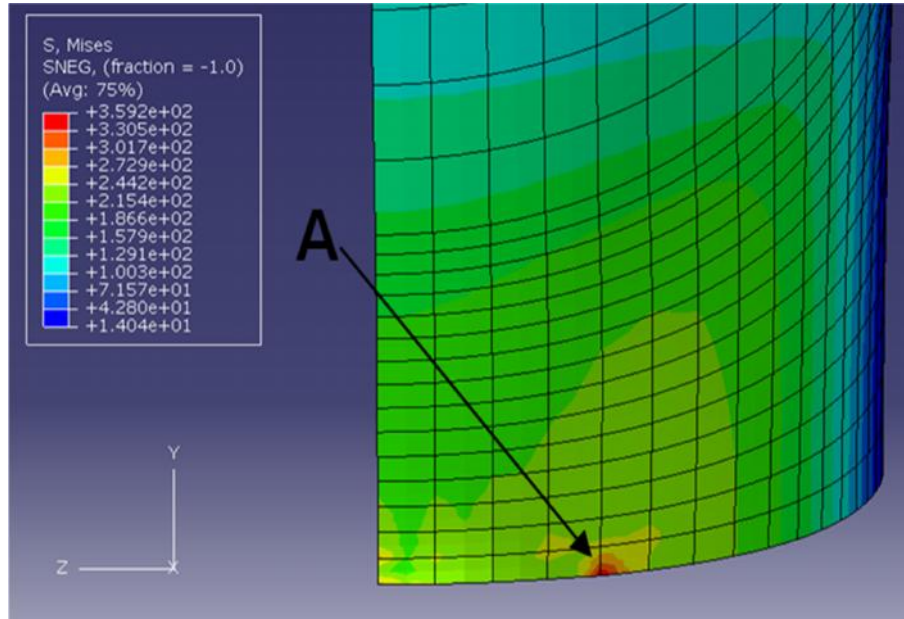


**Fig. 24 Deformed shape of the quarter model with internal circumferential crack**

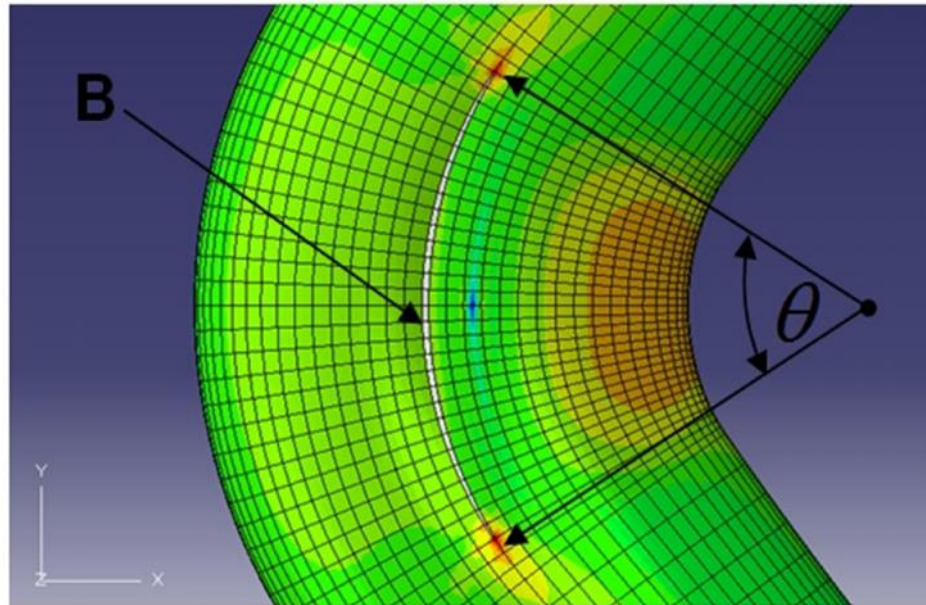


**Fig. 25 Deformed shape of the full model with internal meridional crack on the crown**

## 2.5 Application of the simplified technique

The simplified technique is utilized in order to generate the Bree diagrams of the previously described models. Two analyses were performed, namely, Elastic and Elastic-Plastic. The elastic analysis load is only the cyclic load component (bending moment) and it has only one solution increment. This analysis simulates the unloading of the loading-unloading cycle because the unloading is always elastic and it is performed only once and stored because it is common (with different stress magnitudes) for all the analyses required to generate the Bree diagram. The second analysis (Elastic-Plastic) of the technique consists of two sub steps: the first is applying the steady load (internal pressure) monotonically and the second step is applying the cyclic load (bending moment) monotonically while keeping the steady load applied. A schematic drawing of the simplified technique analyses is shown in Fig. 26.

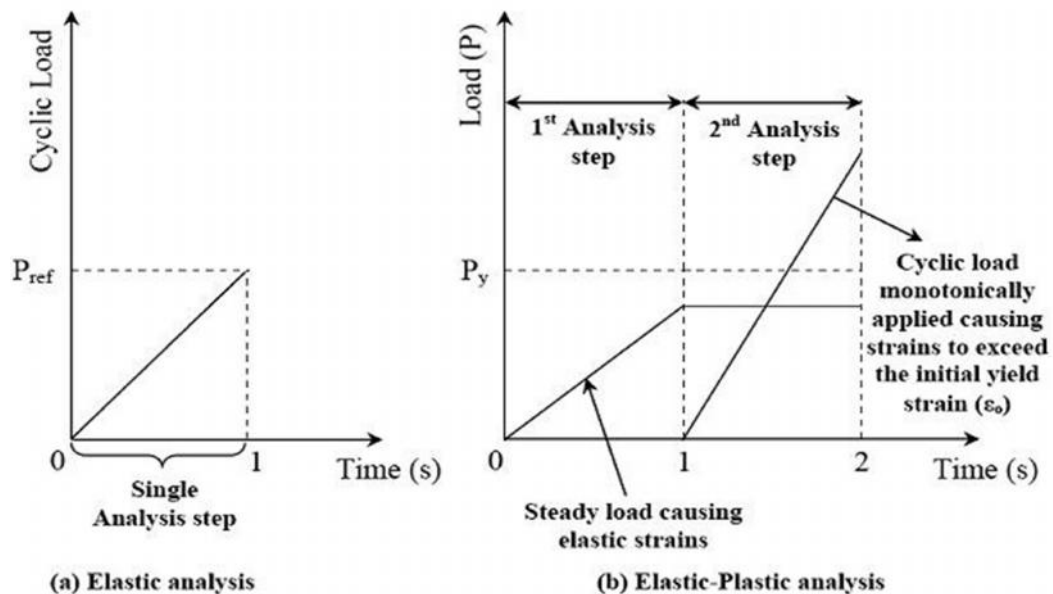


Fig. 26 Schematic representation of the simplified technique analyses [4]

The resulting residual stress for each loading increment is calculated by Eq.2 for each stress component for all the nodes. Mises equivalent residual stress is calculated by Eq.7 and then compared to the yield strength of the structure material. Lower bound SD limit load according to Melan's theorem is defined once the developed residual stress equals or is slightly less than the yield strength.

$$\sigma_{r_i} = \sigma_{ELPL_i} - \sigma_E \frac{M_i}{M_{ref}} \quad (2)$$

$$\sigma_{req_i} = \frac{1}{\sqrt{2}} \left[ \left( \sigma_{r_{x_i}} - \sigma_{r_{y_i}} \right)^2 + \left( \sigma_{r_{y_i}} - \sigma_{r_{z_i}} \right)^2 + \left( \sigma_{r_{z_i}} - \sigma_{r_{x_i}} \right)^2 + 6 \left( \tau_{r_{xy_i}}^2 + \tau_{r_{yz_i}}^2 + \tau_{r_{zx_i}}^2 \right) \right]^{\frac{1}{2}} \quad (7)$$

Another advantage of the simplified technique introduced by Abdalla et. al. [19] is its capability of predicting the mode of failure upon exceeding the elastic SD limit without conducting lengthy elastic-plastic cyclic loading. The method exhibits investigation of the time increment (i) for which the residual stress field has exceeded the yield stress and checks for the same increment (i) in the elastic-plastic analysis for the same node. If the corresponding stress is equal to yield stress, this case implies reversed plasticity occurrence, but if the corresponding stress is less than the yield stress and any other element in the structure has reached the yield, this implies ratcheting occurrence. The simplified technique was further extended and utilized to generate the elastic SD boundary of different structures [27-33]

Every single point in the Bree diagram is obtained using the two FE runs: Elastic analysis and Elastic-Plastic (ELPL) analysis and then the simplified technique

is utilized to obtain the SD limit load. The Limit loads as obtained using the Twice-Elastic-Slope (TES) method adopted in Section VIII Div. II of the ASME Boiler and Pressure Vessel Code [13] are imposed on the diagram. The elastic limit moment can be obtained also as a complementary parameter from the elastic-plastic analysis (representing loading). The code developed by Abdalla et al. [19] searches for the loading increment that corresponds to equivalent stress that equals or slightly exceeds the material yield stress. The internal pressure is normalized with respect to the internal pressure to initiate yielding of a straight pipe, given by Eq. (8) while the moment is normalized with respect to the fully-plastic moment of a straight pipe given by Eq. (9). The pressure to initiate yielding of a straight pipe having the same material and geometrical configurations of the pipe bend investigated in the current work is calculated to be 43.2 MPa while the plastic moment is calculated to be 12.5 kN.m.

$$M_P = \sigma_Y D_m^2 t \quad (8)$$

$$P_Y = \frac{2\sigma_Y t}{D_m} \quad (9)$$

## 2.6 Proposed procedure for FAD generation

### 2.6.1 Failure Assessment Diagram generation

Failure Assessment Diagrams are obtained for each loading case contained in the corresponding Bree diagram of each crack configuration that was previously defined. The API 579 procedure for generating the FAD did not address the problem of SD and is adopted for structures with crack-like flaws under static loading only. The Toughness ratio ( $K_r$ ) used in the API code is representative of the tendency of the

structure to fail by brittle fracture and is obtained by dividing the fracture mechanics parameter (SIF) obtained analytically or numerically by the material fracture toughness ( $K_{Ic}$ ) determined from standard fracture toughness testing. Load ratio ( $L_r$ ) is representative of the tendency of the structure to fail by plastic collapse and is obtained by dividing analytically or numerically obtained reference stress over the yield strength of the material.

The Failure Assessment Diagram (FAD) proposed in the current work is generated using a different procedure. The FAD ordinate ( $K_r$ ) is the normalized J-integral as given by Eq. 10 representing the toughness ratio. The abscissa is the load ratio ( $L_r$ ) which is the normalized moment obtained by dividing the applied moment by the SD limit moment as given by Eq. 11. The generation procedure of the FAD adopted in this study resembles the R6 procedure option 3 [45], However, the load ratio ( $L_r$ ) utilized in the current work is obtained by normalizing the applied bending moment by the SD moment obtained by the simplified technique [19]. The Load ratio is selected in order to link the SD limit load with the fracture mechanics parameter in one assessment diagram aiming to provide a safe region against both SD failure and unstable crack growth.

$$K_r = \sqrt{\frac{J_{ELA}}{J_{ELA} + J_{PLA}}} \quad (10)$$

$$L_r = \frac{M}{M_{SD}} \quad (11)$$

The elastic J-integral can be given with respect to the SIF as shown in Eq. 12 while the total J-integral given in Eq. 13.

$$J_{ELA} = K^2 \left( \frac{1-\nu^2}{E} \right) \quad (12)$$

$$J = J_{ELA} + J_{PLA} \quad (13)$$

Plastic J-integral can be calculated using the contour integrals method or by adopting the Line Spring Model as used in this study. A cut off ratio is defined to distinguish between the failures that are derived by exceeding the SD limit or by unstable crack growth. The Failure Assessment Line (FAL) that separates the safe region from the region of failure is obtained using Eq. 14. The procedure adopted to generate the FAD of the various models under consideration of the current work is shown in Fig. 27.

$$K_r = f(L_r) \quad (14)$$

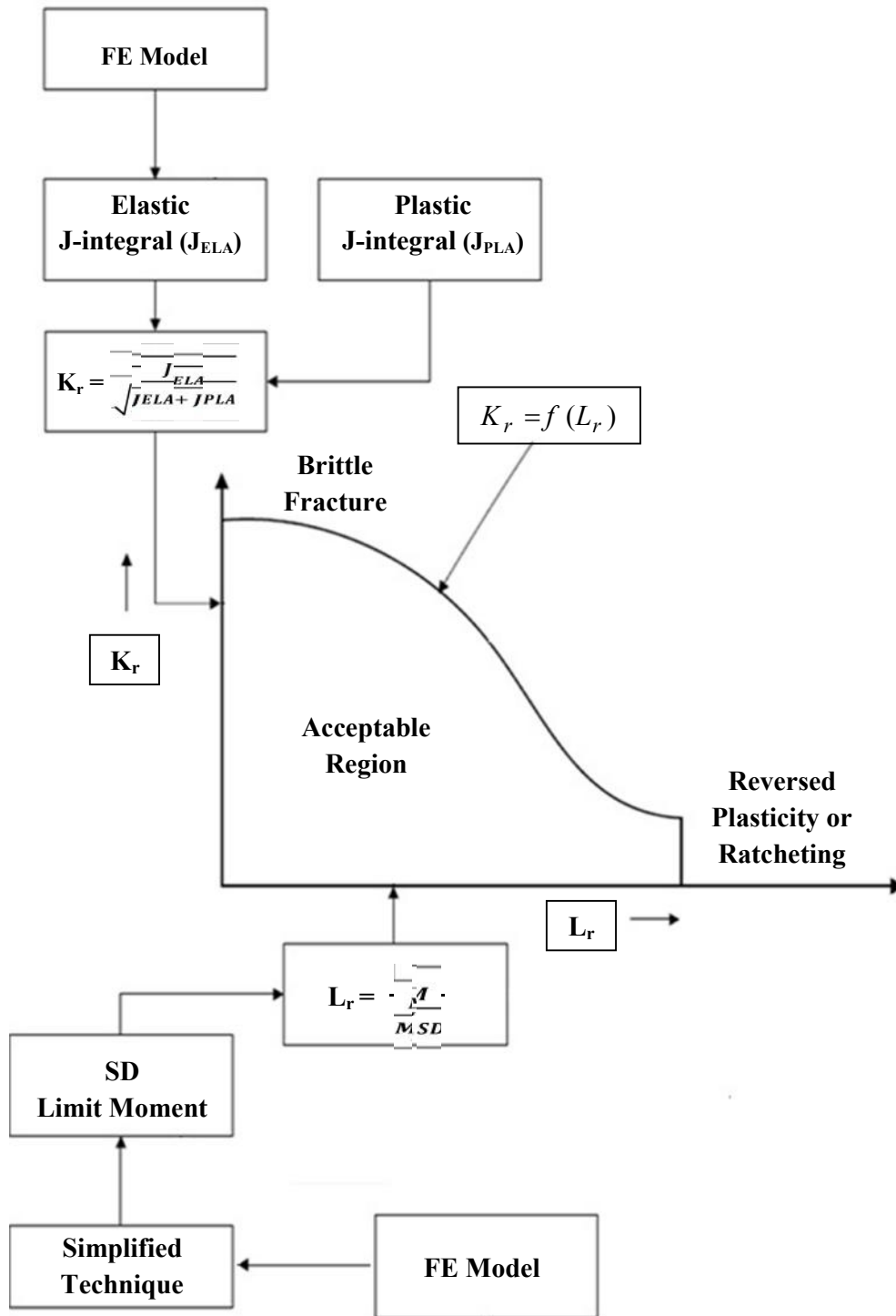


Fig. 27 Failure Assessment Diagram generation procedure

## 2.6.2 Assessment procedure

The assessment point is defined using the toughness and load ratios as given by Eq. 15 and Eq. 16, respectively, and then plotted in the FAD. If the assessment point falls within the acceptance region then the structure is said to be safe against brittle fracture and reversed plasticity or ratcheting; on the other hand, if the assessment point falls beyond the acceptance region the structure would fail by brittle fracture (unstable crack growth) or one of the possible failures due to exceedance of the SD limit load, namely, reversed plasticity or ratchetting based on the position of the assessment point on the corresponding Bree diagram.

$$K_r = \sqrt{\frac{J_{ELA}}{J_{lc}}} \quad (15)$$

$$L_r = \frac{M}{M_{SD}} \quad (16)$$

In order to account for the possibility of stable crack growth if the pipe bend is inside the elastic SD region of the Bree diagram and also inside the safe region of the FAD, the crack growth formula of Paris that is adopted in the ASME FFS-1 API-1 [16] is utilized (Eq. 17).

$$\frac{da}{dN} = C (\Delta K)^n \quad (17)$$

The Paris law constants ( $C$  and  $n$ ) are obtained from the standards according to the material and operating conditions. It should be noted that Paris law does not account for the effective SIF because the possibility of having crack opening at the first half of

the cycle and crack closure at the second half of the cycle. The Stress Intensity Factor (SIF) is obtained from the output of the LSE. The crack growth rate is calculated per cycle and the new crack size after the expected number of cycles is introduced to the defect free model using the LSE. A detailed crack growth case study is presented in Sec. 3.3.5.

A summary of the procedure adopted in the current work to generate the FAD and the assessment of the integrity of cracked pipe bends is given hereafter and is also shown in Fig. 28 :

1. The crack geometry is defined and introduced to the defect free FE models of the pipe bend using LSE as previously presented in Sec. 2.
2. The simplified technique is applied using the Elastic and ELPL analyses and then the SD limit moment is obtained as previously presented in Sec. 2.5.
3. The elastic and total J-integrals are obtained from the output of the LSE and are used to plot the FAD. Typical J-integral curves are shown in Fig. 29 and Fig. 30
4. The assessment point is plotted on the FAD using the obtained SD limit load, Elastic J-integral, and the material fracture toughness.
5. The pipe bends are considered to be safe against both exceeding SD limit load or unstable crack growth according to the position of the assessment point
6. Crack growth analysis is adopted if the pipe bend is safe against unstable crack growth.

The aforementioned procedure is further elaborated in Fig. 31 and also a typical FAD is shown in Fig. 32 where the limits of LEFM and EPFM and also the elastic and plastic components of J-integral are shown in the diagram.

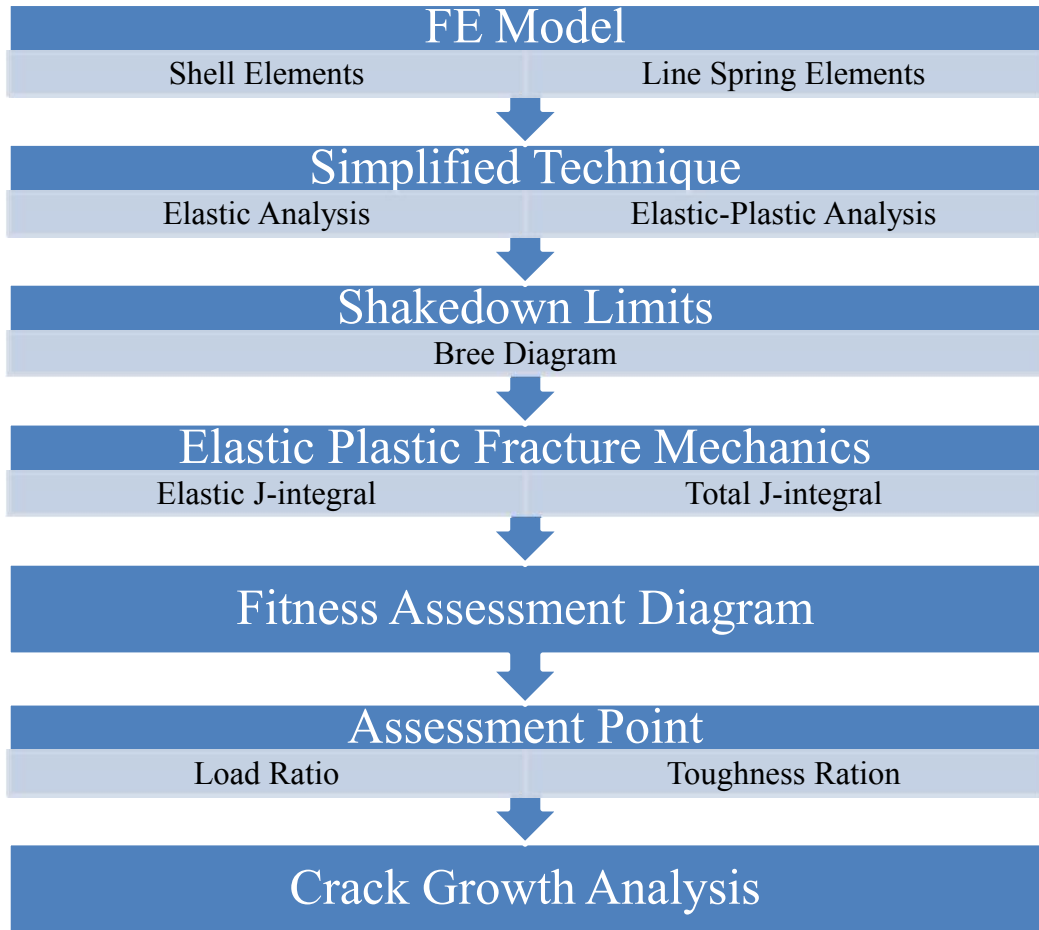


Fig. 28 Assessment procedure

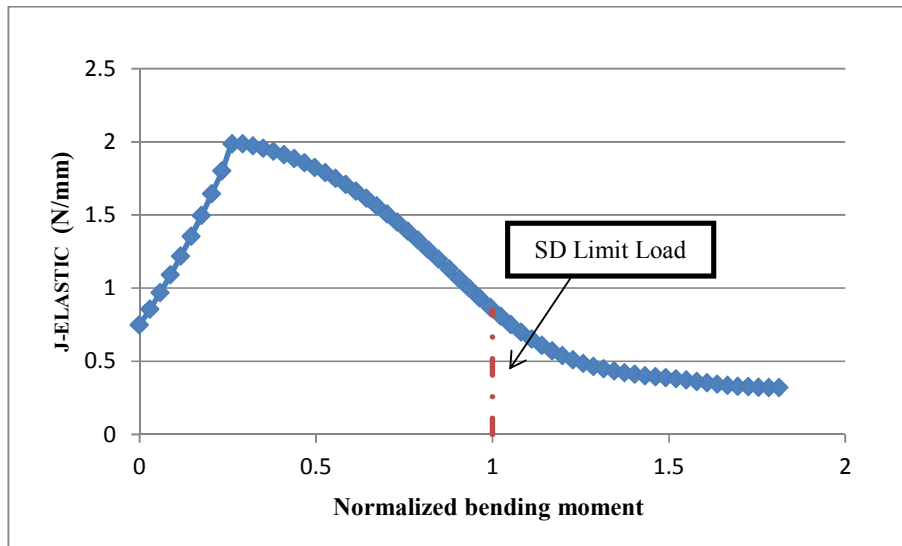
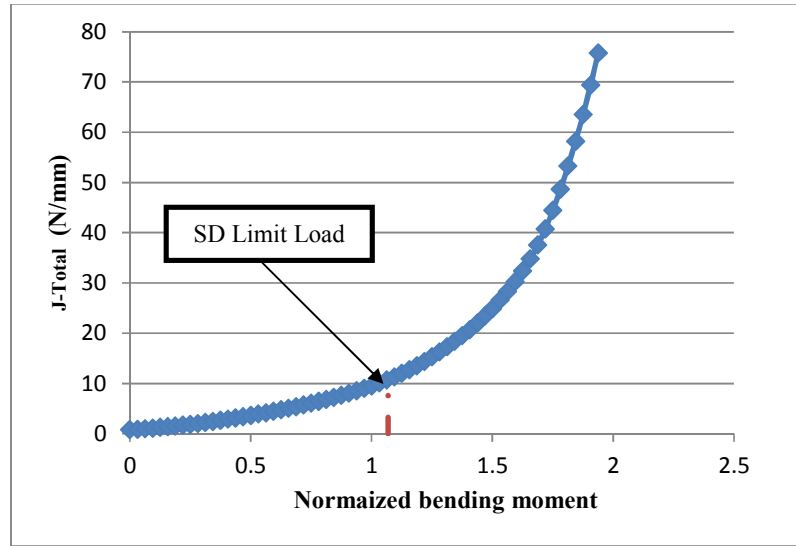


Fig. 29 Elastic J-integral Vs. Applied Moment for the case of QM120C-IPO at

15%  $P_y$



**Fig. 30 Total J-integral Vs. Applied Moment for the case of QM120C-IPO at 15%  $P_y$**

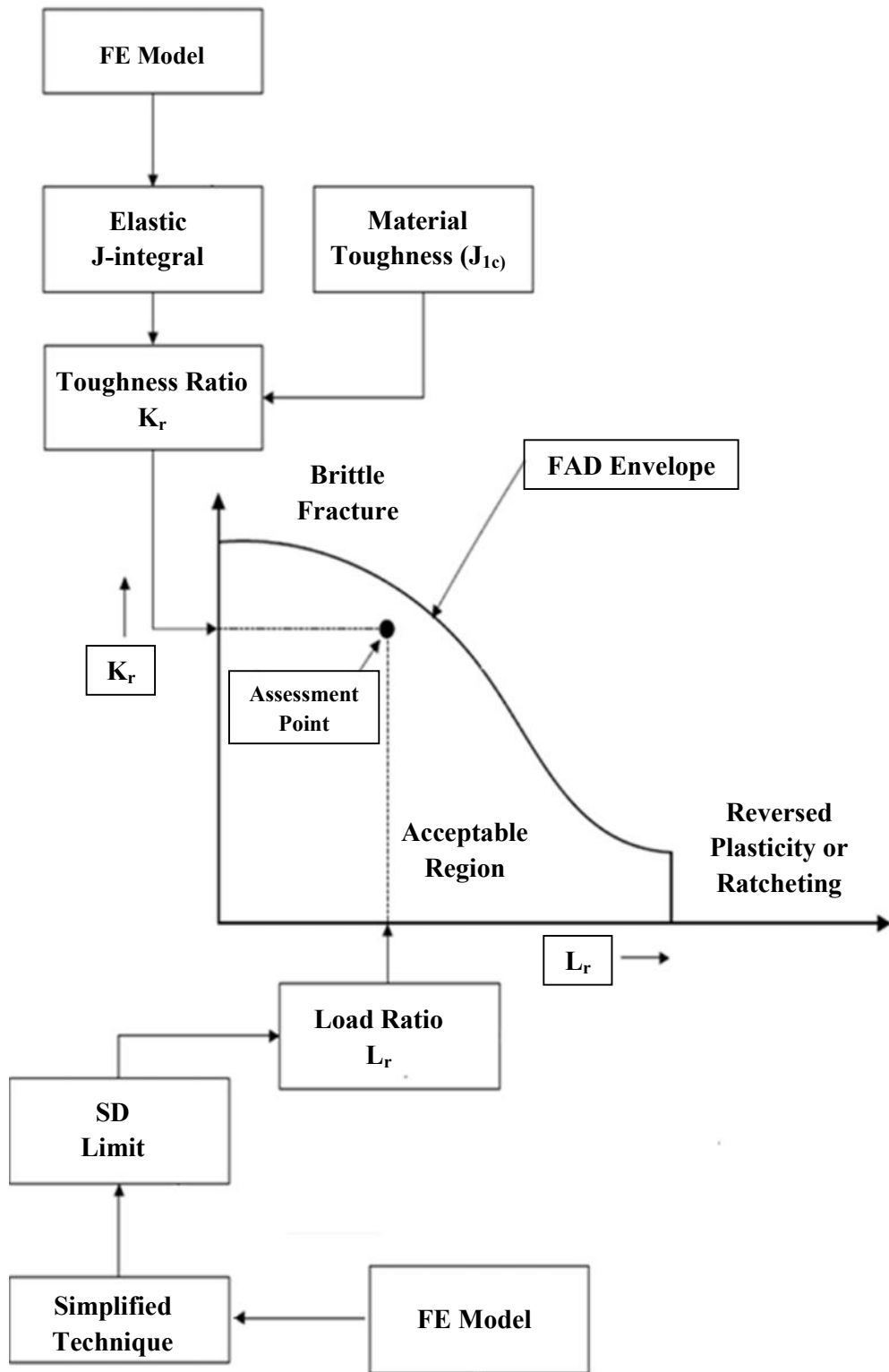
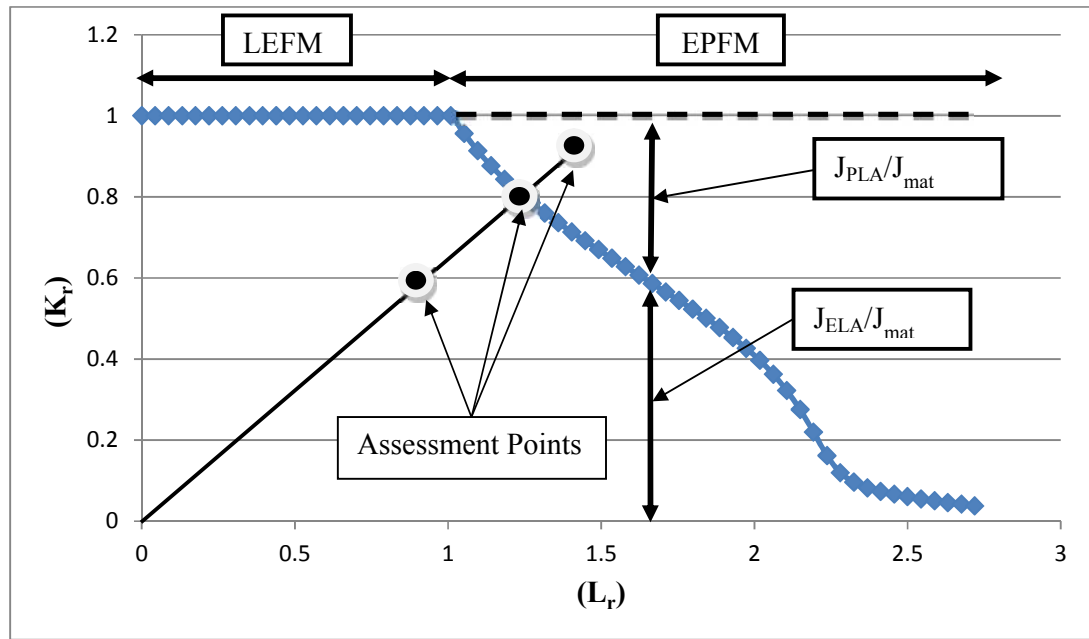


Fig. 31 Assessment criteria



**Fig. 32 Integrity assessment procedure of cracked pipe bends**

The proposed procedure for the assessment of integrity of cracked pipe bends is applied to different models with different crack configurations as summarized in table.7.

**Table 7 Summary of the models investigated**

#	Moment Direction Opening/Closing	Crack Characteristics		
		Location (intrados/ extrados)	Angular Circumferential length (degrees)	Depth b/t
1	Opening	Defect free		
2	Opening	Intrados	45	0.5
3	Opening	Intrados	120	0.5
4	Opening	Intrados	120	0.75
5	Closing	Defect free		
6	Closing	Extrados	120	0.5
7	Closing	Extrados	120	0.75

## CHAPTER 3

### RESULTS and DISCUSSION

#### 3.1 Bree diagrams

##### 3.1.1 Pipe bends under IPO bending moment and internal pressure

###### 3.1.1.1 Defect-Free model

The shakedown boundary as well as the plastic collapse limit (limit load) of the defect free pipe bends is presented based on the simplified technique developed by Abdalla et. al. [19] and the TES method adopted by the ASME code [11], respectively. A sample moment end-rotation curve that is used to obtain the limit load using TES method is shown in Fig. 33. The Bree Diagram having the Elastic limit, SD boundary, and the Limit load of the defect free model is shown in Fig. 34.

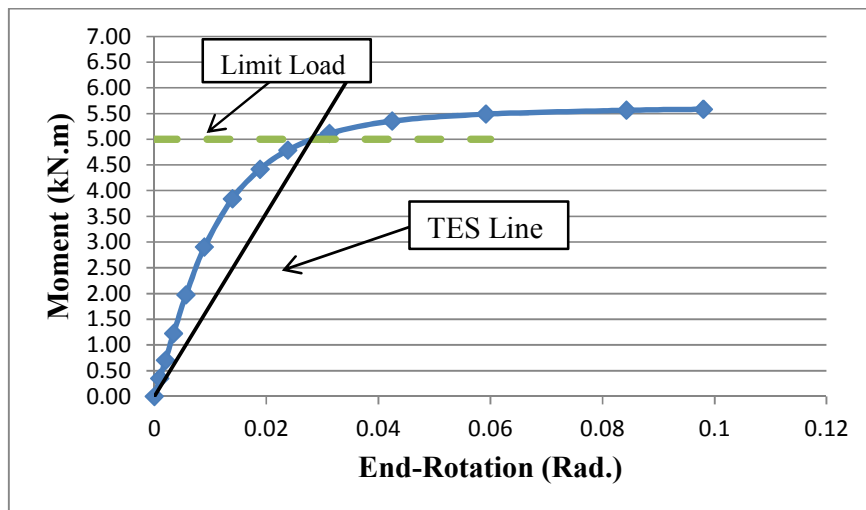
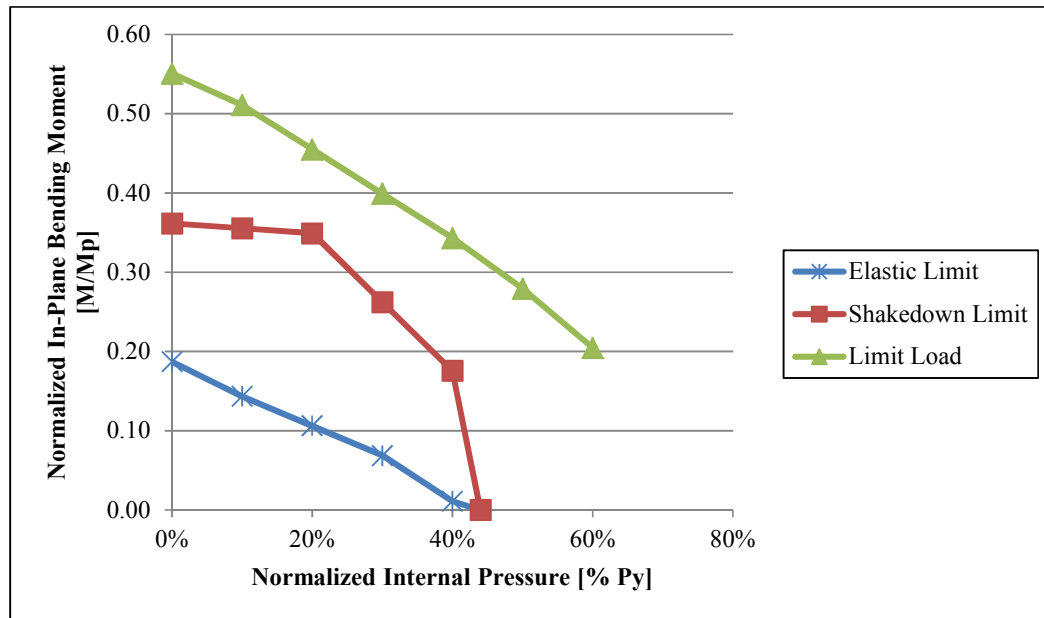


Fig. 33 Representative sample Moment End-Rotation curve for the Defect-Free model at 30%  $P_y$  used for limit load Determination using TES method.



**Fig. 34 Normalized limit, shakedown and elastic moments of the defect-free pipe bend subjected to IPO bending moment and internal pressure**

### 3.1.1.2 Pipe bend with 45° circumferential crack

The LSE is utilized to introduce part through crack of depth to thickness ratio (b/t) of 0.5 and subtended angle of 45° along the pipe bend intrados. The TES slope method is utilized to obtain the limit load while the simplified technique is used to obtain the Elastic limit and SD limit. The Bree diagram of the model that represents cases of short cracks is shown in Fig. 35.

It is worth mentioning that all the obtained Elastic, SD, and limit loads are obtained from the output stresses of the nodes because the cracked models contained two different types of elements; shell elements (S8R) and LSE. The code written by Abdalla et. al. [15] to calculate the SD limit is modified to read the stresses from the nodes not from the Integration points. The code calculates the equivalent residual stress for all the nodes in the structure and compares it to the yield strength of the material as per Melan's Theorem [7-8]. The nodes that are common between the shell

and LSE elements were expected to have the most critical stresses which is confirmed by the output of the simplified technique. The most critical node for all the cracked models was located at the crack tip- free surface intersection.

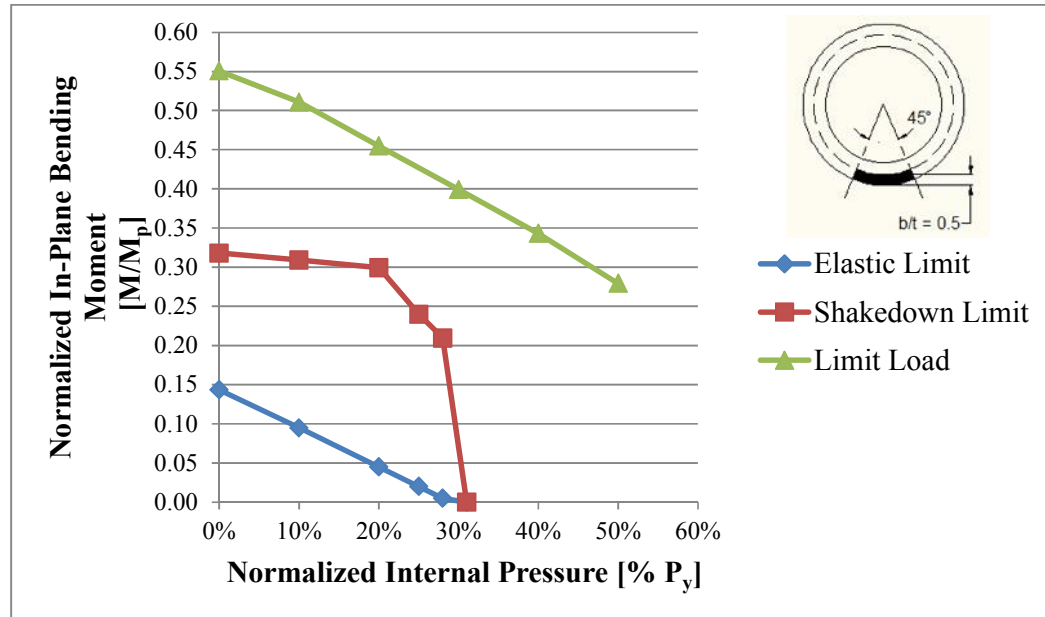


**Fig. 35 Normalized limit, shakedown and elastic moments of the pipe bend with 45° circumferential crack (b/t =0.5) subjected to IPO bending moment and internal pressure**

### 3.1.1.3 Pipe bend with 120° circumferential crack

The Bree diagram of the pipe bend with external 120° circumferential crack (b/t =0.5) in the intrados subjected to the combined effect of internal pressure and IPO bending moment generated using the simplified technique is shown in Fig. 36. The Bree diagram of the same model but with deeper crack (b/t=0.75) is shown in Fig. 37. The elastic limits (the load that initiates yielding at any point in the pipe bend) and the limit load determined using TES method are also superimposed on the Bree diagram.

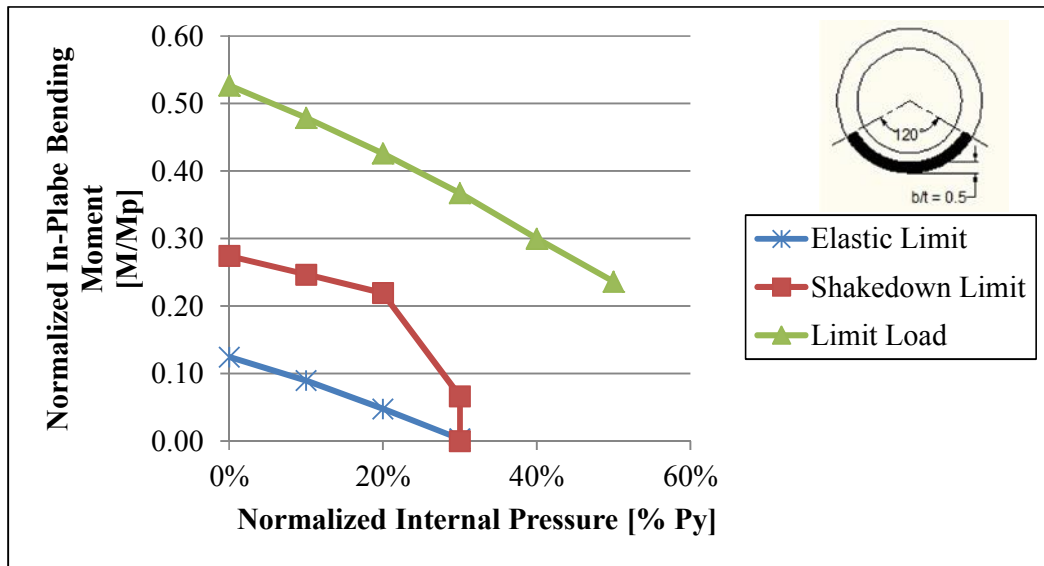


**Fig. 36** Normalized limit, shakedown and elastic moments of pipe bend with 120° circumferential crack (b/t=0.5) subjected to IPO bending moment and internal pressure

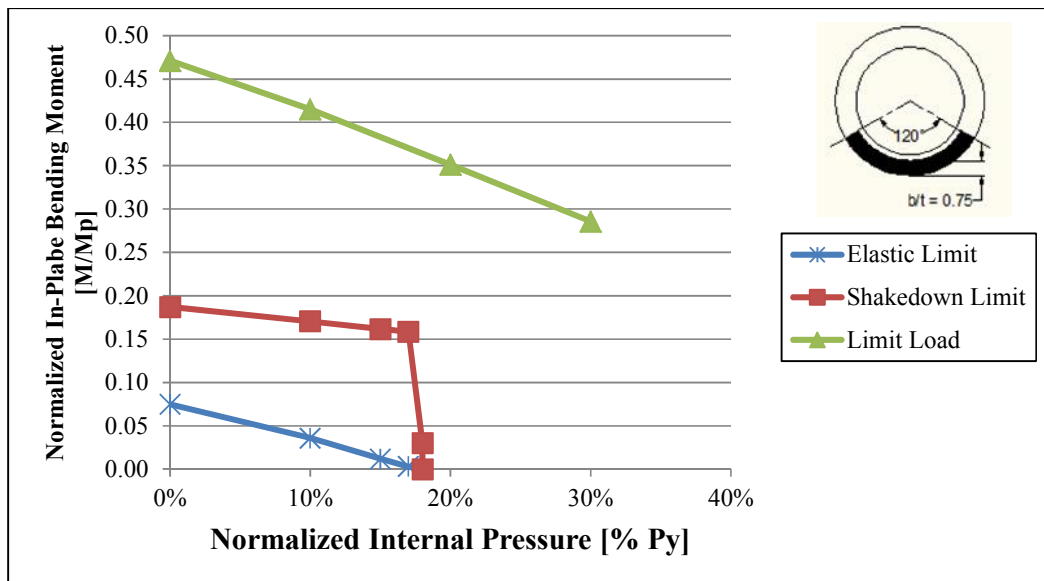


**Fig. 37** Normalized limit, shakedown and elastic moments of pipe bend with 120° circumferential crack (b/t=0.75) subjected to IPO bending moment and internal pressure

### 3.1.1.4 Effect of crack size on SD boundary

The effect of increasing the crack length on the SD limit is shown in Fig. 38. The SD limits of the defect-free (DF) pipe bend subjected to the combined effect of internal pressure and In-Plane bending moment is compared to the SD limits of the pipe bend with 45° circumferential crack in the intrados (QM45C-IPO) and also with a pipe bend with 120° circumferential crack in the intrados (QM120C-IPO) having the same crack depth ( $b/t=0.5$ ). It can be observed that the 45° crack has little influence on both the elastic limit and SD limit loads while the 120° crack has a major influence on both the elastic and SD limit loads. The same effect was noticed for the limit load where it can be seen from the aforementioned limit load verification study that limit load was not considerably reduced except for long cracks.

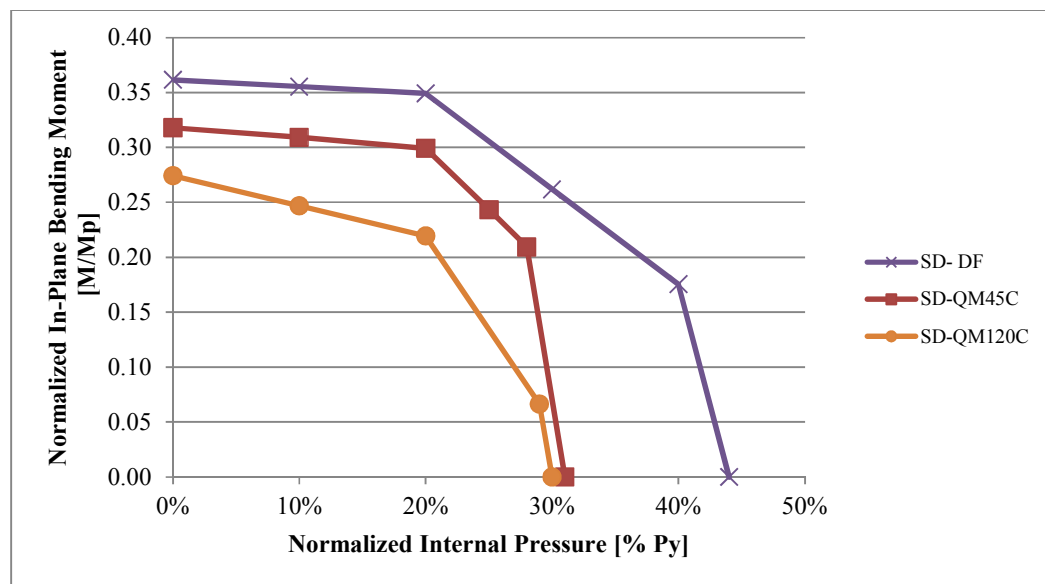


**Fig. 38 Comparison between SD limits of Defect-Free-IPO, QM45C-IPO, and QM120C-IPO Models ( $b/t=0.5$ )**

### 3.1.1.5 Effect of crack depth on SD boundary

The effect of increasing the crack depth on the SD limit is shown in Fig. 39. The SD limits of the defect-free pipe bend subjected to the combined effect of internal pressure and IPO bending moment is compared to the SD limits of the pipe bend with 120° circumferential crack at the intrados (QM120C-IPO) and also with the same model, but with deeper crack ( $b/t=0.5$ ). It can be observed that increasing the crack depth erodes the safe SD boundary.

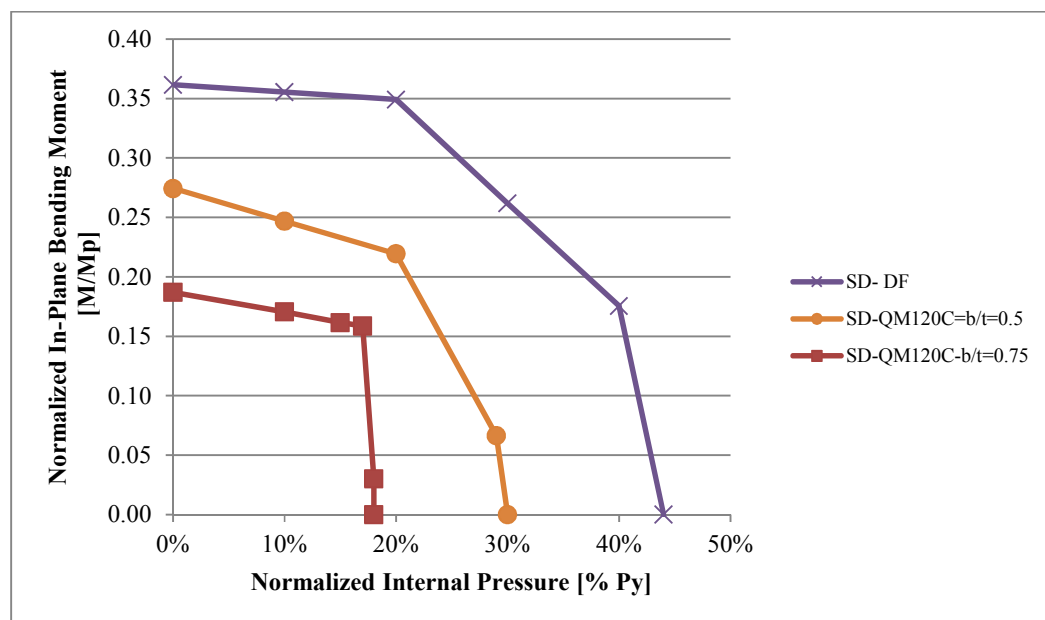


**Fig. 39 Comparison between SD limits of Defect-Free-IPO, QM120C-IPO ( $b/t=0.5$ ), and QM120C-IPO ( $b/t=0.75$ ) Models**

### 3.1.2 Pipe bends under IPC bending moment and internal pressure

#### 3.1.2.1 Defect-Free model

The SD boundary as well as the plastic collapse region and the elastic limits of the defect free model subjected to the combined effect of internal pressure and IPC bending moment is shown in Fig. 40. It can be observed that the elastic limit curve is slightly increasing at low pressures and then it starts to decrease by increasing the

applied pressure as shown in Fig. 40. The same phenomenon can be noticed in the limit load curve and this can be attributed to the strengthening effect caused by the applied pressure because the internal pressure induces pipe bend end rotation in the opposite direction of the end rotation that caused by IPC bending moment.

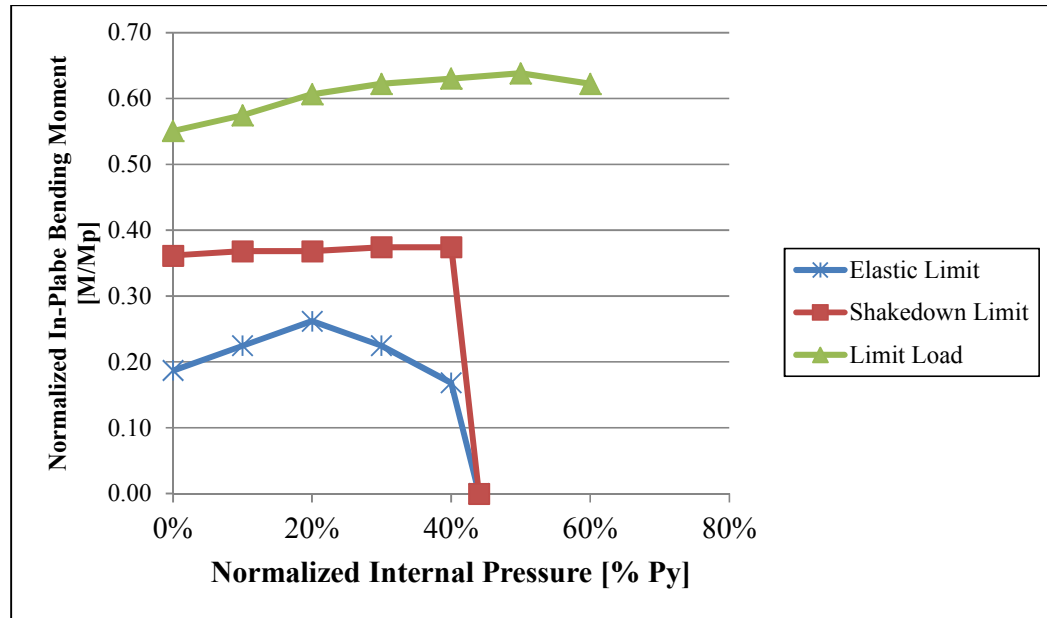


**Fig. 40 Normalized limit, shakedown and elastic moments of the defect-free pipe bend subjected to IPC bending moment and internal pressure**

### 3.1.2.2 Pipe bend with 120° circumferential crack

Bree diagram of the pipe bend with external 120° circumferential crack at the extrados subjected to the combined effect of internal pressure and IPC bending moment generated using the simplified technique. Two crack depth to thickness ratios have been investigated, namely,  $b/t = 0.5$  as shown in Fig. 41 and  $0.75$  as shown in Fig. 42. The elastic limits and limit loads are also superimposed on the diagram. It can be observed that the elastic limit of the first case ( $b/t = 0.5$ ) has an approximate plateau level which is slightly increasing, however the case of deep crack ( $b/t = 0.75$ ) has a clear plateau at low pressures (up to  $30\% P_y$ ) and then it starts to decrease by

increasing the applied pressure. The observed plateau can be attributed to the effect of strengthening effect caused by the applied pressure which is counteracted by the weakening effect caused by the crack while the defect free model has only the strengthening effect.

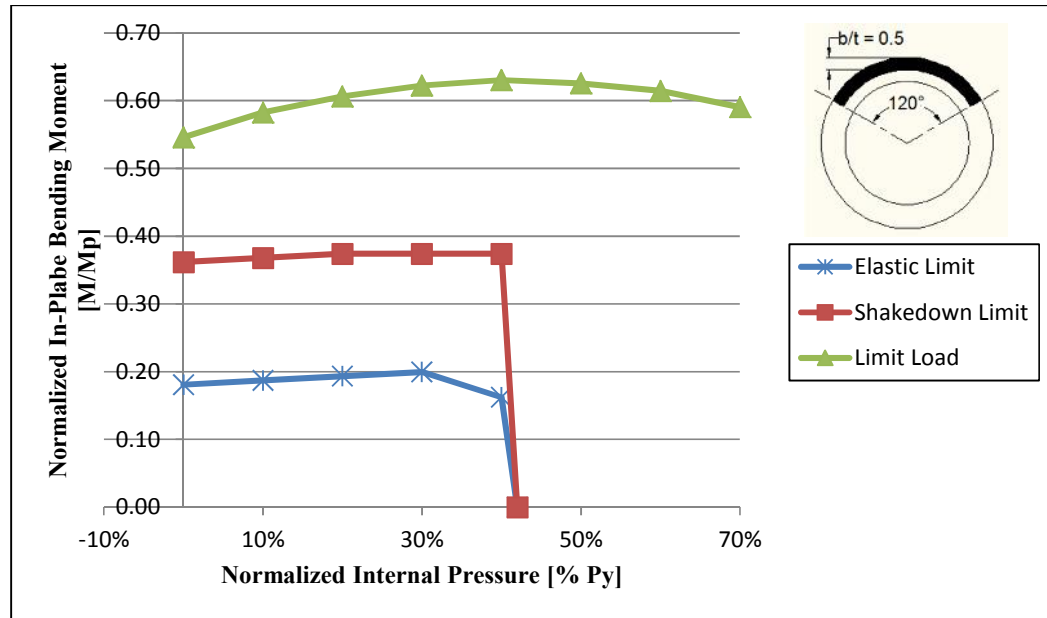


**Fig. 41 Normalized limit, SD, and elastic moments of QM120C (b/t =0.5) subjected to IPC bending moment and internal Pressure**

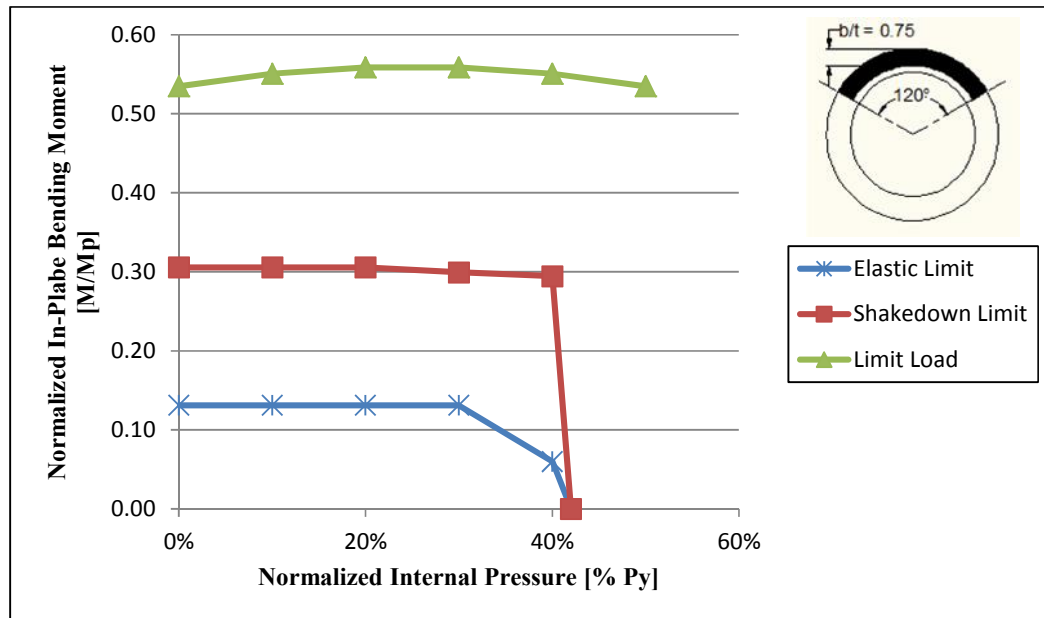


**Fig. 42 Normalized limit, SD, and elastic moments of QM120C ( $b/t=0.75$ ) subjected to IPC bending moment and internal pressure**

### 3.1.2.3 Effect of crack size on SD boundary

A comparison between the DF model subjected to the same loads and the QM120C-IPC model is shown in Fig. 43. It can be shown that the pipe bend has tolerated a long ( $120^\circ$ ) and deep ( $b/t=0.75$ ) crack because of the loading conditions that provides strengthening of the pipe bend under IPC. It can be seen that there is a slight reduction in the elastic and SD limits compared to the DF model under the same loading conditions. The models with shorter cracks ( $45^\circ$ ) and also the models with more shallow cracks ( $b/t=0.5$ ) were found to have a minor effect on the SD boundary due to the presence of cracks on the extrados under IPC.

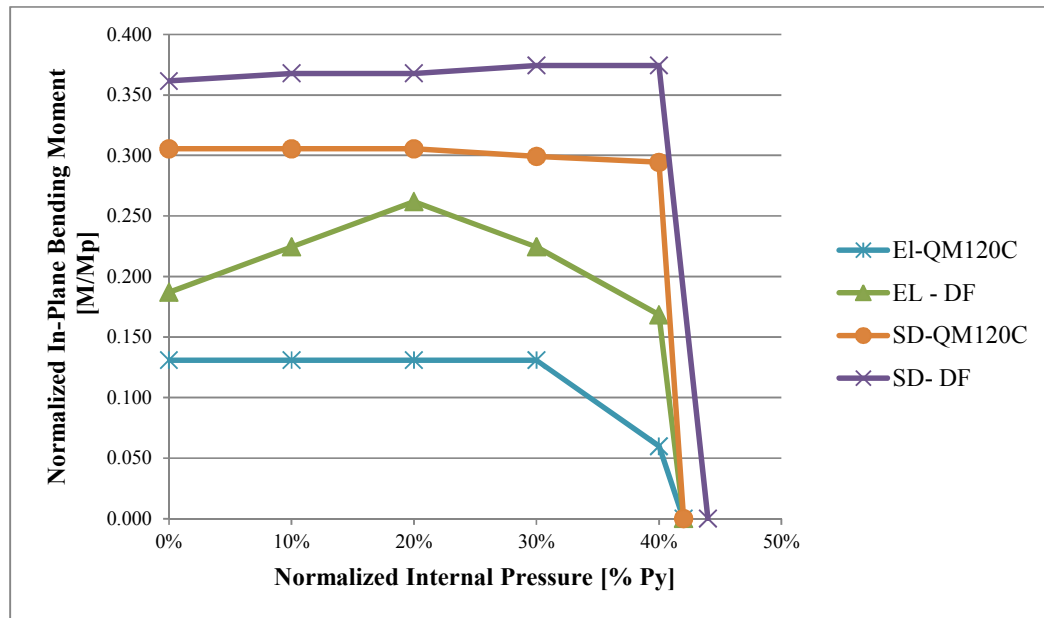


**Fig. 43 Comparison between Elastic and SD limits of Defect-Free and QM120C (b/t =0.75) models subjected to IPC bending moment and internal pressure**

### 3.1.3 Comparison between IPO and IPC bending moments

Comparisons between the two different bending moments adopted in this study are shown in Fig. 45, Fig. 46, and Fig. 46, in order to show the criticality of both loads on the Elastic and SD limits. It should be noted that the cracks are located at different positions to cause crack opening under loading. Crack are located at the intrados for IPO and at the extrados for IPC. However, both intrados and extrados cracks are located at the tension side. It can be observed from the comparisons that the IPO bending moment is more critical than IPC as it results in a dramatic reduction in the SD limits with respect to the DF model. This phenomenon is observed for both the Defect-Free model (Fig. 46) and also the models with different crack depth to thickness ratios as can be observed in Fig. 45 and Fig. 46.

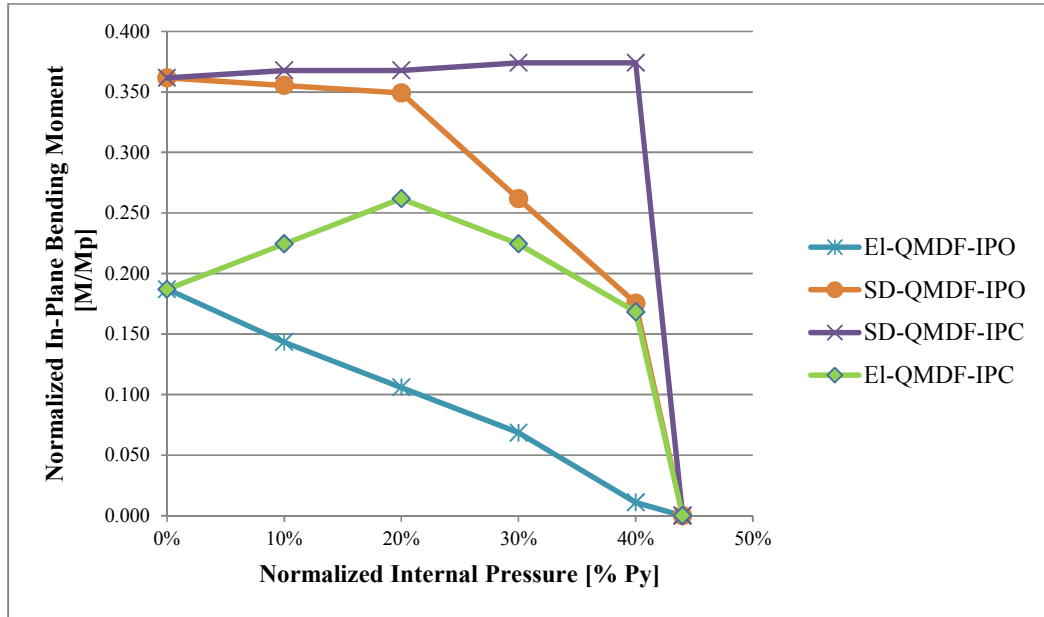


Fig. 44 Comparison between Elastic and SD limits of Defect-Free models under IPO and IPC bending moments ( $b/t=0.75$ )

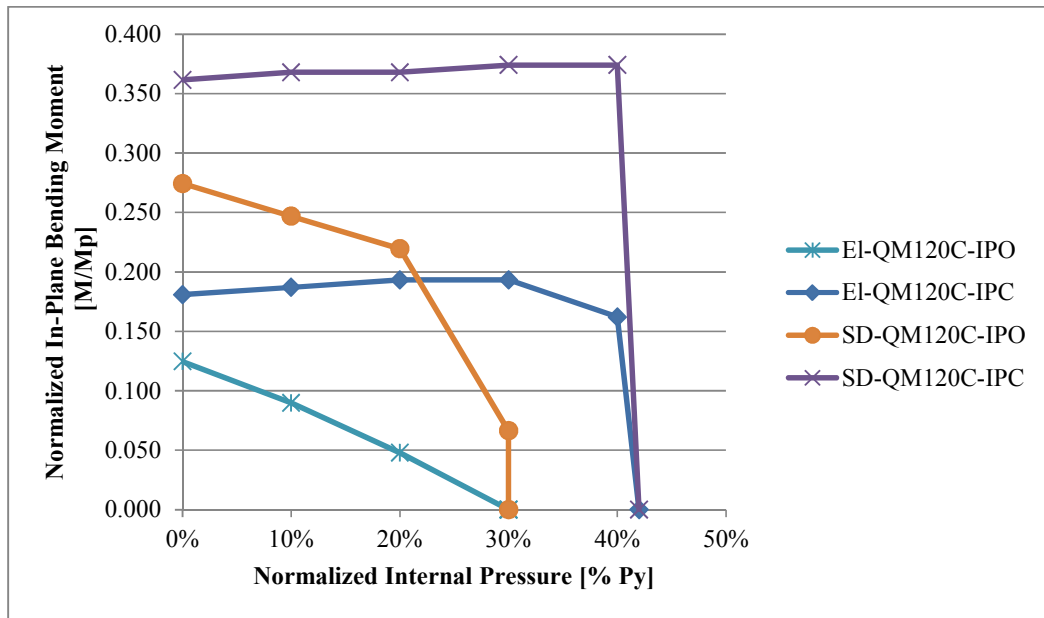
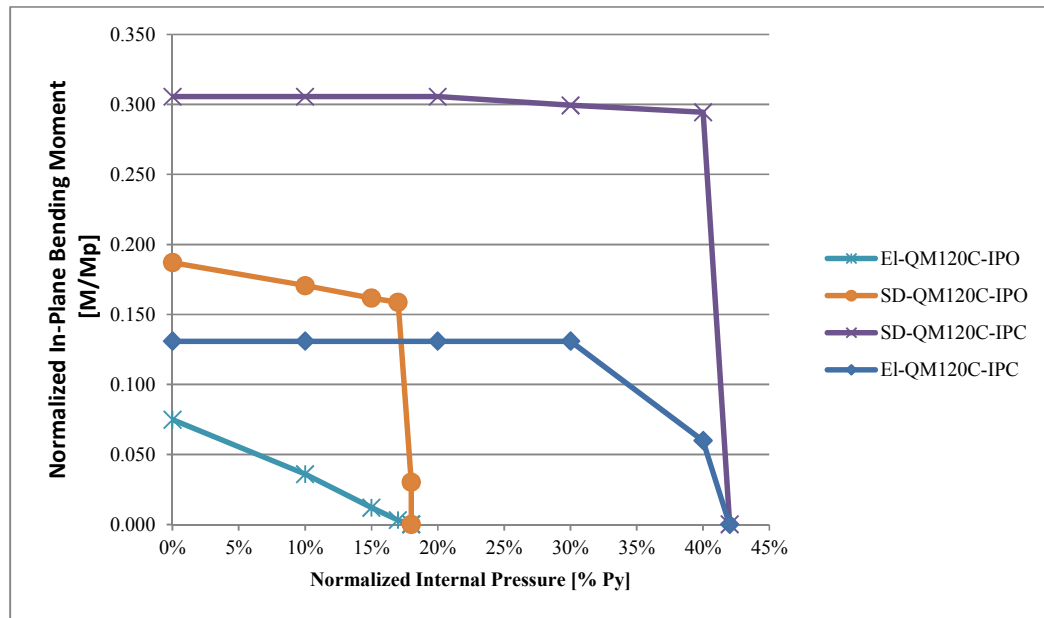


Fig. 45 Comparison between Elastic and SD limits of QM120C-IPO, and QM120C-IPC ( $b/t=0.5$ )



**Fig. 46 Comparison between Elastic and SD limits of QM120C-IPO, and QM120C-IPC (b/t=0.75)**

### 3.2 Validation of the simplified technique using full cyclic loading

In order to gain confidence on the predicted SD limits obtained by the simplified technique, some loading conditions entailed in the aforementioned Bree diagrams from all the models were selected to undergo full Elastic-Plastic (ELPL) cyclic loading FE analyses. The critical point in all the models was the crack tip at the outer surface of the pipe bend. The Equivalent Plastic Strain (PEEQ), the Von Mises equivalent stress and the mean stress are requested at the node that coincides with the critical point. The mean stress which is a measure of the compression (hydrostatic) effect on the node is used to monitor the change from tensile to compressive equivalent stress because the Von Mises equivalent stress is always positive, hence when the mean stress is positive then the Mises stress sign is changed to negative and vice versa.

The output of the simplified technique was used as input for FE ELPL cyclic loading in order to observe the elastic shakedown phenomenon which is shown in Fig. 47. The reversed plasticity failure predicted by the simplified technique was validated by the full ELPL cyclic loading FE analysis as shown in Fig. 48 while the ratcheting behavior is shown in Fig. 49. The input load was slightly exceeding the SD load obtained by the simplified technique. It can be observed from Fig. 47 and Fig. 48 that equivalent stress exceeded the material yield strength despite using EPP material model which can be attributed to the stress averaging algorithm adopted by the FE code when the stresses are requested at the nodes.

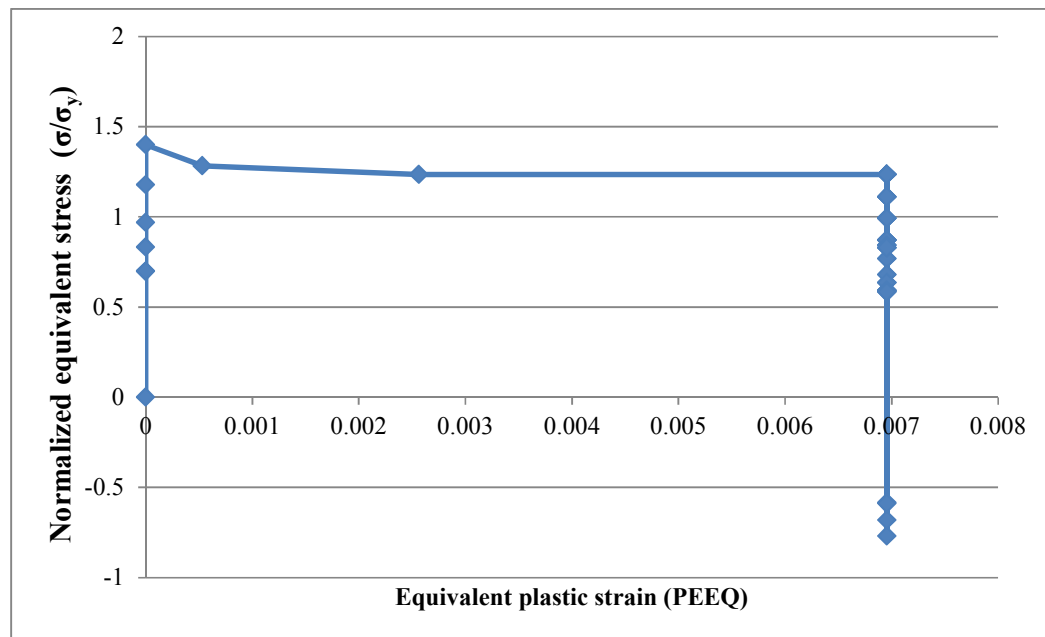


**Fig. 47 Elastic shakedown behavior of the model QM120C-IPO exhibited for the case of 15%  $P_y$  using the shake down limit obtained by the simplified technique.**

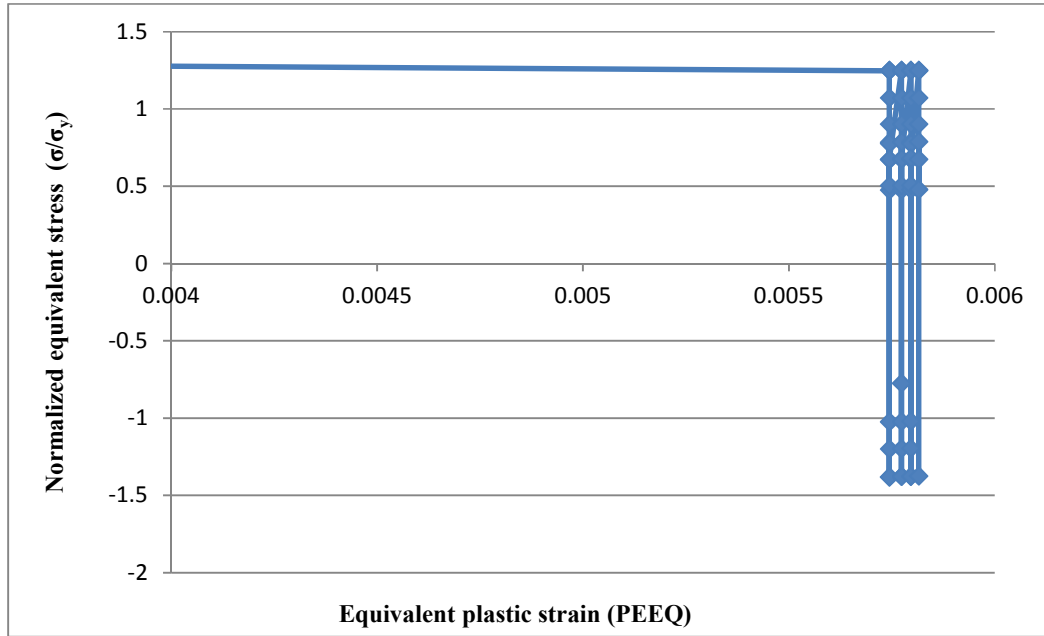


**Fig. 48 Reversed plasticity behavior exhibited for the case of 0%  $P_y$  (QM120C-IPO) upon slightly exceeding the shakedown limit obtained using the simplified technique.**

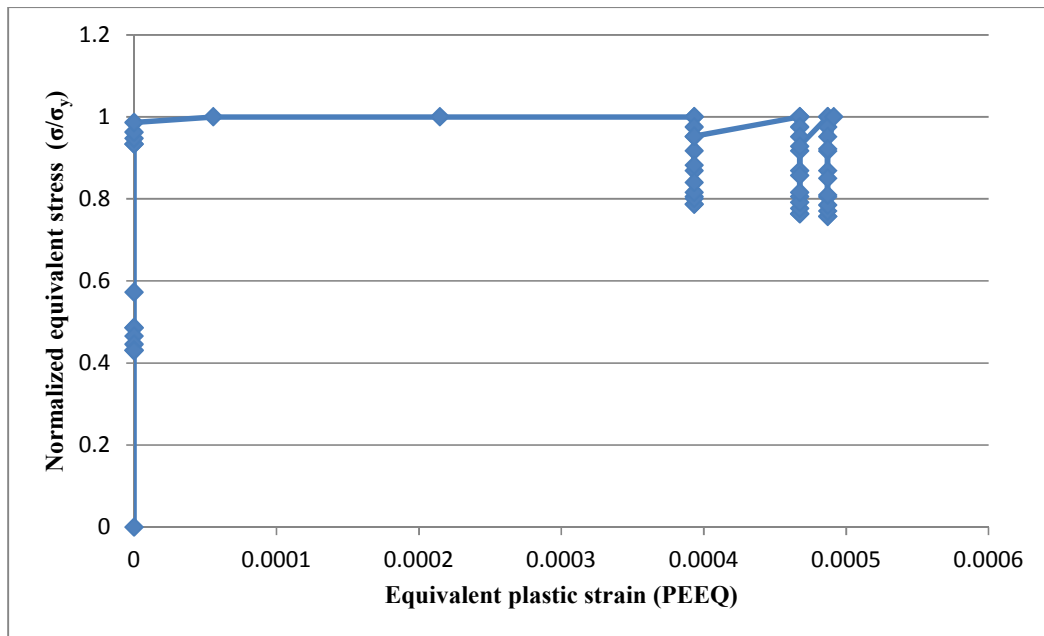


**Fig. 49 Ratchetting behavior exhibited for the case of 40%  $P_y$  Defect-free model upon slightly exceeding the shakedown limit obtained using the simplified technique.**

### **3.3 Failure Assessment Diagrams**

#### **3.3.1 Elastic and total J-integrals**

The API Fitness for Service Code [18] and the R6 procedure [45] addressed the problem of the integrity assessment of cracked structures. The FAD of cracked pipe bends considered in this study are generated using ELPL fracture mechanics analyses utilizing the Line Spring Model. The toughness ratio is obtained by dividing the elastic J-integral by the total J-integral and plotted against the load ratio obtained by dividing the applied moment by the SD limit moment outputted by the simplified technique. A cut-off ratio is defined corresponding to the SD limit load. The elastic J-integral increases with the applied load up to the LEFM limit and then it starts to decrease when the loading induces crack tip stresses in the domain of ELPL fracture mechanics; at this point the plastic part of the total J-integral is dominating.

#### **3.3.2 The effect of crack size and loading condition on J-integrals**

The effect of increasing the applied internal pressure on both the elastic J-integral and the total J-integral is shown in Fig. 50 and Fig. 51 respectively. It is evident that increasing the applied pressure is shifting the curves upwards as expected. The limit for LEFM is reached earlier by increasing the applied internal pressure as can be seen on Fig. 50 where the value of the elastic J-integral starts to decrease after reaching this value. It can be observed from Fig. 50 that at no pressure the elastic J-integral starts from zero while upon introducing the internal pressure the curve is starting from certain value that is increasing by increasing the applied pressure. This can be attributed to the loading scenario adopted in the current work that is based on applying the internal pressure firstly and then the bending moment is applied afterwards.

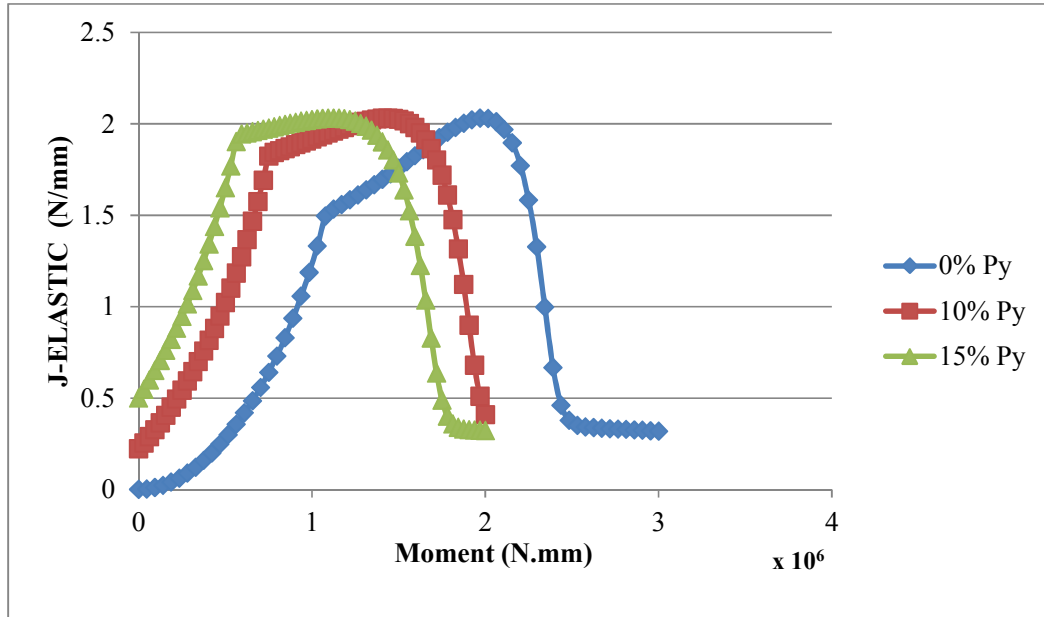


**Fig. 50** The effect of increasing the internal pressure on the elastic J-integral for the model QM120C-IPO ( $b/t=0.75$ )

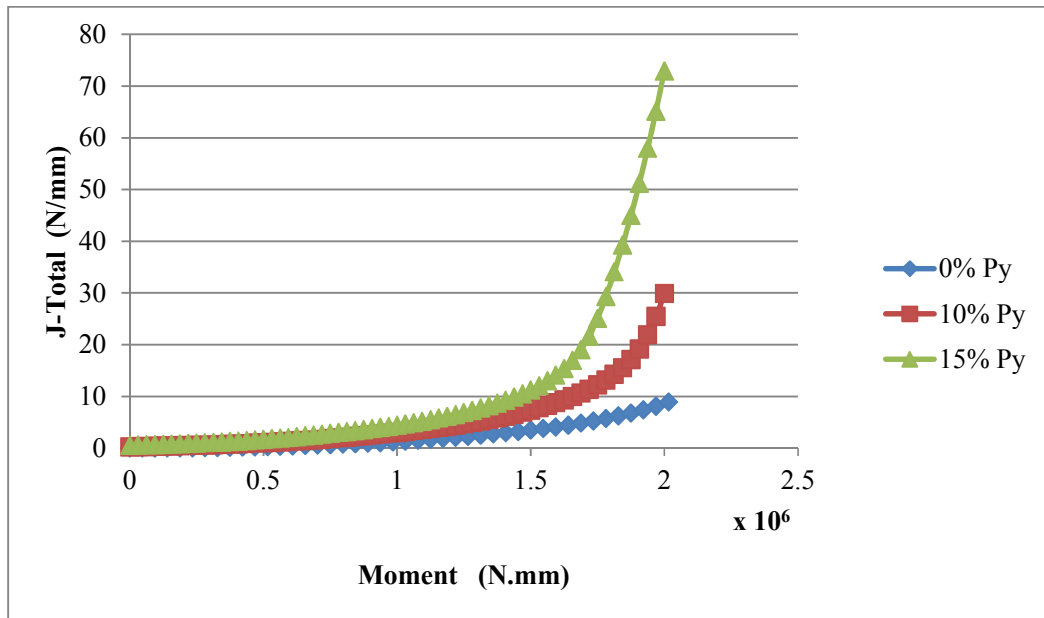


**Fig. 51** The effect of increasing the internal pressure on the total J-integral for the model QM120C-IPO ( $b/t=0.75$ )

The effect of increasing the crack size on both the elastic and total J-integral that will be used to locate the assessment point on the proposed FAD is investigated. The crack size is increased at the same loading conditions in order to investigate the change in the resulted J-integrals. Comparison between the elastic J-integral and also the total J-integral obtained under no internal pressure of the model that had short crack (45°) and the model that had long crack (120°) is shown in Fig. 52 and Fig. 53. The same comparison but under internal pressure together with IPO bending is shown in Fig. 54 and Fig. 55. It can be seen that increasing the crack size is increasing both the elastic and total J-integral for all the aforementioned cases.

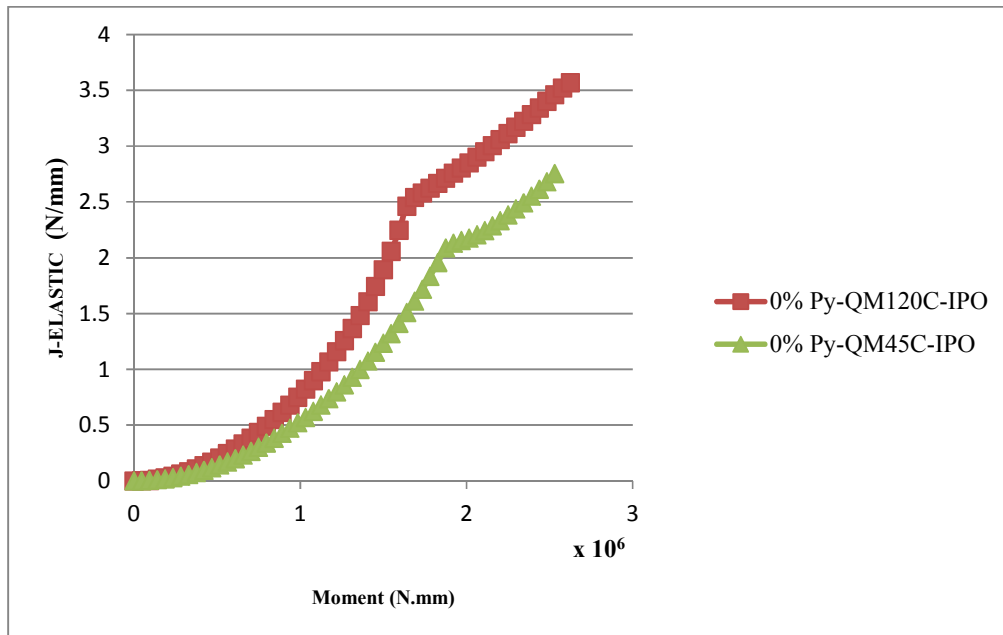


**Fig. 52 Comparison between the elastic J-integral obtained under IPO bending only of the models QM120C and QM45C (b/t=0.5)**

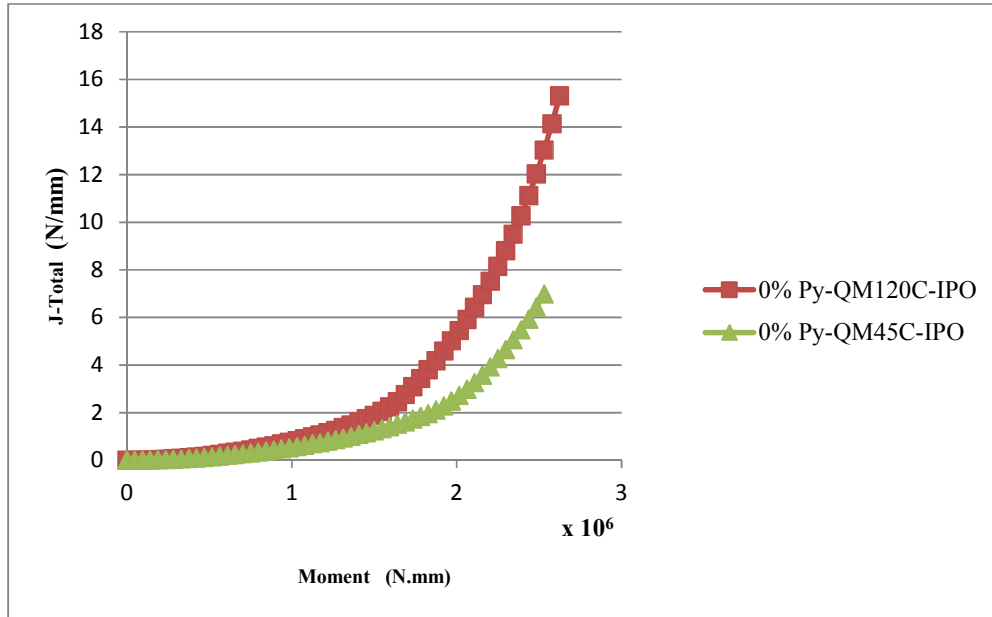


**Fig. 53 Comparison between the total J-integral obtained under IPO bending only of the models QM120C and QM45C (b/t=0.5)**

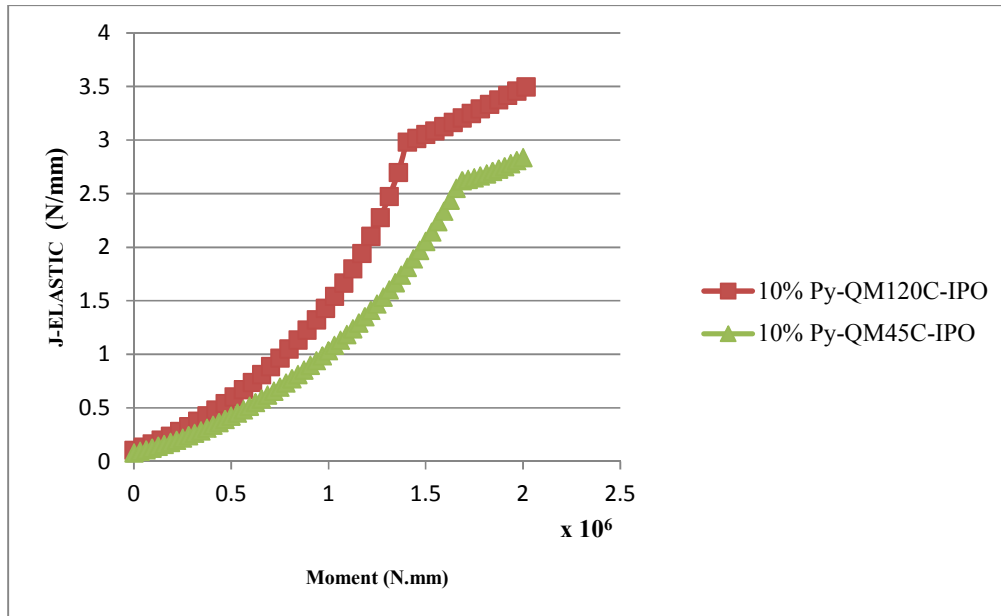


**Fig. 54 Comparison between the elastic J-integral obtained under IPO bending and 10% P<sub>y</sub> of the models QM120C and QM45C (b/t=0.5)**

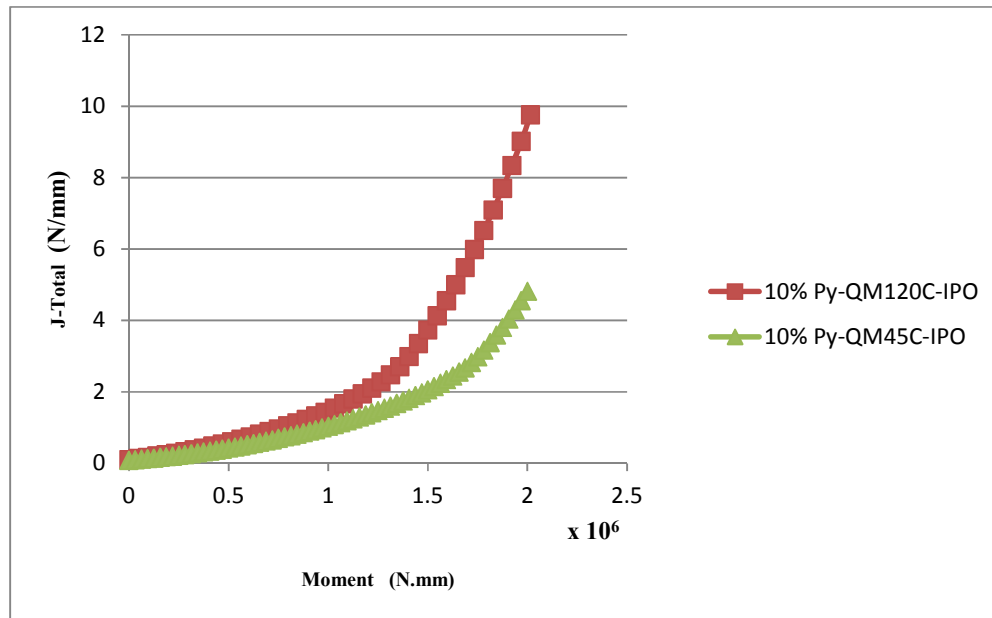


**Fig. 55 Comparison between the total J-integral obtained under IPO bending and 10%  $P_y$  of the models QM120C and QM45C ( $b/t=0.5$ )**

The effect of the different bending moment types adopted in this study on the resulted elastic and total J-integrals is shown in Fig. 56 and Fig. 57. It is evident from the graphs that the resulted J-integrals from IPO is much higher than those obtained from IPC which is consistent with the analysis of SD limit and limit load that was previously discussed in Sec. 3.1.3. It was expected that the IPC bending moment together with internal pressure would result in lower values of J-integral as compared to IPO which is proved from the comparison of both loading conditions given in Fig. 56 and Fig. 57.

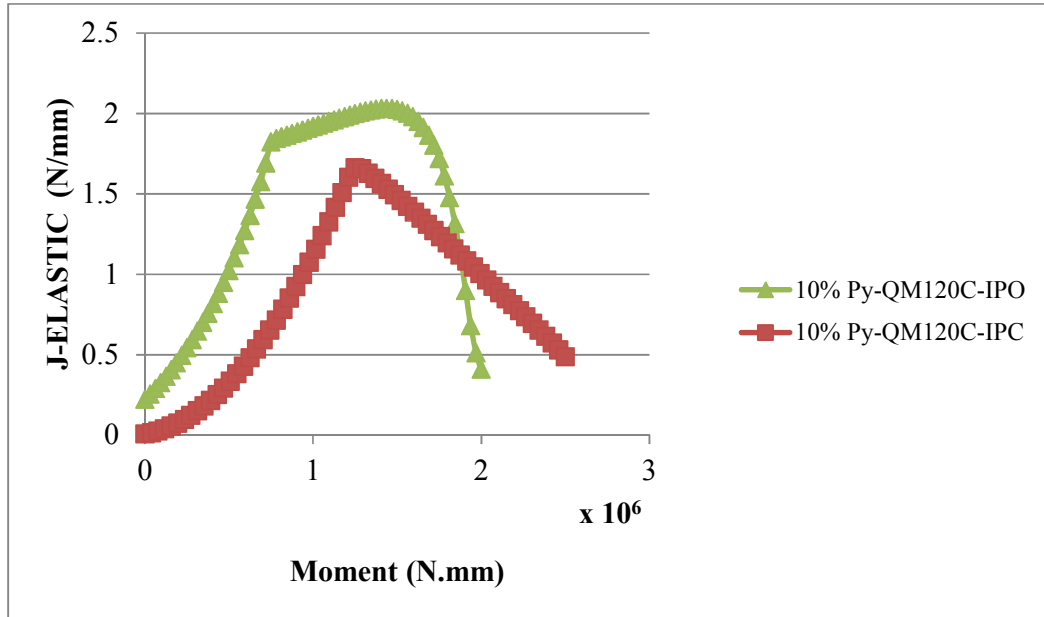


**Fig. 56 Comparison between the elastic J-integral obtained under IPO and IPC bending of the model QM120C (b/t=0.75)**

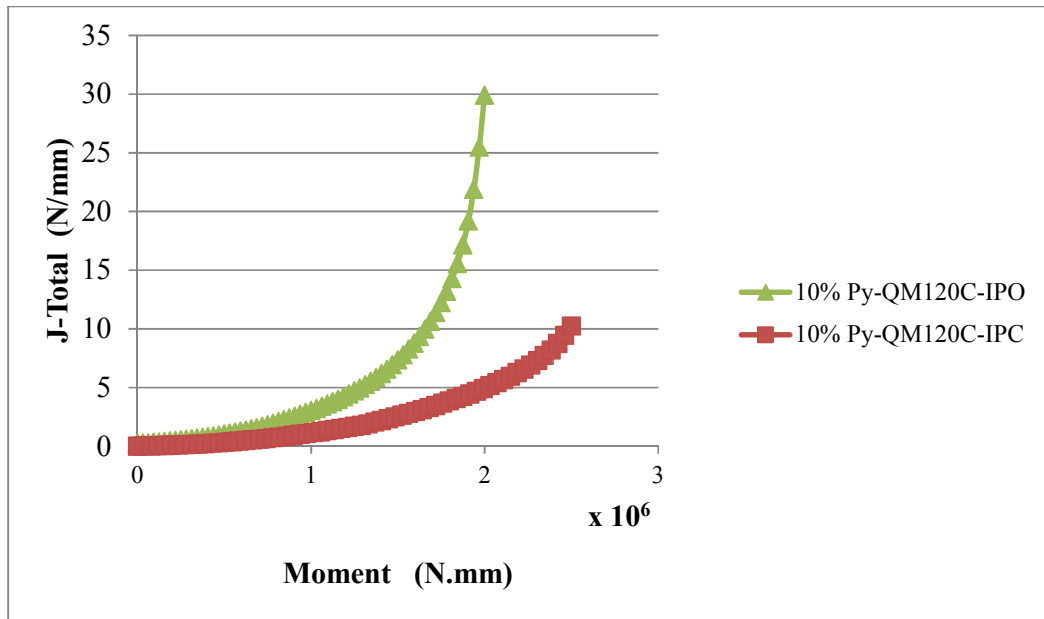


**Fig. 57 Comparison between the total J-integral obtained under IPO and IPC bending of the model QM120C (b/t=0.75)**

### 3.3.3 The proposed FAD

The proposed procedure used to develop the FAD is discussed in this section. As can be seen for all the following FAD's, a horizontal line that corresponds to the value of unity is always obtained at the beginning of the analysis indicating that the crack tip stresses are within the range of Linear Elastic Fracture Mechanics (LEFM). The curvature initiates when the plastic part of the J-integral starts to be accounted. The FAD of some Bree diagram points (loading conditions) is selected to be presented in Fig. 58-63. Similar diagrams were generated for all the models and for all the loading cases encountered in the Bree diagrams. It was noticed that the cut-off line intersected the FAD curve at a value that corresponds to 0.8 in the ordinate for the case of 0%  $P_y$  as shown in Fig. 58 which indicates that the plastic part of the J-integral is not dominant (only 20% of the total J-integral) when the SD limit was reached.

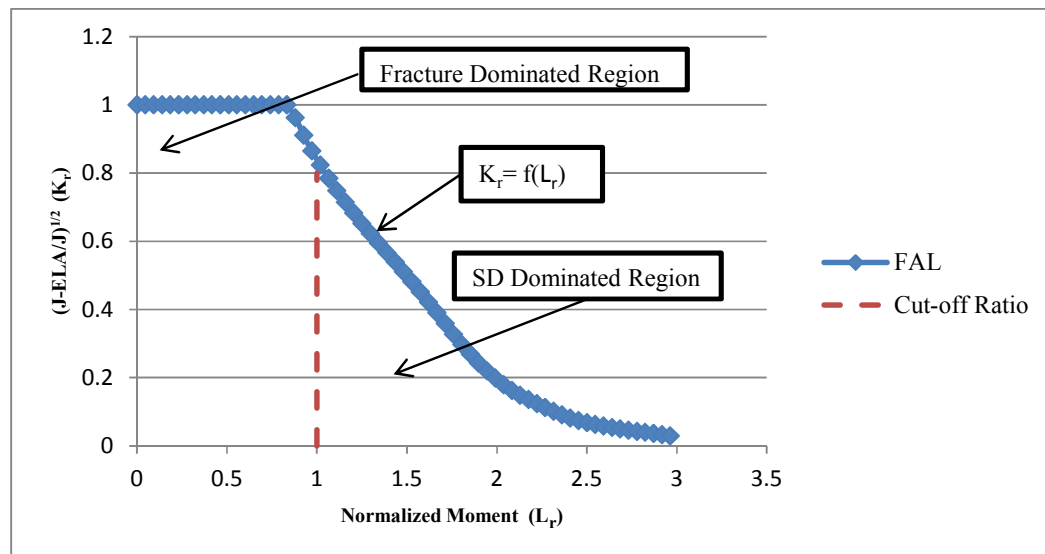
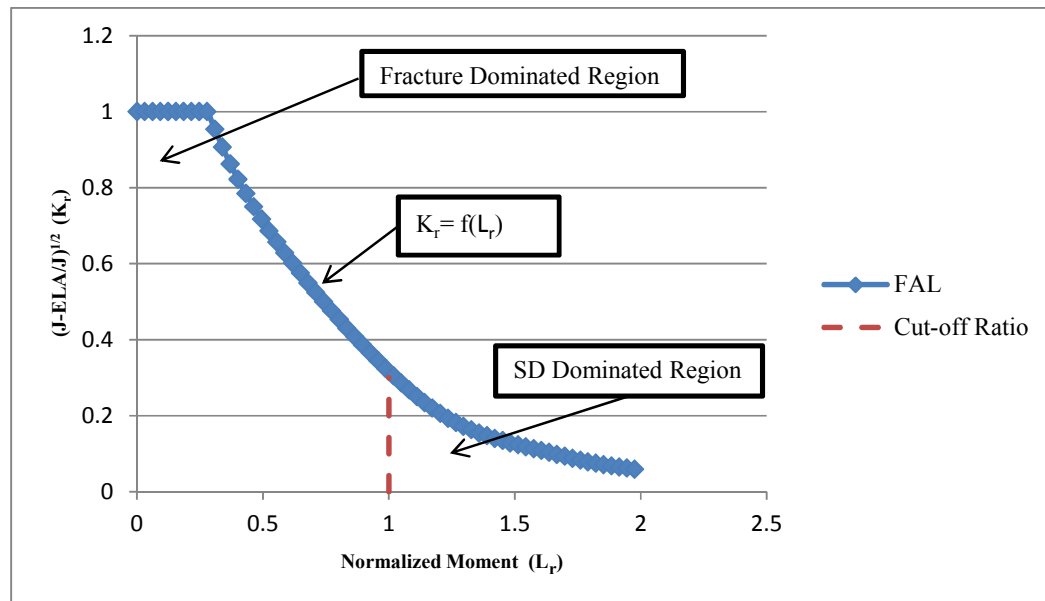


Fig. 58 Failure Assessment Diagram of QM120C model ( $P=0\%P_y$ ) and ( $b/t = 0.75$ )

Increasing the Internal pressure was shown to increase the plastic part of the J-integral up to approximately 65% for the cases of (10%-17%) $P_y$  of the model QM120C-IPO. A representative FAD for the cases of (10%-17%)  $P_y$  is shown in Fig. 59. The FAD's of the model QM120C-IPO are superimposed on one graph as shown in Fig. 60 in order to investigate the effect of increasing the internal pressure on the safe region of the FAD. A sample FAD for the models incorporating shorter cracks is shown Fig. 61. The FAD's of the model QM120C-IPC are superimposed on one graph as shown in Fig. 62 in order to investigate the effect of increasing the internal pressure on the safe region of the FAD. It is obvious that increasing the internal pressure is eroding the LEFM zone of the FAD and the safe region as well. A representative FAD of the models subjected to IPC moment is shown in Fig. 63. It is worth mentioning that the plastic part of the J-integral can indicate the tendency to failure by unstable crack growth rather than exceeding the SD limit.



**Fig. 59 Failure Assessment Diagram of QM120C-IPO model ( $P=15\%P_y$ ) and ( $b/t = 0.75$ )**

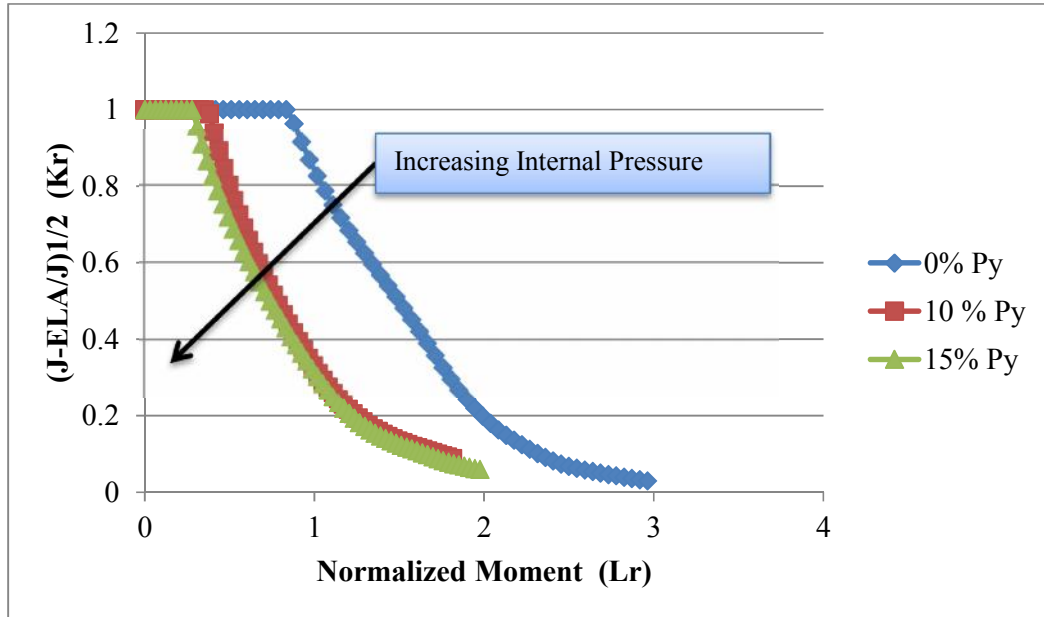


Fig. 60 The effect of increasing the internal pressure on the FAD of the model QM120C-IPO ( $b/t=0.75$ )

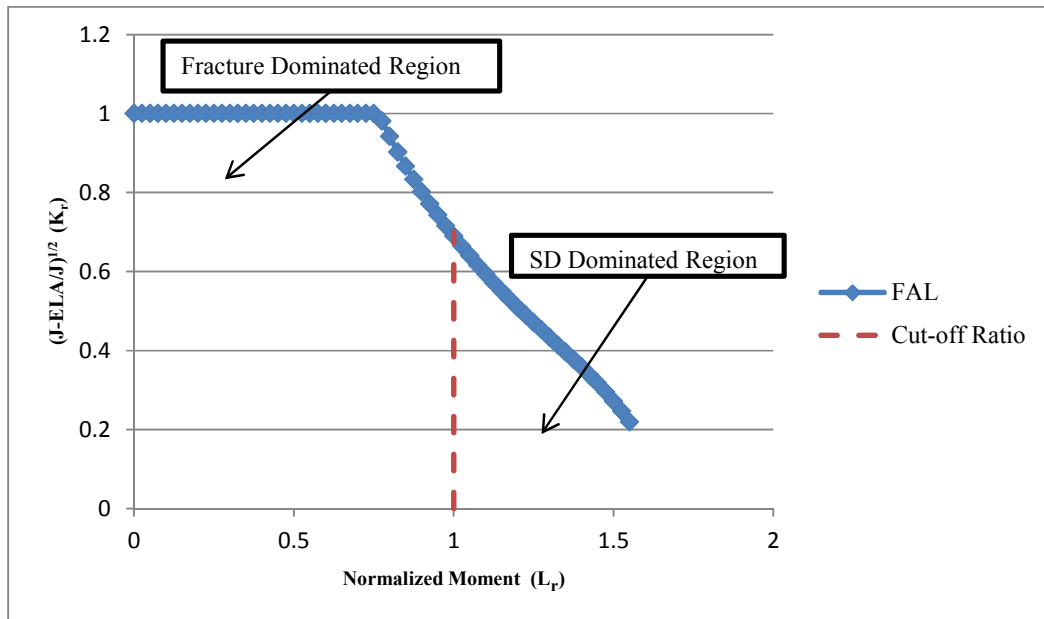
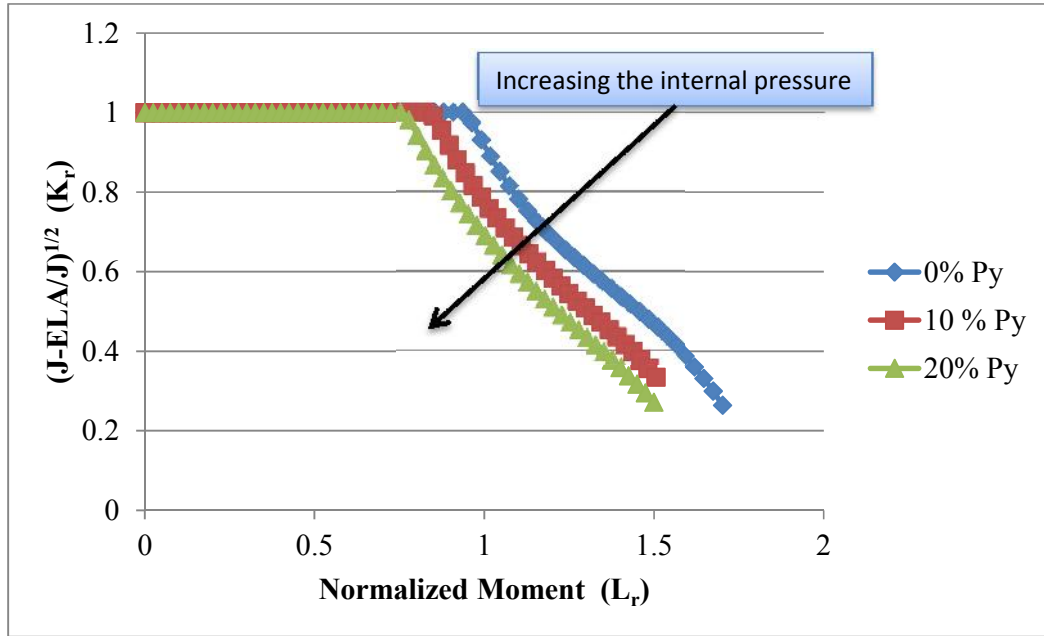
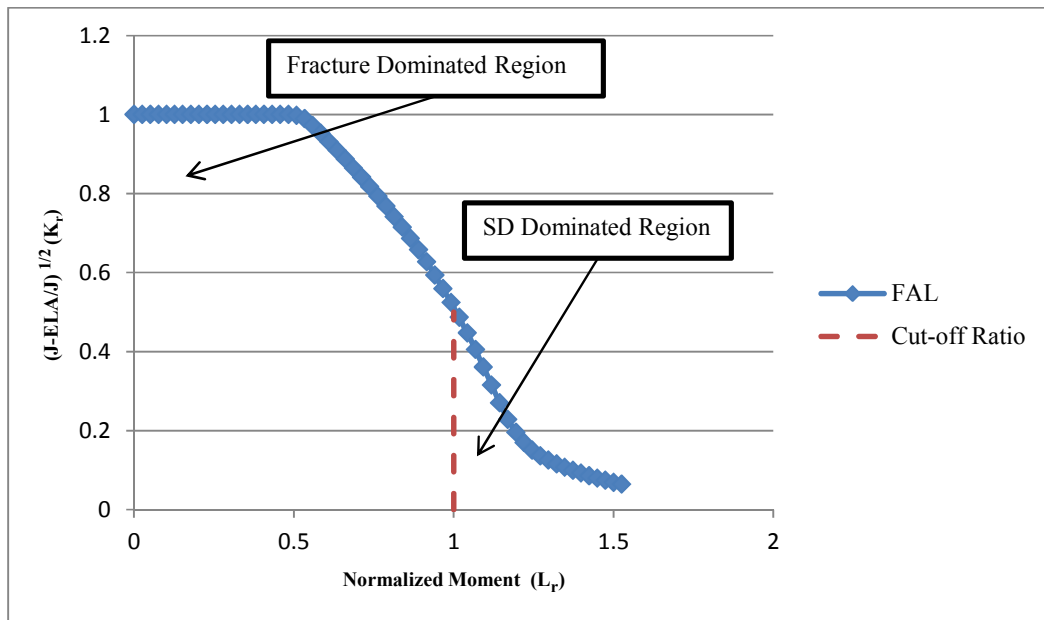


Fig. 61 Failure Assessment Diagram of QM45C-IPO model ( $P=20\%P_y$ ) and ( $b/t = 0.5$ )



**Fig. 62 The effect of increasing the internal pressure on the FAD of the model QM145C-IPO (b/t=0.5)**



**Fig. 63 Failure Assessment Diagram of QM120C-IPC model (P=40%Py) and (b/t = 0.75)**

### 3.3.4 Application of The proposed procedure

As a demonstration of using the proposed FAD procedure, the following case is studied:

- Loads:
  - IPO bending moment and internal pressure
- Crack angle:  $120^\circ$
- Crack depth to pipe thickness ratio: 0.75
- Material Properties
  - Yield Strength: 328 MPa
  - E: 210 GPa
  - $\nu$ : 0.3
  - $J_{Ic}$  : 6.9 N/mm

The Simplified Technique is applied and yielded the following results that is explained in detail is Sec. 3.1

$$0\% P_y: 0.17 M_p$$

$$15\% P_y: 0.16 M_p$$

The Elastic and total J-integral output from the LSE is shown in Fig. 64 and Fig. 65 for the case of 0% $P_y$  internal pressure. Similar curves are obtained for the case of 15%  $P_y$  internal pressures. The elastic J-integral is divided by the total J-integral yielding the toughness ratio that is used to plot the FAL with respect to the

load ratio obtained by dividing the applied moment by the SD limit moment. The FAL is the envelope that separates the safe region against brittle fracture and SD failure from the acceptable region. After generating the FAD the toughness ratio of the assessment point is obtained by dividing the elastic J-integral by the material fracture toughness ( $J_{Ic}$ ).

The assessment point is plotted in the FAD using the toughness ratio ( $k_r$ ) and load ratio ( $L_r$ ). The assessment points curve is superimposed on the FAD as shown in Fig. 66 and Fig. 67. It can be seen in Fig. 66 that the assessment point curve has intersected the cut-off ratio line that correspond to SD limit load before intersecting the FAL which means that the SD limit will be exceeded before having unstable crack growth (brittle fracture). On other hand, the assessment points curve has intersected the FAL before intersecting the cut-off ratio in Fig. 66 which means that the crack would propagate before exceeding the SD limit load. Hence, a new limit moment has to be defined in order to be safe for both SD failure and also brittle fracture.

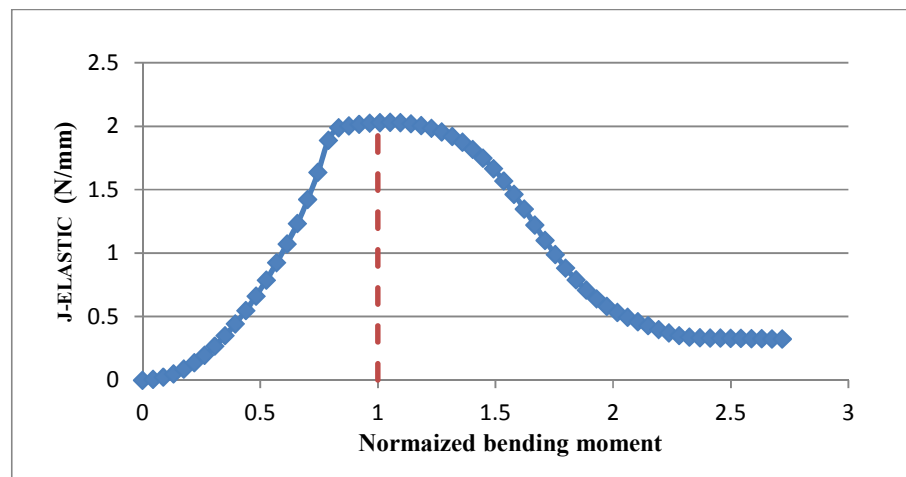


**Fig. 64 Elastic J-integral Vs. Applied Moment for the case of QM120C-IPO at**

**0%  $P_y$**

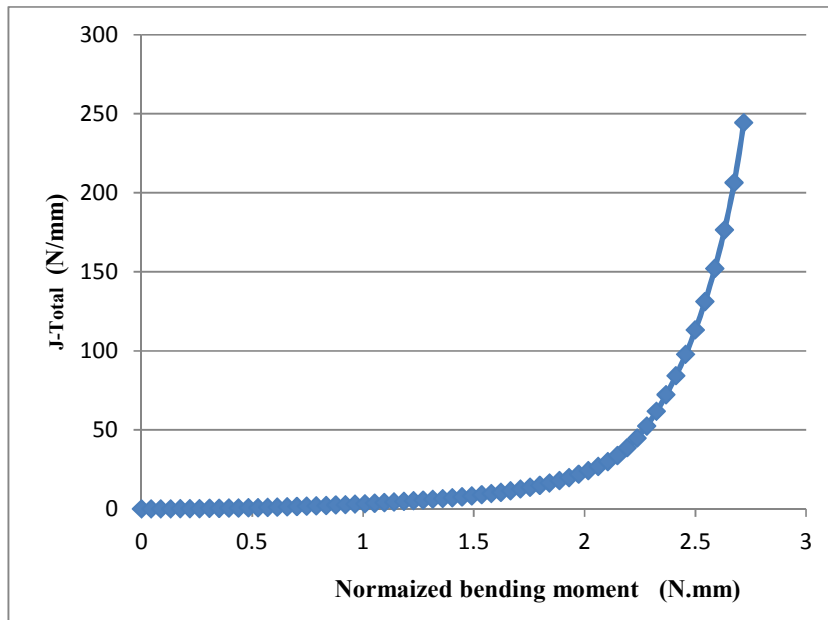


Fig. 65 Total J-integral Vs. Applied Moment for the case of QM120C-IPO at 0%

$P_y$

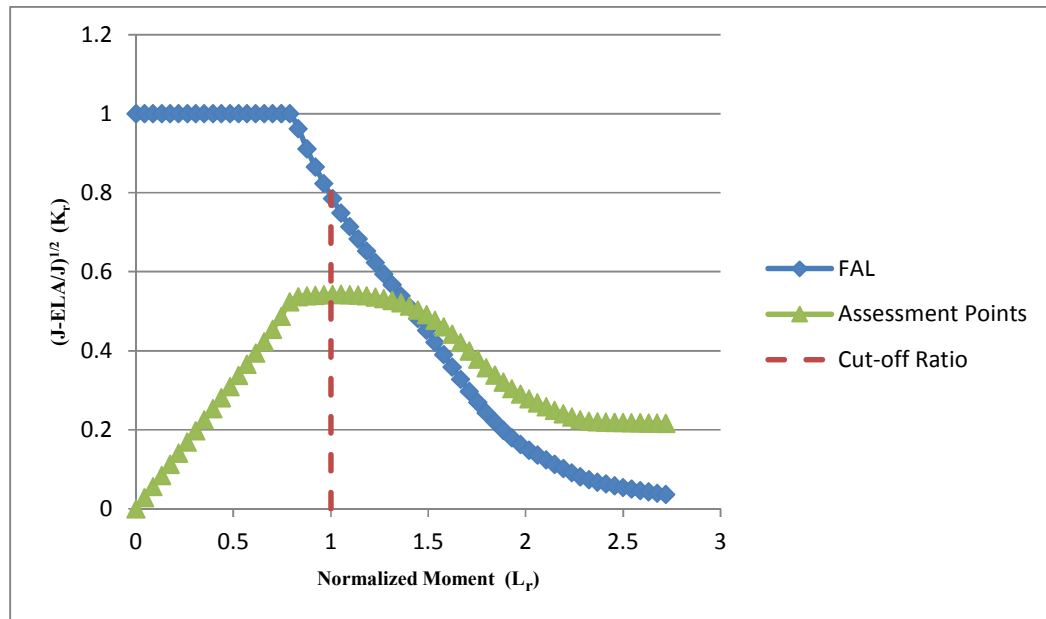
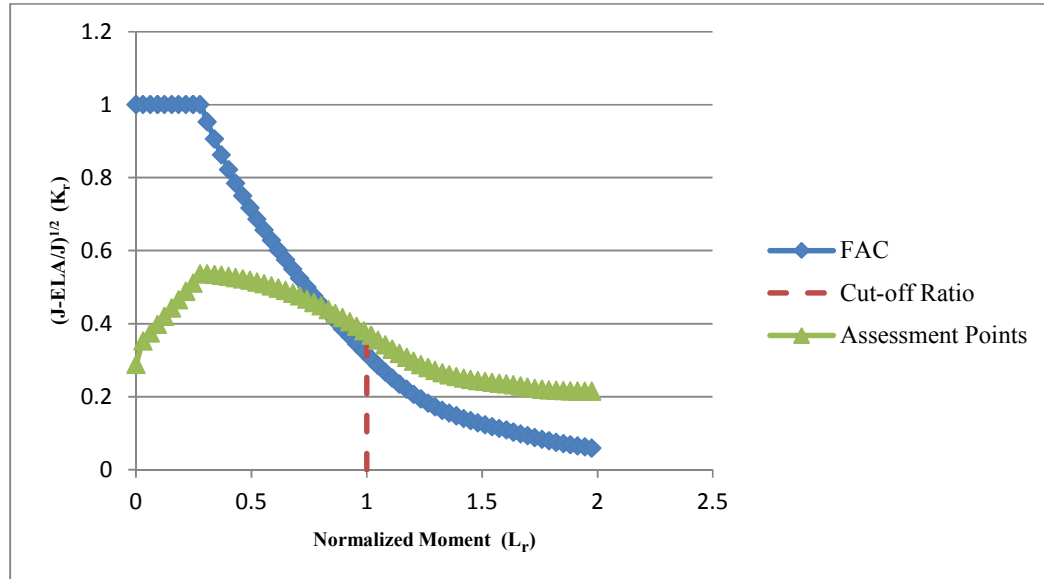


Fig. 66 Assessment points Vs. FAL for the model QM120C-IPO (b/t=0.75) at 0%

$P_y$



**Fig. 67 Assessment points Vs. FAL for the model QM120C-IPO (b/t=0.75) at 15% P<sub>y</sub>**

### 3.3.5 Crack growth analysis

The crack growth analysis of the pipe bend model with circumferential intrados crack growing in compliance with Paris law is shown in Fig. 68. The crack length was initially 45° and is postulated to grow with a constant cycle-to-cycle rate according to Paris law up to 120°. The crack is expected to grow in the length direction because the maximum SIF was found at the crack tip-free surface intersection.

Paris law constants constants (C and n) are obtained from the ASME-API 579 code for the material used in the current analysis. The stress intensity factor is obtained from the output of the LSE. The Paris law threshold ( $K_{th}$ ) for the material is compared to the SIF obtained from the LSE. The crack growth analysis should not be performed if  $\Delta K \leq \Delta K_{th}$ . Paris law is applied as follows:

$$(\Delta K_{th} = 2.0) \leq (\Delta K = 27.51) \text{MPa}\cdot\sqrt{m}$$

$$\frac{da}{dN} = 1.65(10^{-8})(27.51)^3 = 0.000344 \text{mm} / \text{cycle}$$

Based on the Paris law, the crack would extend from 45° to 120° after 158806 cycles. The Failure Assessment Diagram (FAD) of the pipe bend with 120° crack is superimposed on the FAD of the pipe bend with 45° crack. It is evident that the crack was safe against the unstable crack growth for the case of 45° crack. However, the crack growth resulted in unstable crack growth at a moment below the SD limit moment for the case of 120° crack. The effect of crack growth is shown to decrease the region of safety inside the FAD.

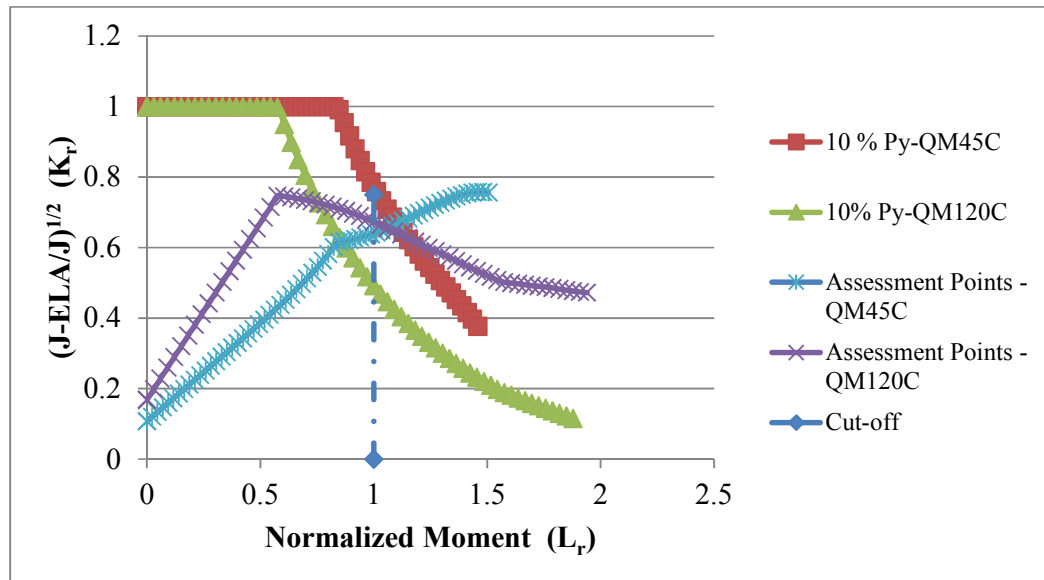


**Fig. 68 Crack growth analysis for the pipe bend models with circumferential crack at the intrados under the combined effect of IPO bending moment and internal pressure**

The Failure Assessment Diagrams obtained in this study are recommended to be used for the integrity assessment of cracked structures subjected to cyclic loadings since the load ratio is normalized using the SD limits obtained in this study utilizing the simplified technique while the load ratio used in the API 579 code and also R6 approach is normalized with respect to either the load that initiates yield or the load that causes plastic collapse.

## CHAPTER 4

### CONCLUSIONS and RECOMMENDATIONS

#### 4.1 Conclusions

The simplified technique and the Line Spring Model were utilized in order to generate the elastic shakedown boundary and Failure-Assessment-Diagrams of circumferentially cracked pipe bends. Experimental (limit load) and numerical (SIF and SD limit load) Verification studies are conducted. The Finite Element (FE) models results of this study agreed with both experimental and numerical results. The following observations were concluded from the current study:

- It was observed that long postulated cracks ( $\Theta = 120^\circ$ ) on the intrados have remarkably decreased the SD limit of pipe bends subjected to the combined effect of steady internal pressure and cyclic IPO bending moment compared to the defect-free model.
- Pipe bend with cracks located at the extrados was subjected to IPC moments. It was shown that IPO moments caused more reduction in the SD boundary compared to IPC moment. Both the models subjected to IPO or IPC bending moments have cracks at the tension side to allow crack opening under loading.
- Limit loads of cracked pipe bends were considerably reduced for long cracks ( $\Theta = 120^\circ$ ) while pipe bends have shown to be sustaining the presence of short cracks ( $\Theta = 45^\circ$ ) without a considerable decrease on the SD boundary.

- A new procedure is developed for the integrity assessment of cracked structures; the proposed procedure utilized the simplified technique to obtain SD limit load and J-integral output from ELPL FE analyses.
- Increasing the internal pressure causes the safety region inside the FAD to decrease and also shortens the straight line that represents the LEFM region of the FAD; this effect has been noticed for all the models considered in the current work.

#### 4.2 Recommendations and future work

- As a general conclusion from this study, it is recommended to introduce the SD limit load to the FAD for the use of the integrity assessment of cracked structures. J-integral obtained from ELPL fracture mechanics analyses is recommended to be utilized to obtain the toughness ratio (ordinate of the FAD) while the SD limit moment is utilized to obtain the load ratio of the diagram (abscissa of the FAD).
- The procedure adopted in this work is recommended to be applied to other pipe bend geometrical configurations such as long radius pipe bends and also for other ( $d_m/t$ ) ratios that include both thin and thick shell categories.
- The procedure adopted in this work is recommended to be extended to investigate the presence of crack like flaws on other piping and pressure vessel components such as T-branches and nozzle-vessel intersections.

## REFERENCES

- [1] Mourad, H. M., and Younan, M. Y., "Limit-Load Analysis of Pipe bends under Out-of-Plane Moment Loading and Internal Pressure", ASME Journal of Pressure Vessel Technology, Vol. 124, No. 1, 2002, pp. 32 - 37.
- [2] Bantlin, A., 1910, "Formänderung und Beanspruchung federnder Ausgleichröhre," Zeitschrift des Vereines Deutscher Ingenieure, 54, pp. 43–49.
- [3] Von Karman T. Uber die formänderung dunnwandiger rohere, insbesondere federnder ausgleichrohre. Z Vereines Dtsch Ing 1910; 55:1889–95 [in German].
- [4] Abdalla, H. F., "A Simplified Technique for Shakedown Limit Load Determination with Application to 90-Degree Pipe Bends," PhD Thesis, Cairo University, 2009.
- [5] Gruning, M., Die Tragfähigkeit Statisch Unbestimmter Tragwerke Aus Stahl Bei Beliebiger Häufig Wiederholter Belastung, Springer, Berlin, 1929.
- [6] Bleich, H., "Ueber Die Bemessung Statisch Unbestimmter Stahltragwerke", Bauingenieur, Vol. 13, No. 19-20, 1932, pp. 261 - 267.
- [7] Melan, E., 1936, "Theorie Statisch Unbestimmter Systeme Aus Ideal Plastischem Baustoff," Sitzber. Akad. Wiss. Wien IIa, 145, pp. 195-218.
- [8] Melan, E., "Der Spannungszustand Eines Mises-Henckyschen Kontinuums Bei Veränderlicher Belastung", Sitzber. Akad. Wiss. Wien IIa, Vol. 147, 1938, pp. 73 - 78.
- [9] Melan, E., "Zur Plastizität Des Räumlichen Kontinuums", Ing. Arch., Vol. 8, 1938, pp. 116 - 126.
- [10] Koiter, W. T., "General Theorems for Elastic Plastic Solids", Progress in Solid Mechanics, 1960, pp. 165 - 221.

- [11] ASME Boiler and Pressure Vessel Code, 2004 edition, Section VIII Division 2, American Society of Mechanical Engineers, New York.
- [12] UK Pressure Vessel Design Code, “PD 5500:2006”, British Standards Institution, UK, 2006.
- [13] Spence, J., and Tooth, A., Pressure Vessel Design: Concepts and Principles, E & FN Spon, New York, 1994.
- [14] European Standard (2005-06), “Unfired Pressure Vessels - Part 3: Design - Annex 2”, “Annex B Direct Route for Design by Analysis”, and “Annex C Stress Categorisation Route for Design by Analysis”, CEN European Committee for Standardization, 2002.
- [15] Trần, T., Kreissig, R., Vu, D., and Staat M., “Upper Bound Limit and Shakedown Analysis of Shells Using the Exact Ilyushin Yield Surface”, Computers and Structures, Vol. 86, No. 17 - 18, 2008, pp. 1683 - 1695.
- [16] Andrew Robertson, Hongjun Li, Donald Mackenzie, 2005, “Plastic collapse of pipe bends under combined internal pressure and in-plane bending,” ASME Journal of Pressure Vessel Technology, 82, pp. 407-416.
- [17] Yahiaoui, K., Moffat, D. G., and Moreton, D. N., 2000, “Piping elbows with cracks Part 2: global finite element and experimental plastic loads under opening bending,” Journal of Strain Analysis, 35, pp. 47-57.
- [18] API 579-1/ASME FFS-1 2007 Fitness-For-Service
- [19] Abdalla, H. F., Megahed, M. M., and Younan, M. Y. A., 2006, “Determination of Shakedown Limit Load for a 90 Degree Pipe Bend Using a Simplified Technique,” ASME Journal of Pressure Vessel Technology, 128, pp. 618-624.

- [20] Marriott, D. L., 1988, "Evaluation of Deformation or Load Control of Stress under Inelastic Conditions Using Finite Elements Stress Analysis," ASME transactions, PVP division conference, 136, pp. 3-9.
- [21] Dhalla, A. K., 1987, "A Simplified Procedure to Classify Stresses for Elevated Temperature Service," ASME transactions, PVP division conference, 120, pp. 177-188.
- [22] Seshadri, R., 1991, "The Generalized Local Stress Strain (GLOSS) Analysis-Theory and Applications," ASME Journal of Pressure Vessel Technology, 113, pp. 219-227.
- [23] Ponter, A., and Boulbibane, M., 2002, "Minimum Theorems and the Linear Matching Method for Bodies in a Cyclic State of Creep", European Journal of Mechanics, A/Solids, 21, pp. 915-925.
- [24] Mackenzie, D. and Boyle, J. T., 1993, "A Simple Method for Estimating Shakedown Load for Complex Structures," Journal of Pressure Vessel Technology, 265, pp. 89-94.
- [25] Mackenzie, D., Boyle, J. T., & Hamilton, R. 1999, "The Elastic Compensation Method for Limit and Shakedown Analysis: a Review." Journal of Strain Analysis, pp. 171-188.
- [26] Muscat, M. and Mackenzie, D., 2003, "Elastic Shakedown Analysis of Axisymmetric Nozzles," Journal of Pressure Vessel Technology, 125, pp. 365-370.
- [27] Abdalla, H. F., Megahed, M. M., and Younan, M. Y. A., 2007, "Shakedown Limits of a 90-Degree Pipe Bend using Small and Large Displacement Formulations," ASME Journal of Pressure Vessel Technology, 129, pp. 287-295.

- [28] Abdalla, H. F., Megahed, M. M., and Younan, M. Y. A., 2007, “A Simplified Technique for Shakedown Limit Load Determination,” Nuclear Engineering and Design. 237, pp. 1231-1240.
- [29] Abdalla, H. F., Megahed, M. M., and Younan, M. Y. A., 2011, “A Simplified Technique for Shakedown Limit Load Determination of a Large Square Plate with a Small Central Hole Under Cyclic Biaxial Loading,” Nuclear Engineering and Design. 241, pp. 657-665.
- [30] Abdalla, H. F., Younan, M. Y. A., and Megahed, M. M., 2011, “Shakedown Limit Loads For 90-Degree Scheduled Pipe Bends Subjected to Constant Internal Pressure and Cyclic Bending Moments,” ASME Journal of Pressure Vessel Technology, 133, 031207.
- [31] Abdalla, H. F., Younan, M. Y. A., and Megahed, M. M., “Shakedown Limit Load Determination for a Kinematically Hardening 90-Degree Pipe Bend Subjected to Constant Internal Pressure and Cyclic Bending,” ASME transactions, PVP division conference, San Antonio, Texas, USA, July 2007.
- [32] Abdalla, H. F., Megahed, M. M., and Younan, M. Y. A., “Comparison of Pipe Bend Ratcheting/Shakedown Test Results with the Shakedown Boundary Determined via a Simplified Technique,” ASME transactions, PVP division conference, Prague, Czech Republic, July 2009.
- [33] Abdalla, H. F., Megahed M. M., and Younan, M. Y. A., “Determination of Shakedown Limit Loads for a Cylindrical Vessel–Nozzle Intersection Via a Simplified Technique,” ASME transactions, PVP division conference, Maryland, USA, July 2011.
- [34] Feng, X. Q., & Gross, D., 1999, “A global/local shakedown analysis method of elastoplastic cracked structures,” Engineering Fracture Mechanics, pp. 179-192

- [35] Yinghua, L., Carvelli, V., & Maier, G., 1998, "Limit and shakedown analysis of pressurized pipelines containing defects," *The Chinese Society of Theoretical and Applied Mechanics*, 14, pp. 65-75.
- [36] Mingde, X., Xianfeng, W., & Bingye, X., 1996, "Lower-bound shakedown analysis of spherical shells containing defects," *International Journal of Pressure Vessels and Piping*, 68, pp. 877-889.
- [37] Yahiaoui, K., Moffat, D. G., and Moreton, D. N., 2000, "Piping elbows with cracks Part 1: a parametric study of the influence of crack size on limit loads due to pressure and opening bending," *Journal of Strain Analysis*, 35, pp. 35-46
- [38] Yahiaoui, K., Moffat, D. G. and Moreton, D. N. "Damage Assessment of Piping Elbows Loaded by Steady Internal Pressure and Dynamic In-Plane or Out-Of-Plane Bending. ", In *Proceedings of the Eighth International Conference on Pressure Vessel Technology*, Vol. 1, Montreal, 1996, pp. 361-375.
- [39] Yahiaoui, K., Moffat, D. G., and Moreton, D. N., 2002, "Evaluation of Limit Load Data for Cracked Pipes Under Opening Bending and Comparison with Existing Solutions," *ASME Journal of Pressure Vessels and Piping*, 79, pp. 27-36.
- [40] Miller A.G., 1988, "Review of Limit Loads of Structures Containing Defects," *ASME Journal of Pressure Vessels and Piping*, 32, pp. 197-327.
- [41] Zahoor A., "Ductile Fracture Handbook," Vols. 1-3, Electric Power Research Institute, EPRI NP-6301-D/N14, Palo Alto, California, USA, 1989, 1990, 1991.
- [42] Kim, Y., Oh, C., Kim, Y. and Park, C., "Finite Element Loads for Circumferential Through-Wall Cracked Pipe Bends under In-Plane Bending," *ASME transactions, PVP division conference, Vancouver, BC, Canada, July 2006*.

- [43] Chattopadhyay, J., Dutta, B.K., Kushwaha, H.S., Roos, E., Herter, K.-H., 2004, "Load bearing capacity of flawed piping components-comparison of experiment with calculation," ASME Journal of Pressure Vessels and Piping, 81, pp. 599-608.
- [34] Chattopadhyay J, Tomar AKS, Dutta BK, and Kushwaha HS., "Collapse Moment of Elbows with Throughwall Circumferentially Crack Subjected to In-plane Bending Moment," 29th MPA Seminar, MPA, Stuttgart, 9–10th October. 2003.
- [45] Milne I, Ainsworth RA, Dowling AR, Stewart AT. "Assessment of the integrity of structures containing defects. " R/H/R6-Rev. 3 Central Electricity Generating Board, May; 1986.
- [46] Simha, C., 2011, "Limit Load Solutions for Cracked Elbows Subjected to Internal Pressure and In-Plane Bending," ASME Journal of Pressure Vessels and Piping, 81, pp. 599-608.
- [47] Goodall, I. W., 1978, "Lower Bound Limit Analysis of Curved Tubes Loaded By Combined Internal Pressure and In-Plane Bending Moment," Technical Report RD/B/N4360, Central Electricity Generating Board Report.
- [48] Yahiaoui, K., Moffat, D. G., and Moreton, D. N., 2000, "Local Finite Element and Experimental Limit Loads of Cracked Piping Elbows Under Opening Bending," Journal of Strain Analysis, 36, pp. 175-186.
- [49] Rice, J.R. , Levy, N., 1972, "The part-through surface crack in an elastic-plastic plate," ASME Journal of Applied. Mechanics., 39, pp. 185-194.
- [50] Rice, J.R. , Levy, N., 1972, "The line-spring model for surface flaws, in: The Surface Crack: Physical Problems and Computational Solutions," ed., J.L. Swedlow, American Society of Mechanical Engineers.

- [51] Parks, D.M., 1981, "The inelastic line-spring: Estimates of elastic plastic fracture mechanics parameters for surface- cracked plates and shells," ASME Journal of Pressure Vessel Technology, 103, pp. 246-254.
- [52] Parks, D.M., 1981, "Inelastic analysis of surface flaws using the line-spring model," Advances in Fracture), ed.: D. Francois, 5 , pp. 2589-2598.
- [53] Goncalves, J.P.M and De Castro, P.M.S.T., 1999, "Application of the line spring model to some complex geometries, and comparison with three-dimensional results," ASME Journal of Pressure Vessels and Piping, 76 , pp. 551-560.
- [54] SIMULIA - Dassault Systèmes, 2009, ABAQUS/Standard, Version 6.9-1, "User Documentation Manuals".
- [55] Sauter, A., Turan, K., Kerkhof, K., And Wagemann, G., 1989, "Fracture Mechanics Analysis Of A Pipe Elbow" Nuclear Engineering and Design, 122 , pp. 211-220.
- [56] Raju, I. S., and Newman, JR., 1979, "Stress-intensity factors for a wide range of semi-elliptical surface cracks in finite-thickness plates" Engineering Fracture Mechanics, 11 , pp. 817-829
- [57] Murakami, Y., "Stress intensity factors handbook," Vols. 1-2, Pergamon , New York, USA, 1987.e
- [58] Raju, I. S., and Newman, JR., 1982, "Stress-intensity factors for internal and external surface cracks in cylindrical vessels" Engineering Fracture Mechanics, 11 , pp. 817-829
- [59] Budden, P. J., Sharples, J. K., and Dowling, A.R., 2000, "The R6 procedure: recent developments and comparison with alternative approaches" International Journal of Pressure Vessels and Piping, 77, pp. 895-903

- [60] Barsoum, R. S., 1976, "On the use of isoparametric finite elements in linear fracture mechanics" International Journal of Numerical Methods in Engineering, 10, pp. 25-37.

## Appendix (A)

### Part-9 ASME FFS-1 API-1 Fitness-For-Service Assessment

#### Procedure for Crack-like Flaw

The Assessment procedure of structures with crack-like flaws can be summarized as follows:

- 1- Flaw and Damage Mechanism Identification
- 2- Applicability and Limitation of The Fitness-For-Service (FFS ) Assessment Procedure

Level 1 and level 2 assessments can only be applied if all the following conditions are satisfied:

- The component is not operated within the creep temperature range.
- The component is not subjected to significant dynamic loads.
- Loading and environmental conditions will not lead to crack growth (level 3 assessment can be applied if crack growth is anticipated)
- Level 1 assessment can be applied only for the following conditions:
  - Limiting conditions on component and flaw geometries:
    - The component is flat plate, cylinder, or sphere.
    - The maximum wall thickness of the component at the region of the crack like flaw is 38 mm.
    - The maximum crack length is 200 mm.
    - If any structural discontinuity exists, a minimum distance of  $1.8 \sqrt{Dt}$  between the crack like flaw and the structural discontinuity should be existing.

- Limiting conditions on component loads:
  - The loading condition is only a pressure that produces membrane stresses only and does not introduce bending stresses.
  - The resulting membrane stresses from the applied pressure should be within the allowable limits of the original construction code.
- Limiting conditions on component material properties:
  - The material is carbon steel which have the following properties:
    - Allowable stress < 172 MPa
    - Specified minimum yield strength 276 MPa
    - Specified minimum tensile strength 483 MPa
    - Fracture Toughness lower bound  $K_{Ic}$
- Level 3 assessment should be adopted for the following conditions:
  - The loading condition and the geometry are complicated which will result in a state of stress around the crack like flaw that needs advanced methods of solution
  - Loading and environmental conditions will result in potential active growth phase of the crack like flaw
  - High gradients of stresses, fracture toughness, yield, or tensile strength exist in the vicinity of the crack like flaw

## Appendix (B)

### R6 Defect Assessment Procedure

The R6 procedure was initially developed by the Central Electricity Generating Board (CEGB) in 1976 and then continually developed to account for the integrity assessment of defected structures in the various fields of industry. After the privatization of CEGB, improving and the continuous development of the R6 approach revisions has become the responsibility of British Energy. The R6 approach has witnessed 4 major revisions [59]. There are three main options that can be used to perform the assessment of the integrity of cracked structures by the R6 approach. Option one is a general purpose that is independent of the material, load and geometry. The Failure Assessment line is plotted using Eq (18) and the Cut-off ratio is defined using Eq. (19).

$$f(L_r) = (1 - 0.14L_r^2)(0.3 + 0.7 \exp(-0.65L_r^2)) \quad (18)$$

$$L_{\max}^r = \frac{1}{2} \left(1 + \frac{\sigma_u}{\sigma_y}\right) \quad (19)$$

Option 2 assessment procedure is more specific as it accounts for material's detailed stress-strain curve; however, it does not account for loads and geometrical configurations. Option 3 assessment is implemented by explicit J-integral analyses. Hence it depends on the structure's material properties, loading conditions, geometry and crack size. Option 3 of the R6 approach is utilized in the current work to generate the FAD and the assessment of integrity of cracked pipe bends.

## Appendix (C)

### Line Spring Element Formulation

Goncalves et. al. [53] summarized the theory behind the line spring model as follows: the governing equation that relates local forces  $N(x)$ ,  $M(x)$  to their local work conjugate displacement can be given as:

$$\begin{bmatrix} N(x) \\ M(x) \end{bmatrix} = \begin{bmatrix} S_{11}(x) & S_{12}(x) \\ S_{21}(x) & S_{22}(x) \end{bmatrix} \begin{bmatrix} \delta(x) \\ \theta(x) \end{bmatrix} \quad (20)$$

The Stiffness Matrix  $S$  is obtained by modeling the springs as plain strain single-edge notched specimen. The virtual work contribution of the element LS3S that is provided for Mode I failure on symmetry planes is given as:

$$VW = \int \begin{bmatrix} \delta_1^* & \theta_1^* \end{bmatrix} \begin{bmatrix} N_1 \\ M_1 \end{bmatrix} dL \quad (21)$$

Where  $\delta_1^*$  and  $\theta_1^*$  are virtual displacement and rotation, respectively. The element LS3S and LS6 are found in the element library of ABAQUS [54] and can be used to model part through cracks in conjugate with quadratic shell elements. The element stiffness matrix formulation of Eq (18) has three points Simpson's rule, consequently the element integration points are at the nodes.